A THESIS

FOR THE DEGREE OF DOCTOR OF PHILOSOPHY

Graphene oxide and Graphene nanosheets: Tunable properties and multifunctional applications

Karthikeyan Krishnamoorthy

Department of Mechanical System Engineering

GRADUATE SCHOOL

JEJU NATIONAL UNIVERSITY

2012. 12

博士學位論文

Graphene oxide and Graphene nanosheets: Tunable properties and multifunctional applications

濟州大學校 大學院

機械工學 科

케이 카티케얀

2012 年 12 月

Graphene oxide and Graphene nanosheets: Tunable properties and multifunctional applications

Karthikeyan Krishnamoorthy

(Supervised by Professor Sang-Jae Kim & Professor Gui-Shik Kim)

A thesis submitted in partial fulfillment of the requirement for the degree of Doctor of Philosophy

2012. 12

The thesis has been examined and approved.

Prof. Somi Kim Cho, Chairman, Thesis Committee Member	College of Applied Life Sciences Jeju National University
Prof. Hyeon Suk Shin, Thesis Committee Member	Advanced centre for energy Ulsan Institute of Science and Technology
Prof. Young-Sun Mok, Thesis Committee Member	Dept. of Chemical Engineering Jeju National University
Prof. Gui-Shik Kim, Thesis Committee Member	Dept. of Mechanical Engineering Jeju National University
Prof. Sang-Jae Kim, Thesis Committee Member and Supervisor	Dept. of Mechatronics Engineering Jeju National University

December, 2012

Date

Nanomaterials and System Lab
Department of Mechanical System Engineering
GRADUATE SCHOOL
JEJU NATIONAL UNIVERSITY
REPUBLIC OF KOREA

Dedicated to

My Parents

Acknowledgements

I would like to express my sincere gratitude to the many individuals who contributed to success of my work. First of all I would like to thank my research advisor, Professor Sang-Jae KIM. Through his positive and open-minded attitude, and his enthusiasm and optimism toward research on material science engineering, he created the legacy of the free, vivid, intelligent, friendly and communicative research atmosphere in the lab. I feel really lucky to be able to work in such environment. His experience, knowledge, and guidance have been invaluable throughout my graduate career.

I would also like to thank my research co-advisor Professor Gui-Shik KIM for his continuous support in my Ph.D. work. Next I would like to thank Professor Somi Kim Cho for her support in the collaborative research in nanobiotechnology. I also thank Professor Kyusik Yun and Professor Jehee Lee for their support in studying the biological applications of graphene related materials. I also thank Prof K. Jeyasubramanian and Prof M. Premanathan for their constant support and encouragement.

I would like to thank my senior Prof V. Gunasekaran, who introduced me in to this lab and gave support throughout the course. I would like to express my deep appreciation to Dr. R. Mohan and Dr. S. Saini for their valuable suggestions and timely help. Next, I would also like to remember the support from friends Dr. V. Murugan Veerapandian, Mr. R. Ananthakumar, Mr. Umasuthan Navaneethaiyer, Mr. Sebastian Ananth, Mr. J. Y. Moon and Mr. H. B. Hyun for the collaborative projects. I am dearly thankful to all the current members of our group (Mr. K. Thiyagarajan, Mr. B. Saravanakumar, Mr. Kim Dae young, Mr. Kim Tae Hyun, Mr. Hong Eui-Yong, Ms. Shin So Yoon, and Ms. Bak Seo Hyeon) who provided a joyful environment and timely helps.

Next I would like to thank my better half Ms. P. Nithiyabharathi for being me in high spirit at all times. Then, I would say my heartiest thanks to Dr. Ganesh Thangaraj and Mr. Navaneethan for their fruitful discussions and suggestions during the period when I was highly depressed. It is immense pleasure for me to thank Dr. M. S. Gandhi for his PUNCH dialogues and delicious foods. I thank Dr. Anil, Dr. Harikrishnan, Dr. Dharanitharan, Mr. Raviteja, Mr. Sridhar, Mr. Purushothaman and

Mrs. Saranya Purushothaman, for providing good environment in Jeju. I would like to thank all those whom I have not mentioned above but helped me in numerous ways to my success.

I am also grateful for the Regional Instrument Center (RIC) at Jeju National University for providing me opportunities to handle many instrument facilities during my study and I thank Mr. Ko at RIC for their cheerful assistance in the work. Many thanks to Graduate school of Jeju University which has been grateful to waive the tuition fee for my doctoral studies. I also thank Brain Korea 21 (BK-21) and NRF project research grants which provided the funds for my entire Ph.D. work.

I would like to express my deepest gratitude to my brother Mr. K. Parthiban who had taken over my responsibilities in my home and supported me to achieve my goal.

Contents

초 록

산화 그래핀(GO) 나노시트는 물성물리 및 응용분야에서 매우 중요한 차세대 전자재료로서 기대되고 있다. 산화 그래핀은 1859 년 Brodie 에 의해 처음 제작된 이후로 활발히 연구되어 왔지만, GO 의 화학적 특성은 이질적이고 비결정적인 특성 때문에 이론적 및 실험적으로 정확하게 설명하기 어려운 부분이 과제로 남아있다. 본 학위논문에서는, 그래핀 내의 산화 농도에 따라서 조절 가능한 산화그래핀의 성질 및 특성을 이해하기 위하여 산화농도에 따른 GO 의 화학적, 구조적인 특징들에 관하여 연구를 수행하였다. 또한, GO 의 산화농도에 따른 구조적 및 전기화학적인 특성 의존성을 조사하였다.

본 연구에서는 전자재료 및 전자산업에서 응용이 촉망 받고 있는 그래핀 나노시트의 GO 를 환원시키기 위한 주요실험으로써는 4 가지 제작방법을 시도하였다. 첫번째는 쉽고 빠르게 실험할 수 있는 초음파법을 사용하였고, 두번째로 저비용과 고효율적인 방법으로 실험하기 위하여 수열합성법을 이용하였다. 또한 생합성 방법(biosynthesis), 그리고 마지막으로 저온, 무독성적인 실험을 위하여 수소 플라즈마(hydrogen plsma) 조사방법을 사용하여 실험하였다. 그리고 상기에서 기술한 네가지 방법으로 제작된 그래핀 및 산화그래핀은 스펙트럼 분석법(spectroscopic techniques)을 주로 하여 실험 및 해석을 하였다.

또한, 광촉매 분야내의 GO 나노시트의 응용 가능성을 검토하기 위하여 자외선영역에서의 레사주린 (resazurin)이 GO 의 작용기에 의해 레소루핀(resorufin)으로 변화하는 양상에 대하여 실험적으로 측정하고 비교 설명하였다. 또한, GO 의 항균력과 실용적인 응용을 위한 항균 섬유를 제작하여 그 특성을 조사하여 보고 하였으며, 금속부식을 보호하기 위한 GO 박막의 방식특성에 대하여 전기화학적 특성분석을 이용하여 조사하였다. 수열합성법에 의해 제작된 그래핀 나노시트의 항균력에 대하여 연구하였으며, 수소플라즈마(hydrogen plasma)방법에 의해 제작된

그래핀 나노시트의 차세대 저장소자인 슈퍼커패시터 적용에 관하여 조사하였다.

대표적인 응용분야로써, 볼 분쇄기(ball milling) 를 이용하여 경제적이고 대량생산이 가능한 무독성 GO 나노페인트를 제작하였다. 그리고 산과 염소를 포함하는 해수 분위기에서 금속부식을 보호하기 위한 GO 나노페인트의 전기화학적 특성에 대하여 조사 및 분석하였으며 그 실용적인 적용가능성에 대하여 조사하였다. 이와 같은 연구성과는 GO 나노페인트를 병원 및 위생시설에서 이용하였을 경우에 GO 의 항박테리아 특성에 의하여 지금까지 개발된 상품보다도 친환경, 친위생의 우수한 특성의 상품개발가능성을 보고하였으며, 원천기술확보 및 상품화를 시도하고 있다.

Abstract

Graphene oxide nanosheets become a hot material in material science. Eventhough, this material is well known since 1859 when it was first synthesized by Brodie, the chemistry of this material is not well understood mainly due to its heterogenous and amorphous nature. In this dissertation, a detailed analysis of the chemical and structural investigation of graphene oxide (GO) with different oxidation level was demonstrated in order to understand the types of oxygenated functional groups formed in GO. The surface and electrochemical properties of GO was significantly tuned by controlling the oxidation level.

Different types of reduction routes were employed to synthesize graphene, a well known exciting material in the electronic industry. A facile, and fast method for the reduction of GO into graphene nanosheets using ultrasonic method was demonstrated. A cost effective and efficient route to the synthesis of graphene using hydrothermal method was illustrated. The use of biological reducing agent (galactose) for the reduction of GO was reported. A low temperature, non toxic route for the reduction of GO by hydrogen plasma reduction using a dielectric barrier discharge reactor was developed. A detailed analysis of the graphene synthesized by various routes has been performed with the aid of spectroscopic techniques.

The application of GO nanosheets in the field of photocatalysis was investigated by the measuring the photoreduction of resazurin into resorufin under UV- light irradiation. The antibacterial activity of GO against bacteria and their application in the fabrication of functional antimicrobial textiles was presented. The application of GO thin films for the prevention of metal corrosion has been studied using electrochemical studies. The antibacterial activity of graphene nanosheets

(hydrothermal method) evaluated against pathogenic bacteria by measuring the minimum inhibitory concentration and the results shows their pronounced toxicity towards bacteria. The application of graphene nanosheets (plasma method) towards energy storage devices was examined.

Utilizing nanostructured materials on the road to the development of commercial products with exceptional properties have been rapidly increasing in this decade. Here, we demonstrate the preparation of graphene oxide (GO) paint by entrenching GO nanosheets in alkyd resin using the ball milling method. The intermolecular cross-linking occurred between GO and the lipid chains present in the alkyd resin results in rapid drying time, high-gloss surface and good hiding power of GO paint. The paint formulation with suitable nontoxic additives and their key role in the drying process are discussed. The GO paint coating exhibited corrosion-resistant behavior both in acidic and salt media as examined by immersion and electrochemical corrosion test. It also inhibited the bacterial growth on its surface ensuring the biomedical application of the GO paint. Overall, this strategy for the development of environmentally benign GO paint will create new horizon into the coating industry.

Chapter 1

Introduction

1.1 Graphene oxide nanosheets – a brief

Graphene oxide (GO) is an atomic sheet of graphite decorated by several oxygenated functional groups on its basal planes and at its edges, resulting in a hybrid structure comprising a mixture of sp^2 and sp^3 hybridized carbon atoms [1]. GO can be considered as the insulating and disordered analogue of the conductive graphene [2]. The latter has attracted the interest of physicists due to its unique electronic structure with linear dispersion of Dirac electrons. The insulating and defective nature of GO does not allow the observation of fundamental 2D condensed-matter effects, which limited the interest of physicists in this material [3]. However, this material attracts the chemists and materials scientists due to its heterogeneous chemical and electronic structures, along with the fact that it can be processed in solution. Even though, this material has been well known since 1859 when it was first synthesized by Brodie [4], the material only becomes of widespread interest after the discovery of graphene and is due to the fact it acts as a major precursor for the synthesis of graphene sheets by suitable reduction techniques either chemically or thermally [5].

Apart from the synthesis of graphene, GO has several standalone applications in various fields such as optoelectronics, supercapacitors, memory devices, composite materials, photocatalysis and as a drug delivery agent [6-11]. This has drawn the attention of researchers to explore the intriguing properties of GO nanosheets. The oxidation of graphite results in the decoration of different types of functional groups such as hydroxyl, epoxyl, carbonyl and carboxyl groups in graphene oxide [12]. The

presence of these oxygenated functional groups in GO makes it hydrophilic in nature and also enables them to functionalize other materials with suitable chemistry [13].

GO can be synthesized by the oxidation of graphite into graphite oxide followed by the exfoliation of this graphitic oxide into GO [14]. It is already well known that chemically both graphite oxide and GO have similar or identical structures. Both possess stacked structures with chemical functionality on their basal planes and at their edges. The only difference between them is the number of stacked layers; GO possess a monolayer or just a few stacked layers, while graphite oxide contains a greater number of stacked layers [15]. The formation of oxygenated functional groups in graphite oxide makes them easier to exfoliate into monolayers of GO by simple stirring or mild sonication [16]. The oxidation of graphite to GO breaks up the sp^2 hybridized structure of graphene sheets, and results in the generation of defects that manifest as clear wrinkles in the stack [17] and increase the distance between adjacent sheets from 3.35 A° in graphite powder to 6.8 A° in GO powder [18]. The interlayer spacing varies significantly depending on the amount of water intercalated in between the sheets [19] which further reduces interaction between sheets, thereby facilitating the delamination of graphitic oxide into individual graphene oxide sheets upon exposure to low-power sonication in water or mild stirring. The presence of oxygenated functional groups in GO makes them hydrophilic nature and results in a highly electronegative surface [20].

1.2 Synthesis of graphene oxide:

There are different methods available in literature for the synthesis of graphene oxide. In 1859, the British chemist B. C. Brodie explored the structure of graphite by investigating the reactivity of flake graphite [4]. He performed a reaction

involving ''potash of chlorate'' (potassium chlorate; $KClO_3$) to a slurry of graphite in fuming nitric acid (HNO_3). Finally, he determined that the resulting material was composed of carbon, oxygen, and hydrogen, with an increase in the overall mass of the flake graphite. Brodie found the material to be dispersible in pure or basic water, but not in acidic media, so that he termed the material as "graphic acid" [14].

Nearly 40 years after Brodie's discovery of the ability to oxidize graphite, L. Staudenmaier improved Brodie's method by altering the concentration of $KClO_3$ in the reaction [21]. He used multiple aliquots of $KClO_3$ during the oxidation reaction with addition of addition of concentrated sulfuric acid, to increase the acidity of the mixture. This slight change in the procedure resulted in an overall extent of oxidation similar to Brodie's multiple oxidation approach.

After 60 years, Hummers and Offeman developed an alternate oxidation method by reacting graphite with a mixture of potassium permanganate ($KMnO_4$) and concentrated sulfuric acid (H2SO4), again, achieving similar levels of oxidation [22]. Though, the structure of graphene oxide sheets has been debated for long times with uncertainty due to both the type and distribution of oxygen-containing functional groups. These three methods comprise the primary routes for forming GO. Others have developed slightly modified versions of these methods.

The modified Hummers method is one of the standard methods utilized by many groups for the synthesis of graphene oxide. This method employs an excess of potassium permanganate in the Hummers method which significantly improved the oxidation of graphite [23]. Importantly, it has since been demonstrated that the properties of GO can be varied depending on the oxidants used, reaction time, temperature and also on the graphite source.

1.3 Structure of graphene oxide:

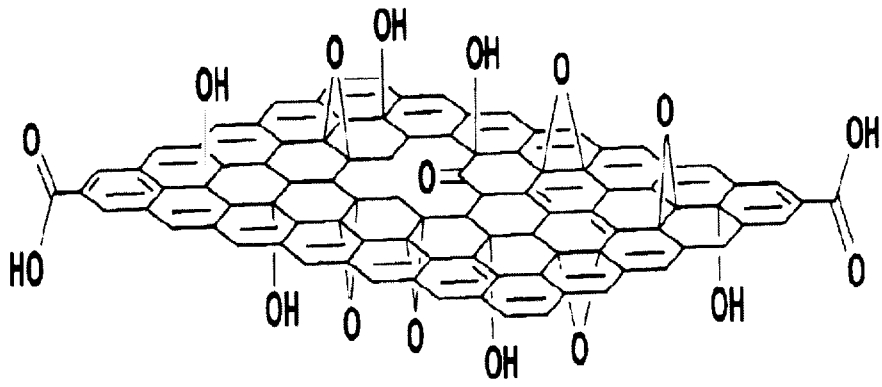

Figure 1.1 Structure of graphene oxide.

The chemical structure of graphene oxide has been a subject of considerable debate in this decade, which is due to the amorphous nature of GO [14,20,24]. The non-stoichiometry of GO make them a complex heterogenous material and there are lot of proposed structure for this material is available in literature [14]. Many scientists based on their experimental and theoretical calculations developed different structure of GO. The mostly cited and well agreed model of graphene oxide is given by the Lerf-Klinowski model [25] as shown in Figure 1.1 It shows that GO consists of different types of oxygenated functional groups on the graphite lattice. The carbonyl and carboxyl groups are present at the edges and the hydroxyl and epoxyl groups are present at the basal planes [26]. These oxygenated functional groups present in GO makes them hydrophilic nature and can be readily dispersed in water or other solvents at molecular level.

1.4 Properties of graphene oxide nanosheets.

1.4.1 Hydrogen bonding networks in GO

GO bearing several oxygenated functional groups are more promising towards the preparation of novel nanocomposites with other polymers and results in exceptional mechanical, electrochemical, thermal properties. The fundamental properties of these exceptional properties relies on the hydrogen bond networks in GO [27]. The molecular dynamics simulations studies of GO nanocomposite paper shows that the properties are controlled by H-bond networks involving both functional groups attached to GO nanosheets as well as water molecules within the interlayer cavities.

1.4.2 GO as a chemical cross-linking agent

GO act as a chemical cross-linking agent for polymers and are used for the preparation of cross-linked graphene sheets in polymer matrix for enhanced mechanical properties [28]. S. Park et al. reported the "Graphene Oxide Sheets Chemically Cross-Linked by Polyallylamine" for excellent mechanical stiffness and strength [29].

1.4.3 GO as a template for nanocrystal growth

GO nanosheets are used as a template for the growth of other nanocrystals and finally results in enhanced properties [30]. This can be achieved by either covalent or non-covalent approaches. Several reports show the promising application of nanocomposite achieved by functionalized graphene shows exceptional properties in diverging applications [31,32].

1.5 Chemically reduced graphene oxide / graphene nanosheets

Graphene, a two-dimensional (2D) single atomic layer of sp^2 bonded carbon atoms [33] has been demonstrated as a promising material because of its unique and outstanding electrical [34,35], thermal [36] and mechanical properties [37]. Its atomic scale thin plane geometry, high carrier mobility and unusual band structure make it an ideal material for applications in future opto-electronic devices [38]. In practice, acquiring large area graphene for future applications such as the integration of high-speed nano-transistors and transparent conducting films are more challenging thing to achieve.

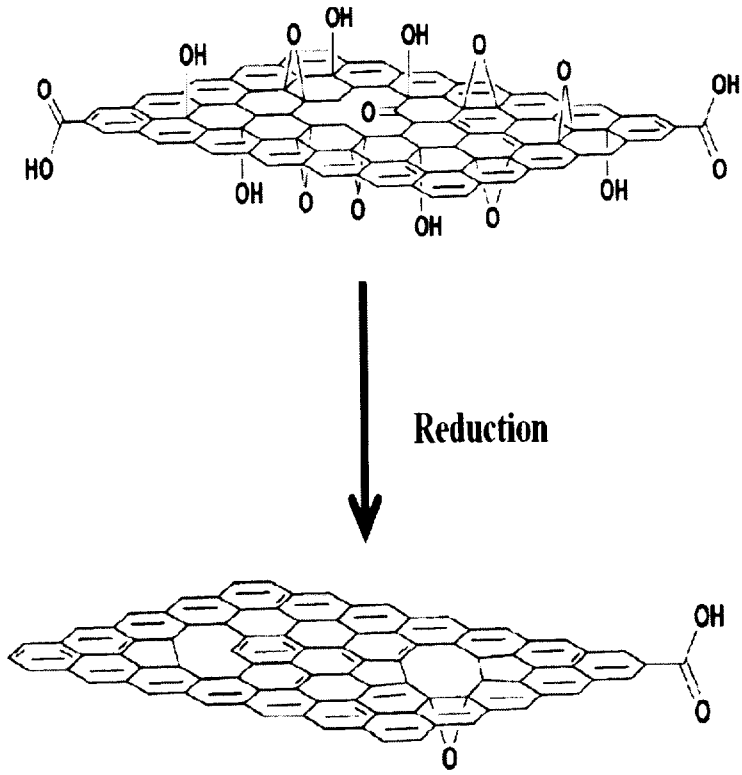

Figure 1.2 Reduction of graphene oxide into graphene.

One of the alternate methods to prepare graphene nanosheets is achieved by reducing graphene oxide (Figure 1.2) using suitable reducing agents [33,39]. Graphene oxide (as discussed above) opens up new possibilities for large scale applications of graphene electronics. Basically, the solution processed GO can be reduced into reduced graphene oxide (rGO), the chemical analogy of crystalline graphene nanosheets by using suitable reduction techniques either by chemically or thermally means. The high temperature for the reduction of GO into graphene limits their commercial application.

There are numerous reducing agents available for the reduction of GO into graphene nanosheets such as hydrazine hydrate, sodium borohydrate etc., [40-42] Some other biological reducing agents such as glucose, fructose, vitamin C are also employed for the reduction of GO [43,44]. Several approaches such as chemical reduction, hydrothermal method, solvothermal method and microwave irradiation method were employed for the reduction of GO into graphene sheets [45-48]. The important parameter in the reduction reaction of GO needs to be focused is the recovery of conjugated π–π^* network in graphene and also the removal of oxygenated functional groups bonded on graphene since they can alter the electronic structure of graphene.

Nowadays, chemists are following combined reduction techniques involving two or three steps of reduction reaction for achieving monolayer graphene sheets [2]. These methods employ sophisticated instruments, high cost, use of toxic gases and longer reaction time [49]. Hence, the development of new synthetic strategy towards the synthesis of 2D graphene with low cost and mild synthetic routes is of great significance and need to be explored.

1.6 Applications of graphene oxide and chemically reduced graphene oxide nanosheets

1.6.1 Energy storage devices

Electrochemical supercapacitors have drawn much attention in recent years due to their high power density, reversibility, long cycle life, and small environmental impact. As a carbon nanomaterial, graphene exhibits many unusual and attractive physical, chemical, and mechanical properties. In particular, these properties make graphene a stronger candidate electrode material for supercapacitor applications than ordinary porous carbon, activated carbon, and carbon nanotubes [50,51].

1.6.2 Flexible resistive switching memory devices

The GO thin films are used for the next generation non-volatile memory devices. The scientific and technological limitations of traditional semiconductor device led the researchers to focus on the carbon based materials for the memory device applications. The preliminary results by C. H. Lee et al. and S. K. Hong et al suggested that GO thin films have a great potential in the future memory device applications [52,53].

1.6.3 Electrochemical Biosensors

The unique electronic and electrochemical properties of graphene and GO make them a suitable candidate for electrochemical biosensors applications. The chemically derived graphene oxide with the nature of single sheets shows a favorable electrochemical activity should be a kind of more robust and advanced carbon electrode material which may hold great promise for electrochemical sensors and biosensors design [54].

1.6.4 Corrosion inhibition coatings

Graphene nanosheets exhibit oxidation resistance of underlying metals [55]. This property of graphene nanosheets makes them favorable towards the corrosion resistant coating applications [56]. However, due to the limitations in large scale productivity of graphene nanosheets, the chemically derived graphene oxide offers a route for the corrosion resistant coating applications. The work by Shin et al shows corrosion resistant coating applications of chemically reduced graphene oxide [57].

1.6.5 Hydrogen storage devices

Graphene-based carbon materials in particular have attracted a great deal of interest as a promising hydrogen storage medium [58]. Theoretical calculations predict that regular or irregular combinations of sp^3-bonded carbon atoms and graphene fragments are advantageous for molecular hydrogen storage [59]. It was also found by ab initio molecular orbital theory and DFT calculations that the physisorption energies are significantly increased on the curved and planar graphenes, respectively [60]. G. Srinivas et al reported the unique property of graphene like nanosheets towards hydrogen storage applications [61].

1.6.6 Biological applications

The electronic properties of graphene and graphene oxide nanosheets are well discussed by many reports. However, the biological applications of these materials are wide-open. Recently, the researchers turned towards the biological applications of these materials. The graphene oxide and graphene nanosheets show promising antibacterial activity towards bacteria [62]. Functionalized graphene nanosheets with antibacterial peptides are used for the detection of bacteria in tooth enamels [63]. Apart from the antibacterial activity, the GO nanosheets with several functional groups are used for potential drug delivery vehicles for the encapsulation of drugs

using suitable guest host chemistry [64]. The biological properties of these materials rely on the chemical structures of graphene oxide and the number of dimensions and also the lateral dimension.

1.7 Focus of current research

Current research mainly focused on the investigation of the properties of graphene oxide and reduced graphene oxide towards multifunctional applications. Scheme 1 represents the focus of current research work done.

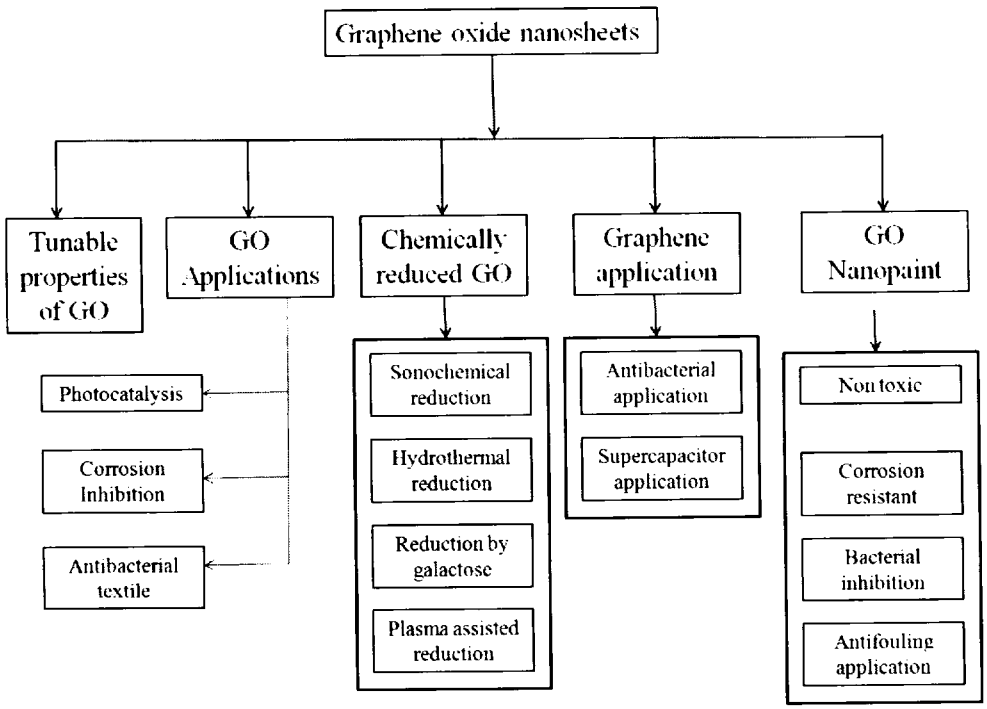

Scheme 1. Focus of current research work.

Briefly, GO nanosheets are synthesized using the Hummers method and we varied the oxidation degree of GO by controlling the amount of oxidizing agent used in the reaction. A detailed analysis using UV-visible spectra, X-ray diffraction studies,

X-ray photo electron spectra, Raman spectra, high-resolution transmission electron microscope have been employed to understand the chemical and structural investigation of GO with different levels of oxidation. The GO synthesized with different oxidation level shows significant variation in the zeta potential. Further, the electrochemical properties revealed that the various oxidation level results in the tunable properties of GO.

Graphene oxide becomes a suitable material for the large scale synthesis of graphene nanosheets, which is well known material in the electronic industry. We then focused different types of reduction methods for the reduction of GO into graphene such as sonochemical reduction, hydrothermal reduction, biological reduction using galactose and plasma assisted redcution. The physico-chemical properties of the graphene synthesized using different reduction methods are investigated well.

We then focused on the applications of GO nanosheets in various fields such as photocatalysis, antibacterial, and corrosion inhibition application. The photocatalytic activity of GO is measured by the UV-assisted photoreduction of resazurin due into resorufin, suggesting GO has a potential application in photocatalysis. GO nanosheets are examined for their antibacterial property against Gram-negative and Gram-positive bacteria. The commercial textile are modified using GO and they also exhibited antibacterial activity. These studied suggest their application towards prevention of health care associated infections. Then we focused on the application of GO towards corrosion prevention of metal. Herein, we used the GO thin films coated on copper foils and the anticorrosion property is studied using electrochemical tests such as Tafel analysis and electrochemical impedance spectroscopic techniques.

We also focused on the potential utility of graphene nanosheets towards the bacterial toxicity. We used the hydrothermally synthesized graphene nanosheets for evaluating their toxicity towards four different types of bacterial species. The minimum inhibitory concentration of graphene nanosheets are compared with the commercial drug kanamycin. The results show graphene nanosheets shows better antibacterial activity towards pathogenic bacteria than the commercial drug which signifies their future application in biomedical field.

The unique electronic property of graphene nanosheets shows promising application in the energy storage devices such as supercapacitors. We evaluated the electrochemical properties of the graphene synthesized by plasma reduction method for their application in energy storage devices. The specific capacitance of the synthesized graphene nanosheets shows 141 F/g.

Utilizing nanostructured materials on the road to the development of commercial products with exceptional properties has been rapidly increasing in this decade. In this regard, we demonstrate the preparation of graphene oxide (GO) paint by entrenching it in alkyd resin using the ball milling method. The GO nanopaint comprises non-toxic additives suggesting their environmentally benign nature. We also studied their application in bacterial growth inhibition, corrosion resistant application etc.

Overall, the research work carried aims at understanding the basic properties of GO and graphene nanosheets, their applications and focused on developing a commercial paint using GO nanosheets for multipurpose applications such as house hold, prevention of metal corrosion, and controlling health care associated infections and also can be used as bottom paints in maritime industries.

REFERENCES

[1] K.A. Mkhoyan, A.W. Contryman, J. Silcox, D.A. Stewart, G. Eda, C. Mattevi, S. Miller, and M. Chhowalla, Nano Lett. **9,** 1058 (2009).

[2] W. Gao, L. B. Alemany, L. Ci, and P. M. Ajayan, Nature Chem. **1**, 403 (2009).

[3] K. P. Loh, Q. Bao, G. Eda, and M. Chhowalla, Nature Chem. **2**, 1015 (2010).

[4] B. C. Brodie, Philos. Trans. R. Soc. London. **149**, 249 (1859).

[5] S. Park and R. S. Ruoff, Nat. Nanotechnol. **4**, 217 (2009).

[6] G. Wang, X. Sun, C. Li, and J. Lian, Appl. Phys. Lett. **99**, 053114 (2011).

[7] K. Krishnamoorthy, R. Mohan, and S. J. Kim, Appl. Phys. Lett. **98**, 244101 (2011).

[8] U. Khan, P. May, A. O. Neill, and J. N. Coleman, Carbon **48**, 4035 (2010).

[9] Q. Cheng, J. Tang, J. Ma, H. Zhang, N. Shinya, and L. C. Qin, Carbon **49**, 2917 (2011).

[10] X. Sun, Z. Liu, K. Welsher, J.T. Robinson, A. Goodwin, S. Zaric, and H. Dai, Nano Res. **1,** 203 (2008).

[11] Z. Liu, J.T. Robinson, X. Sun, and H. Dai, J. Am. Chem. Soc. **130,** 10876 (2008).

[12] S. Stankovich, R.D. Piner, S.T. Nguyen, and R.S. Ruoff, Carbon **44,** 3342 (2006).

[13] Y. T. Fu, S. J. Ming, C. Ching, C. T. Hsiang, T. Hsisheng, Adv. Funct. Mater. **20,** 2255 (2010).

[14] D. R. Dreyer, S. Park, C. W. Bielawski, and R. S. Ruoff, Chem. Soc. Rev. **39**, 228 (2010).

[15] J. Kim, L. J. Cote, F. Kim, W. Yuan, K. R. Shull, and J. Huang, J. Am. Chem. Soc. **132,** 8180 (2010).

[16] G. Wang, B. Wang, J. Park, J. Yang, X. Shen, and J. Yao, Carbon **47**, 68 (2009).

[17] M. J. McAllister, J. L. Li, D. H. Adamson, H. C. Schniepp, A. A. Abdala, J. Liu, M. Herrera-Alonso, D. L. Milius, R. Car, R. K. Prud'homme, and I. A. Aksay, Chem. Mater. **19,** 4396 (2007).

[18] A. B. Bourlinos, D. Gournis, D. Petridis, T. Szabo, A. Szeri, and I. Dekany, Langmuir **19,** 6050 (2003).

[19] W. Scholz, H. P. Boehm, Z. Anorg. Allg. Chem. **369,** 327 (1969).

[20] O. C. Compton, and S. T. Nguyen, Small **6,** 711 (2010).

[21] L. Staudenmaier, Ber. Dtsch. Chem. Ges. **31**, 1481 (1898).

[22] W. S. Hummers, and R. E. Offeman, J. Am. Chem. Soc. **80**, 1339 (1958).

[23] M. Hirata, T. Gotou, S. Horiuchi, M. Fujiwara, and M. Ohba, Carbon **42**, 2929 (2004).

[24] S. Wang, R. Wang, X. Liu, X. Wang, D. Zhang, Y. Guo, and X. Qiu, J. Phys. Chem. C. **116**, 10702 (2012).

[25] H. Y. He, J. Klinowski, M. Forster, and A. Lerf, Chem. Phys. Lett. **287,** 53 (1998).

[26] A. Lerf, H. He, M. Forster, and J. Klinowski, J. Phys. Chem. B **102,** 4477 (1998).

[27] N. V. Medhekar, A. Ramasubramaniam, R. S. Ruoff, and V. B. Shenoy, ACS Nano **4,** 2300 (2010).

[28] S. Park, K.-S. Lee, G. Bozoklu, W. Cai, S. T. Nguyen, and R. S. Ruoff, ACS Nano **2,** 572 (2008).

[29] S. Park, D. A. Dikin, S. T. Nguyen, and R. S. Ruoff, J. Phys. Chem. C, **113,** 15801 (2009).

[30] H. Wang, J. T. Robinson, G. Diankov, and H. Dai, J. Am. Chem. Soc., **132,** 3270 (2010).

[31] R. Liu, S. Liang, X.-Z. Tang, D. Yan, X. Li, and Z.-Z. Yu, J. Mater. Chem. **22,** 14160 (2012).

[32] E. Peng, E. S. G. Choo, P. Chandrasekharan, C.-T. Yang, J. Ding, K.-H. Chuang, J. M. Xue, Small (2012) DOI: 10.1002/smll.201201427.

[33] A. K. Geim, and K. S. Novoselov, Nat. Mater. **6,** 183 (2007).

[34] C. Soldano, A. Mahmood, and E. Dujardin, Carbon **48,** 2127 (2010).

[35] K. S. Novoselov, A. K. Geim, S. V. Morozov, D. Jiang, Y. Zhang, S. V. Dubonos, I. V.
Grigorieva, and A. A. Firsov, Science **306,** 666 (2004).

[36] A. A. Balandin, S. Ghosh, W. Z. Bao, I. Calizo, D. Teweldebrhan, F. Miao, and C. N. Lau, Nano Lett. **8,** 902 (2008).

[37] I. W. Frank, D. M. Tanenbaum, A. M. van der Zande, and P. L. McEuen, J. Vac. Sci. Technol. B **25,** 2558 (2007).

[38] P. Avouris, Z. Chen, and V. Perebeinos, Nat. Nanotechnol. **2,** 605 (2007).

[39] Z. Wei, D. Wang, S. Kim, S.-Y. Kim, Y. Hu, M. K. Yakes, A. R. Laracuente, Z. Dai, S. R. Marder, C. Berger, W. P. King, W. A. de Heer, P. E. Sheehan, and E. Reido, Science **328,** 1373 (2010).

[40] M.C. Kim, G.S. Hwang, and R.S. Ruoff, J. Chem. Phys. **131,** 064704 (2009).

[41] S. Stankovich, D.A. Dikin, R.D. Piner, K.A. Kohlhaas, A. Kleinhammes, Y. Jia, Y. Wu, S.T. Nguyen, and R.S. Ruoff, Carbon **45,** 1558 (2007).

[42] H.-J. Shin, K. K. Kim, A. Benayad, S.-M. Yoon, H. K. Park, I.-S. Jung, M. H. Jin, H.-K. Jeong, J. M. Kim, J.-Y. Choi, and Y. H. Lee, Adv. Funct. Mater. **19,** 1987 (2009).

[43] C. Zhu, S. Guo, Y. Fang, and S. Dong, ACS Nano, **4,** 2429 (2010).

[44] M. J. F. Merino , L. Guardia, J. I. Paredes, S. V. Rodil, P. S. Fernandez , A. M. Alonso, and J. M. D. Tascon, J. Phys. Chem. C, 114, 6426 (2010).

[45] Y. Zhou, Q. Bao, L. A. L. Tang, Y. Zhong, and K. P. Loh, Chem. Mater. **21,** 2950 (2009).

[46] Y. Zhu, S. Murali, M. D. Stoller, A. Velamakanni, R. D. Piner, and R. S. Ruoff, Carbon **48,** 2118 (2010).

[47] Z. Lei, L. Lu, and X. S. Zhao, Energy Environ. Sci. **5,** 6391 (2012).

[48] A. V. Murugan, T. Muraliganth, and A. Manthiram, Chem. Mater. **21,** (2009) 5004.

[49] J. Zhang, H. Yang, G. Shen, P. Cheng, J. Zhang, and S. Guo, Chem. Commun. **46,** 1112 (2010).

[50] B. Xu, S. Yue, Z. Sui, X. Zhang, S. Hou, G. Cao, and Y. Yang, Energy Environ. Sci., **4**, 2826 (2011).

[51] A. Chidembo, S. H. Aboutalebi, K. Konstantinov, M. Salari, B. Winton, S. A. Yamini, I. P. Nevirkovets, and H. K. Liu, Energy Environ. Sci., 2012,**5,** 5236-5240

[52] C. L. He, F. Zhuge, X. F. Zhou, M. Li, G. C. Zhou, Y. W. Liu, J. Z. Wang, B. Chen, W. J. Su, Z. P. Liu, Y. H. Wu, P. Cui, and Run-Wei Li, Appl. Phys. Lett. **95,** 232101 (2009).

[53] S. K. Hong, J. E. Kim, S. O. Kim, and B. J. Cho, Journ. Appl. Phys. **110,** 044506 (2011)

[54] M. Zhou, Y. Zhai, and S. Dong, Anal. Chem. **81,** 5603 (2009).

[55] S. Chen, L. Brown, M. Levendorf, W. Cai, S.-Y. Ju, J. Edgeworth, X. Li, C. W. Magnuson, A. Velamakanni, R. D. Piner, J. Kang, J. Park, and R. S. Ruoff, ACS Nano **5,** 1321 (2011).

[56] D. Prasai, J. C. Tuberquia, R. R. Harl, G. K. Jennings, and K. I. Bolotin, ACS Nano **6,** 1102 (2012).

[57] D. Kang, J. Y. Kwon, H. Cho, J.-H. Sim, H. S. Hwang, C. S. Kim, Y. J. Kim, R. S. Ruoff, and H. S. Shin, ACS Nano **6,** 7763 (2012).

[58] L. P. Ma, Z. S. Wu, J. Li, E. D. Wu, W. C. Ren, and H. M. Cheng, Int. J. Hydrogen Energy 34, 2329 (2009).

[59] N. Park, S. Hong, G. Kim, and S. H. Jhi, J. Am. Chem. Soc.**129,** 8999 (2007).

[60] Y. Okamoto, and Y. Miyamoto, J. Phys. Chem. B.**105,** 3470 (2001).

[61] G. Srinivas, Y. Zhu, R. Piner, N. Skipper, M. Ellerby, and R. Ruoff, Carbon **48,** 630 (2010).

[62] W. Hu, C. Peng, W. Luo, M. Lv, X. Li, D. Li, Q. Huang, and G. Fan, ACS Nano **4,** 4317 (2010).

[63] M. S. Mannoor, H. Tao, J. D. Clayton, A. Sengupta, D. L. Kaplan, R. R. Naik, N. Verma,
F. G. Omenetto, and M. C. McAlpine, Nature Comm. **3**, Article number: 763, (2012) doi:10.1038/ncomms1767.

[64] X. Yang, Y. Wang, X. Huang, Y. Ma, Y. Huang, R. Yang, H. Duan, and Y. Chen, J. Mater. Chem. **21**, 3448 (2011).

Chapter 2

Experimental methods

2.1. Introduction

This chapter provides detailed information on the experimental procedures used for the synthesis of graphene oxide, controlled degrees of oxidation and reduction of graphene oxide by various methods. In addition the preparation of GO nanopaint is also discussed in detail.

2.2 Materials used

Graphite powder was purchased from Sigma Aldrich Ltd. Potassium Permanganate ($KMnO_4$), sulfuric acid (H_2SO_4), hydrogen peroxide (H_2O_2), and hydrochloric acid (HCl) were obtained from Dae Jung chemicals & metal Co., Ltd, South Korea. All the chemicals used in this research were research grade.

2.3 Synthesis of graphene oxide nanosheets

The graphene oxide nanosheets were synthesized according to the modified Hummer's method using graphite powder as the starting material [1]. Briefly, graphite powder (2 g) was stirred in 98% H_2SO_4 (35 mL) for 1 h. Then, $KMnO_4$ (6 g) was gradually added to the above solution while keeping the temperature less than 20 °C. The mixture was then stirred at 35 °C for 30 min. The resulting solution was diluted by adding 90 mL of water under vigorous stirring and a dark brown color suspension was obtained. The reaction was terminated by the addition of 150 mL of distilled water and 30% H_2O_2 solution (5 mL). After continuously stirred for 2 hrs, the mixture was washed by repeated centrifugation and filtration using 5% HCl aqueous solution in order to remove the metal ions. Further, the centrifugation process was repeated

with distilled water until the pH of the solution becomes neutral. The obtained brown colored precipitate is graphitic oxide and is dried under vacuum. Finally, 160 mL of water was added to the resulting precipitate and sonicated well in a probe type sonicator nearly 1 h to obtain a uniform suspension of graphene oxide.

2.4 Synthesis of graphene oxide nanosheets with controlled oxidation

GO was synthesized using the harsh oxidation of graphite according to the modified Hummers method [1]. The amount of oxygenated functional groups in the GO was varied by changing the amount of $KMnO_4$ from 1 g to 6 g with an increment of 1 g per oxidation level (The other parameters in the reaction were kept constant). In total, 6 different oxidation levels were synthesized; these were denoted as S-1, S-2, S-3, S-4, S-5 and S-6 where the numbers of the samples indicate the amount (in grams) of $KMnO_4$ used in the oxidation reaction.

2.5 Sonochemical reduction of graphene oxide into graphene nanosheets

The as-synthesized GO nanosheets were used as the starting precursor for the synthesis of graphene via sonochemical method. Briefly, the pH of the as exfoliated GO solution (0.2 g in 200 mL) was adjusted to reach 10 by NaOH solution followed by the addition of 2 mL of hydrazine and the entire reaction is subjected to ultrasound irradiation for 2 hr. The obtained graphene nanosheets was washed thoroughly with distilled water and centrifuged at 12000 rpm for 10 minutes in order to remove the residuals. The procedure was repeated for several times until the synthesized product becomes free from trace amount of impurities. Further, the synthesized graphene nanosheets were dried in a hot air oven and were used for further characterization. The graphene or reduced graphene oxide nanosheet synthesized by ultrasonic method

is named as US-rGO. In order to confirm the reduction reaction and the rate kinetics were enhanced in the presence of ultrasound, we also examined the same reduction reaction in the absence of ultrasound. The experiments were performed with the same concentration in the absence of ultrasound irradiation.

2.6 Hydrothermal reduction of GO into graphene nanosheets.

The reduction of GO into graphene nanosheets was achieved by the hydrothermal method. Briefly, 0.05 gm of as-synthesized GO nanosheets were dispersed in 50 mL of deionized water and were irradiated by ultrasound for 30 min in order to achieve uniform dispersion of GO. Then the pH of the solution was adjusted to reach 10 by the addition of NaOH (KOH can also be used) solution followed by the addition of 2 ml of hydrazine hydrate solution. Then, the solution is transferred into a Teflon vessel covered by a stainsteel reactor and kept at a constant temperature of 90 °C for 10 hrs. After the hydrothermal reaction, the obtained graphene nanosheets were washed thoroughly with distilled water and centrifuged at 12000 rpm for 10 minutes in order to remove the residuals. The procedure was repeated several times until the synthesized product became free from trace amount of impurities. Further, the graphene nanosheets were dried in a hot air oven at 150 °C for 2 h in order to remove the water content.

2.7. Synthesis of reduced graphene oxide by D-galactose

The rGO was synthesized from GO using an eco friendly method by employing galactose as a reducing agent. Briefly, galactose (0.4 g) is gradually added to the aqueous solution of GO (0.5 mg/mL) and is allowed to constant stirring for 30 min resulting in a color change from brown to black. Then, 0.2 mL of ammonia is added to the solution and allowed to heat at 70 °C for 1 hour. Finally, the black

precipitate of rGO obtained was centrifuged at an rpm of 5000 and washed three times with deionized water.

2.8 Plasma assisted reduction of GO

Briefly, the atmospheric pressure dielectric barrier discharge (DBD) plasma reactor used in this study consisted of two stainless steel plates (width: 40 mm; length: 150 mm; thickness: 1 mm) acting as electrodes and two 1.5-mm thick glass plates serving as dielectric barrier, which is represented in Figure 1.1 (a). The two stainless steel electrodes were 15 mm apart. The DBD plasma reactor prepared as mentioned above was energized by an alternating current (AC) high voltage in the range of 16 to 20 kV (peak value) to create plasma. The DBD plasma reactor was placed in an acrylic chamber equipped with gas inlet and outlet. The gas for the generation of plasma was Ar, and H_2 was used as a reducing agent. The flow rates of Ar and H_2 fed to the DBD plasma reactor were controlled by mass flow controllers (MKS Instruments, Inc.). About 0.15 g of GO nanosheets was kept in a Petri-dish and was loaded between the electrodes of the plasma reactor. Prior to plasma ignition, Ar and H_2 gas (with the flow rate of 60 and 15 standard cubic centimeters per minute-sccm, respectively) was flowed into the plasma chamber for nearly 10 min in order to remove the atmospheric gases already present inside. Then, high voltage of about 16 to 20 kV was applied to the electrodes at a frequency of 400 Hz to ignite the plasma. The reaction was allowed to proceed for 3 h. Finally, the resulting powder were collected and used for further studies. The actual discharge power dissipated in the plasma reactor was calculated from the area of the Lissajous curve, also called charge-voltage plot (as shown in Figure 1.1 (b)) generated in the oscilloscope (*Tektronix MSO/DPO3000)*, which was determined to be about 14.6 W.

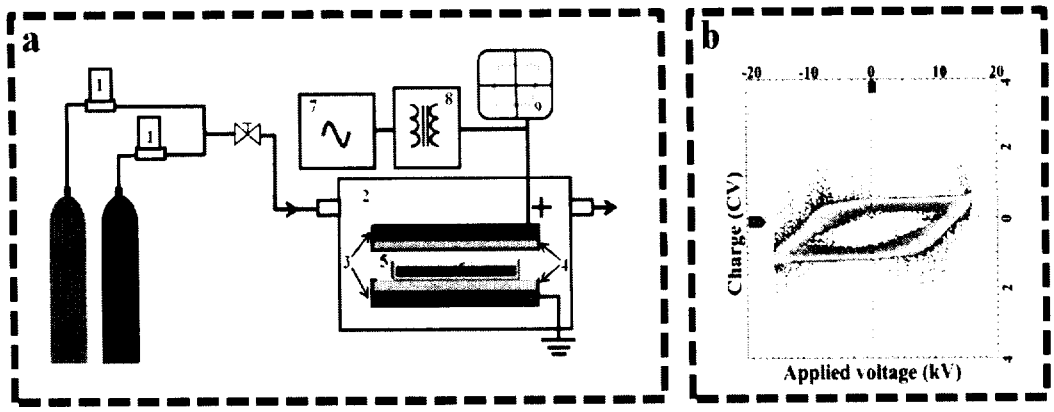

Figure 1.1 (a) Experimental set up for plasma treatment of Graphene oxide in a DBD discharge reactor. 1. Mass flow controllers 2. DBD plasma reactor 3. Electrodes 4. Glass (dielectric) 5. Plasma 6. Graphene Oxide 7. High-voltage transformer 8. Variable transformer 9. Oscilloscope. (b) Lissajous V-Q figure during the plasma reaction. Capacitor and the applied frequency values were 0.86 μF and 400 Hz, respectively.

2.9 Instrumentation

XRD characterization was performed on a X-ray Diffractometer System (D/MAX 2200H, Bede 200, Rigagu Instruments C). The FT-IR spectrum (1000–2000 cm^{-1}) was measured using a Thermo scientific FT-IR spectrometer with pure KBr as the background. The samples were mixed with KBr and the mixture was dried and compressed into a transparent tablet for measurement. The surface morphology of all the samples was analyzed using a high resolution transmission electron microscope (HR-TEM, FEI Titan 80-300) and a bioatomic force microscope (AFM: Nanowizard II, JPK instruments). The chemical composition and the state of elements present in the outermost parts of the GO nanosheets were investigated by XPS measurements using an ESCA- 2000, VG Microtech Ltd. Here a monochromatic X-ray beam source at 1486.6 eV (Aluminum anode) and 14 kV was used to scan the sample surface. A

high flux X-ray source with an Aluminum anode was used for X-ray generation, and a quartz crystal monochromator was used to focus and scan the X-ray beam on the sample. The zeta potential measurements of the samples in an aqueous dispersion were performed on Malvern Instruments. The Raman spectra were recorded with a RENISHAW (M005-141) Raman system with laser frequency of 514 nm as an excitation source. The laser spot size was 1 μm and the power at the sample was kept to below 10 mW, in order to avoid laser induced heating. The ultrasound irradiation for the exfoliation of the graphitic oxide into monolayers of GO was carried out on a SONIC VCX 750 model (20 kHz, 750 W) using a direct immersion titanium horn.

2.10 Electrochemical measurements of GO with various oxidation level

The electrochemical properties of all the samples were studied by cyclic voltammetry (CV) measurements using an AUTOLAB PGSTAT320N system with a three-electrode configuration containing a glassy carbon electrode (GCE) as the working electrode, and platinum and an Ag/AgCl electrode as the counter and reference electrodes, respectively. Prior to GO casting, the GCE electrode, was polished with alumina powder, and then rinsed thoroughly, and finally blow dried with N_2. A 5 μL suspension of GO samples was spread on the pretreated bare GCE using a micropipette and the film was allowed to dry in a vacuum desiccator. All the electrochemical measurements were recorded in a 5 mM $K_3[Fe(CN)_6]$ solution containing 0.1 of KCl solution in the potential range of -0.2 to +0.6 V. A reproducible voltammogram can be obtained under steady-state conditions after about five cycles.

2.11 Measurement of photocatalytic activity of GO nanosheets

The photocatalytic activity of GO was evaluated by measuring the photoreduction of RZ as a function of irradiation time under UV light (350 nm). The photocatalysis experiment was carried out in glass reactors containing 10 ml of RZ aqueous solution at a concentration of 1.5 μg/ml with various concentration of GO (0.5 mg, 0.75 mg, and 1 mg). The solution was stirred well and allowed to UV-irradiation at regular intervals and the corresponding absorption spectra were measured. Both the concentration dependent and time dependent photocatalytic activity of GO were examined.

2.12 Antibacterial activity of GO nanosheets and development of functional textiles

2.12.1 Bacterial strains used

E. coli DH5α is obtained from Department of Marine Life Sciences, Jeju National University, Republic of Korea. *S. iniae* was gifted by professor Sung-Ju Jung, Department of Aqualife Medicine, Chonnam National University, Republic of Korea.

2.12.2 Growth of bacterial strains

Gram-negative bacteria *Escherichia coli* (DH5α) and Gram-positive bacteria *Streptococcus iniae* were cultured in LB agar (Luria Bertani broth containing 1.5% agar) plate at 37 °C and brain heart infusion agar plate at 30 °C, respectively. Single colony was inoculated into 5 mL of the respective broth and cultured overnight at appropriate temperature. This culture was seeded to further grow the bacteria in a final volume of 50 mL. When optical density (OD_{600}) reached 0.6, cells were harvested by centrifugation at 3500 rpm for 30 min at 4 °C. The harvested cells were washed twice with saline solution (0.9% NaCl) to remove the residual media

components and then resuspended with saline. Finally cells were spectrophotometrically (Bio-Rad, USA) quantified.

2.12.3 Assay for antibacterial activity of GO nanosheets

a) Disc Diffusion Method:

At first, the antibacterial activity of GO nanosheets was evaluated by the disc diffusion method [2]. Gram-negative bacteria *Escherichia coli* (DH5α) and Gram-positive bacteria *Streptococcus iniae* were cultured in LB agar (Luria Bertani broth containing 1.5% agar) plate at 37 °C and brain heart infusion agar plate at 30 °C, respectively. Single colony was inoculated into 5 mL of the respective broth and cultured overnight at appropriate temperature. The bacteria were diluted with saline to a final concentration of ~10^7 cells/mL and 100 µL was spread on the respective agar plates using sterile cotton swab. The discs impregnated with different concentrations (100, 500 and 1000 µg/mL) of the GO were placed on agar. The disc impregnated with saline was used as negative control. The plates were incubated overnight at appropriate temperature. Antibacterial activity was measured by the zone of inhibition around the disc with the following formula:

$$H = (D-d)/2 \quad \text{..... [1]}$$

where H is the length of inhibition zone (mm); D is the total diameter of the zone of inhibition (mm); d is the diameter of disc (mm).

b) Colony counting Method:

A quantitative colony counting method is also employed for determining the antibacterial activity of GO nanosheets [3]. The microorganisms (~10^7 cells/mL) were incubated with different concentration of GO (25-150 µg/mL) in saline at 200 rpm and appropriate temperature for 3 h. After incubation, bacteria were serially diluted with saline up to 10^4 cells/mL. 100 µL of this solution was spread on the respective

agar plates and incubated overnight at appropriate temperature. The colony forming units (CFU) were counted from each plate and the antibacterial activity was expressed as a function of cell viability loss. The loss of cell viability (%) was determined using the number of colonies found in the experimental mixture incubated with GO and the number of colonies found in the blank, incubated without GO. The experiments were done in triplicate and the average values were reported.

2.12.4 Surface modification of textiles using GO nanosheets

The surface modification of cotton fabrics by GO nanosheets was achieved using a facile approach comprising of dip coating via stirring [4]. Briefly, the cotton fabric (3 × 4 cm dimension) was immersed into the solution containing (0.25 g of GO in water) and allowed to vigorous stirring at 300 rpm for 24 hr. After that, the GO coated fabric was taken from the solution and washed three times with deionized water for the removal of residual GO on the surface. The resulting fabric was allowed to dry at 35 °C for 1 day in a vacuum desiccator. The amount of GO coated into the fabric was calculated by weight method by employing the formula given below:

Amount of GO loaded into the fabric = W_2-W_1 ..... [2]

Where W1 - Initial weight of GO coated cotton fabrics

W2 - Final weight of GO coated cotton fabrics

2.12.5 Antibacterial property of GO coated cotton fabrics:

The modified Hohenstein method was adopted to evaluate the antibacterial activity of GO coated fabrics against both Gram positive (*S. iniae*) and Gram negative (*E.coli* DH5α) models [5]. Bacterial strains were resuspended in saline solution with a final bacterial cell concentration of ~10^7 cells/mL. Cotton fabrics specimens were added into the tube and ensured it was fully immersed in inoculums. The mixture was

then incubated at 200 rpm at species specific temperatures for 24 h. A blank was arranged for each strain without adding the coated fabrics specimen and just before taking the inoculums for plating, coated cotton fabrics were added in such a way to acquire the data at 'zero contact time'. The reduction in the bacterial concentration incubated with the specimens in different standard time intervals of 6, 12 and 24 h was measured. The anti-bacterial potential of the GO particle coated cotton fabrics was determined by comparing the reduction in viable bacterial population of the coated fabric specimen to that of control sample and expressed as a percentage reduction in standard time intervals. The inoculum was serially diluted up to 10^4 cells/mL and uniformly spread on respective media plates at different cell concentrations (with blanks). Plates were incubated for overnight at species specific temperatures. The colony forming units (CFU) were counted from a series with optimum cell population. Evaluation was carried out on the basis of a modified method of Hohenstein test and the percentage reduction was calculated using the following formula:

$$R = ((B-A) / B)\times 100 \quad \text{..... [3]}$$

where R is percentage reduction; A is the number of bacteria recovered from the broth inoculated with GO coated cotton fabric specimen and B is the number of bacteria recovered from the broth inoculated with control fabrics (pure cotton fabrics) specimen after the desired contact period (6, 12 and 24 hours) immediately after inoculation.

2.12.6 Lipid peroxidation measurement

The free-radical modulation activity of GO was determined using a lipid peroxidation assay [6]. Briefly, lipid peroxidation was induced in liposomes prepared by ultrasonic irradiation from egg lecithin by adding 5 μL of 400 mM FeCl3 and 5 μL

of 200 mM L-ascorbic acid. To this, the appropriate concentration of test materials (GO and graphene) were added. The control containing no compound was prepared. The samples were incubated at 37 °C for 60 minutes. The reaction was inhibited by adding 1 mL of stopping solution containing 0.25M HCl, 1.5% (vol/vol) trichloroacetic acid, and 0.375% (wt/vol) thiobarbituric acid. These reaction mixtures were kept in a boiling-water bath for 15 minutes, cooled, and centrifuged. The absorbance of the resulting solution was measured at 532 nm.

2.13 Corrosion inhibition studies of GO thin films

2.13.1 Preparation of thin films of GO nanosheets

The GO thin film was made by using drop casting method over a copper foil (Nilaco corporation, Tokyo, Japan) which is used as a substrate [7]. Briefly, appropriate amount of GO in 80:20 (v/v) of water and ethanol was sonicated for 30 min for attaining uniform suspension. Then, 100 µL of GO dispersion is drop casted into the copper foil and is allowed to dry at 80 ^{o}C for 30 min. After the evaporation of solvent, uniform thin films of GO are formed on the copper foil. The hydrophilic nature of GO thin films allows them to be adhesive with substrates in the form of thin film.

2.13.2 Electrochemical studies for corrosion analysis

Potentiodynamic polarization and electrochemical impendence spectroscopy measurements were performed on Autolab PGSTAT galvanostat / potentiostat system. A three electrode electrochemical cell was used with a platinum counter electrode and silver/silver chloride (Ag/AgCl) electrode as the reference electrode. The bare copper substrate and GO coated copper substrates are used the working electrode. The sample was loaded in a Teflon sample holder and the surface area exposed to the corrosive medium was 1 cm^2. All the electrochemical tests were performed in 3.5%

NaCl solution at room temperature. The sample was kept in the solution for 60 min prior to the potentiodynamic polarization study in order to establish the open-circuit potential (E_{ocp}) or the steady state potential. After obtaining the stable open-circuit potential, the upper and the lower potential limits of linear sweep voltammetry were set at (±200 mV respectively, with respect to the E_{ocp}). The sweep rate was 1 mV/s. The Tafel plot was obtained after the electrochemical measurements. The corrosion potential (E_{corr}) and the corrosion current density (I_{corr}) were deduced from the Tafel plot [8]. The electrochemical impedance spectroscopy (EIS) measurements were conducted using a frequency response analyzer. The spectrum was recorded in the frequency range of 10 mHz–100 kHz with a data density of 5 points per decade. The applied alternating potential had root-mean square amplitude of 10 mV on the E_{corr}. After each experiment, the impedance data were displaced as Nyquist and Bode plots. The Nyquist plot is a plot of real (Z') Vs imaginary impedance (Z'') values. From this plot, at high frequency the value of solution resistance (R_s) is obtained and at low frequency the charge-transfer resistance (R_{ct}) is deduced.

2.14 Antibacterial activity of graphene nanosheets

The graphene nanosheets synthesized by hydrothermal reduction of GO as discussed in section 2.7 is used in this study.

2.14.1 Bacterial strains

The as-synthesized graphene nanosheets were tested for anti-bacterial activity in comparison with a standard drug, kanamycin (aminoglycoside antibiotic). Four pathogenic bacterial strains including Gram-negative strains such as *Escherichia coli* (KACC 10005) and *Salmonella typhimurium* (KCCM 40253) and also Gram-positive

strains such as *Bacillus subtilis* (KACC 14394) and *Enterococcus faecalis* (KACC 13807) were utilized in the study.

8.14.6 Test of antibacterial properties and measurement of minimum inhibitory concentration (MIC) of graphene nanosheets

The anti-bacterial activity of the samples was determined by the micro dilution method [9]. LB broth was used as the diluent for the bacterial strains. Inoculates were prepared by suspending growth from overnight cultures in sterile LB media. The two fold dilution of samples and standard in the 96 well plates were prepared and denoted as graphene nanosheets and kanamycin. Approximately 10^7 CFU/mL cells were inoculated; the final volume in each micro well plate was 0.2 mL and was incubated at 35 °C for 24 h. The microwell plates were read at 590 nm using the ELISA reader before and after incubation to determine their MIC values. The MIC is defined as the lowest concentration of an anti-microbial agent that allows no growth of a microorganism after overnight incubation when compared with that of the control. The MIC of an antimicrobial drug corresponds to a lowered bacterial density from 10^7 to at least 10^2 CFU/mL (i.e, a 99.9% [3-$\log_{10}$] reduction in bacterial inoculum) [10]. The experiments were performed in triplicate and were repeated twice.

The free radical modulation activity of graphene nanosheets was determined using a lipid peroxidation assay as discussed in section 2.11.6.

Data was analyzed using Biostat software (AnalystSoft Inc., Vancouver, British Columbia, Canada) for one-way analysis of variance for the statistical significance of the model ($P<0.05$).

2.15 Supercapacitor performances of graphene nanosheets

The graphene nanosheets synthesized by hydrogen plasma assisted reduction of GO as discussed in section 2.7 is used for this study.

2.15.1 Electrode fabrication and electrochemical studies

The electrochemical studies such as cyclic voltammetric analysis, electrochemical impedance spectra (EIS) and galvanostatic charge-discharge analysis were carried out in AUTOLAB PGSTAT302N electrochemical work station. For these studies, the active material graphene, acetylene black, and PVDF were taken in the weight ratio of 85:10:5. All these were mixed together using NMP (N-methylpyrrolidone) as a solvent and was made into a slurry. Then, the slurry is coated onto the graphite sheet with the area 1×1 cm^2 and allowed to evaporate the solvent an overnight drying process. The electrochemical analysis was carried out in three-electrode configuration with graphene-coated graphite sheet, Pt, Ag/AgCl as working, counter, and reference electrodes, respectively. Here, we used 1M solution of potassium chloride (KCl) as the electrolyte. The EIS experiments were conducted at a frequency range of 0.1 Hz to 100 kHz with applied potential amplitude of 10 mV.

2.16 GO nanopaint

2.16.1 Materials used

The additives used in GO paint are Linseed alkyd resin (Sunny Paints and Tar Products, India), Thickener A (Vigneshwara Paints Ltd, India), Soya lecithin (Shreenidhi Oils and Foods Ingredients Pvt. Ltd., India), Mineral turpentine oil (Indian Oil Corporation, India), aluminum stearate (Sigma Aldrich, India) and Cobalt

napthenate (Sigma Aldrich, India). The zinc oxide and zirconia used in this study are nanoparticles synthesized by the method reported elsewhere [6,11].

2.16.2 Preparation of GO paint

The GO nanosheets embedded alkyd paints are prepared by ball milling approach (Pulverisette 6.0 instrument, Germany). The composition of paint prepared using GO as pigment with other additives such as binder, thickener, wetting agent, inner coat drier, upper coat drier, thinner, stabilizer are given in Table. 1. The constituents of the paints as shown in Table 1 (except the thinner) are taken in a tungsten carbide bowl and milled using tungsten carbide balls. The ball to powder ratio (BPR) is maintained as 10:1 with milling speed of about 300 rpm for 5 h time duration. After that, thinner is added and the milling is continued for 30 min which results in the formation of black colored GO paint. The final product was collected and stored in air tight container and used for further characterization.

2.16.3 Coating of GO paint

The prepared GO paint can be applicable to coat any type of surface including glass, metal substrates, flexible substrates and floors etc. In our experiments, we coated the GO paint on GI substrates for the corrosion test. Prior to coating, the GI substrates were pretreated by pickling at 50 °C in acid (1N sulphuric acid) followed by rinsing with water to remove the surface contaminants. Then, the substrates were polished using emery sheet followed by cleaning with thinner. After these cleaning steps, the substrates were coated with GO paint using brush coating method. For antibacterial studies, the GO paint is coated on glass plates.

2.16.4. Gloss measurement and hiding power of the GO paint

The hiding power and gloss measurement of the GO paints were examined by applying known amount (1 g) of paint on a commercially available drawdown card

using multifunctional film applicator and are compared with the commercially available black color paint [12]. The thickness of the paint coatings was controlled by the multifunctional film applicator as 150 µm. Briefly, 1 g of paint was placed on the drawdown card and is allowed to drawdown using thin film applicator and is allowed to dry at room temperature. The hiding power of the paint was observed from the coated paint on drawdown card whether the background color was covered by the paint or not. The gloss measurements were carried out on Rajdhani digital gloss meter (RSPT-200 model, INDIA) instrument. All these measurements were carried out at Vigneshwara Paints Pvt. Ltd, Tamilnadu, India.

2.16.5 Solid content of the paint:

The solid content of the paint is the ratio of total weight of the solid ingredient in the paint to the total weight of the total ingredients in the paint. The quantity of solid content present in the paint was determined by drying 1 gram of paint in a cleaned, dry watch glass. Based on the initial and final weight measurements, the solid content percentage of both GO and commercial paint were evaluated using the following relation:

$$\text{Solid content of paint (\%)} = [W_2 / W_1] \times 100 \quad \ldots\ldots [4]$$

Where W_1 = Initial weight of the paint.

W_2 = Final weight of paint after drying.

2.16.6 Corrosion inhibition test - Acid immersion method:

The corrosion inhibition test was examined using the weight loss method [13]. Briefly, two types of substrates were used to study the corrosion inhibition efficiency viz. (i) bare GI substrate (ii) bare GI substrate coated with GO paint. The substrates were immersed in 0.1 N HCl solution for 24 h at room temperature After 24 h, the substrates were taken out from the beakers and immersed in distilled water for the

removal of acidic impurities and dried in room temperature. The weight of each substrate before and after the reaction was measured and is used for the calculation inhibition efficiency. The corrosion inhibition efficiency of GO paint coating is calculated using the formula [13].

$$\text{Inhibition efficiency } \% = [(W_{uncoated}-W_{coated})/W_{uncoated}] \times 100 \ldots\ldots\ldots\ldots [5]$$

where $W_{uncoated}$ = weight loss in bare substrate.

W_{coated} = weight loss in GO paint coated substrate.

2.16.7 Electrochemical corrosion studies

The corrosion behavior was studied by potentiodynamic polarization measurement using an Autolab PGSTAT galvanostat/potentiostat system [14]. The measurements were performed in a 3.5% NaCl solution electrolyte at room temperature. A conventional three-electrode cell was used with the platinum counter electrode and a silver/silver chloride (Ag/AgCl) as a reference electrode and the test sample (with an exposed area of 1 cm^2) as the working electrode. Prior to the polarization measurements, open circuit potential (OCP) was monitored for 1h to confirm to its stability. After getting the stable OCP, the upper and lower potential limits of linear sweep voltammetry were set at +200 and -200 mV respectively with reference to OCP. The sweep rate was 1 mV s^{-1}. The corrosion potential E_{corr} and corrosion current I_{corr} was determined by the Tafel extrapolation method. The protective efficiency $P_i(\%)$ of the GO paint coating is obtained from the polarization curves calculated by the equation [14]:

$$P_i(\%) = [1-(I_{corr}/I'_{corr})] \times 100 \ldots\ldots\ldots\ldots\ldots\ldots\ldots\ldots\ldots [6]$$

where I_{corr} and I'_{corr} indicates the corrosion current density of GO coated GI substrate and the bare GI substrate respectively.

2.16.8 Bacterial strains used

The microorganisms *Escherichia coli* (MTCC739), *Staphylococcus aureus* (MTCC96), *Pseudomonas aeruginosa* (MTCC1688) were collected from microbial type culture collection and gene bank, IMTECH, Chandigarh, India and maintained in nutrient medium (Sigma Aldrich, India).

2.16.8.1 Measurement of MIC of GO nanosheets

The antibacterial activity of the GO nanosheets was determined by the micro-dilution method [9]. Inoculates were prepared by suspending growth from overnight cultures in sterile nutrient medium. The 2-fold dilution of samples and standard in the 96-well plates were prepared. Approximately, 10^7 CFU/mL cells were inoculated; the final volume in each microwell plate was 0.2 mL and was incubated at 37 °C for 24 h. The microwell plates were read at 590 nm using the ELISA reader before and after incubation to determine their MIC values. The MIC is defined as the lowest concentration of an antimicrobial agent that allows no growth of a microorganism after overnight incubation when compared with that of the control. The MIC of an antimicrobial drug corresponds to a lowered bacterial density from 10^7 to at least 10^2 CFU/mL (i.e, a 99.9% [3–$\log_{10}$] reduction in bacterial inoculum). The experiments were performed in triplicate and were repeated twice.

2.16.8.1 Bacterial growth inhibition studies of GO paint coated surfaces

The antibacterial property of the GO paint coated surface was evaluated by the method described elsewhere [15]. Breifly, 100 µL suspension of *E. coli* or *S. aureus* or *P. aeruginosa* in 0.1M PBS (approximately 10^8 cells per mL) was added to 20 mL of the nutrient broth in a 50 mL sterile conical flask and incubated overnight in a shaker incubator at 200 rpm and 37 °C. The bacterial cells were collected by

centrifugation at 3000 rpm for 10 min, washed twice with PBS, and diluted in PBS to 5×10^6 cells per mL. The bacterial cells suspension was sprayed on the bare and GO paint coated substrates and dried for 5 minutes in air. The resultant substrates were placed in a Petri dish and immediately covered with a layer of nutrient agar. The Petri dish was sealed and incubated overnight at 37 °C, and the bacterial colonies grown on the slide surface were monitored.

2.16.8.1 In-situ antifouling experiment in sea water

We examined the anti-fouling property of the GO nanopaint for their potential applications towards marine painting. The bare and GO paint coated GI substrates were fixed and immersed into the sea water (lagoon with tidal water directly connected to the Jeju Sea) and the photographic images were recorded before and after 1 week period of immersion.

REFERENCES:

[1] M. Hirata, T. Gotou, S. Horiuchi, M. Fujiwara, and M. Ohba, Carbon **42**, 2929 (2004).

[2] R. D. Holtz, B. A. Lima, A. G. S. Filho, M. Brocchi, and O. L. Alves, Nanomedicine: Nanotechnol. Biol. Med. **8,** 935 (2012).

[3] S. K. Rastogi, V. J. Rutledge, C. Gibson, D. A. Newcombe, J. R. Branen, and A. L. Branen, Nanomedicine: Nanotechnol. Biol. Med. **6,** 305 (2011).

[4] T. Yuranova, R. Mosteo, J. Bandara, D. Laub, and J. Kiwi, Journal of Molecular Catalysis A: Chemical **244,** 160 (2006).

[5] K. Vaideki, S. Jayakumar, G. Thilagavathi, and R. Rajendran, Appl. Surf. Sci. 253, 7323 (2007).

[6] M. Premanathan, K. Karthikeyan, K. Jeyasubramanian, and G. Manivannan, Nanomedicine: Nanotechnol. Biol. Med. **7**, 184 (2011).

[7] G. Venugopal, K. Krishnamoorthy, R. Mohan, and S.-J. Kim, Mater. Chem. Phys. **132,** 29 (2012).

[8] B. Subramanian, R. Ananthakumar, and M. Jayachandran, Surf. Coat. Tech. **205,** 3485 (2011).

[9] Amsterdam, D. In *Susceptibility testing of antimicrobials in liquid media*, 4th ed.; Lorian, V., Ed.; Lippincott Williams & Wilkins: Baltimore MD, **1996**; p 52-111.

[10] M. E. Levison, Infect. Dis. Clin. North Am. **18,** 451 (2004).

[11] K. Krishnamoorthy, S. Natarajan, S. J. Kim, and J. Kadarkaraithangam, Mater. Express **1,** 329 (2011).

[12] G. Gsward (Ed.), Paint Testing Manual. (ASTM Philadelphia, 1972).

[13] J. Tang, Y. Shao, T. Zhang, G. Meng, and F. Wang, Corros. Sci. **53,** 1715 (2011).

[14] C. –H. Chang, T.-C. Huang, C.-W. Peng, T.-C. Yeh, H. I. Lu, W.-I. Hung, C. J. Weng, T. I. Yang, J.-M. Yeh, Carbon **50,** 5044, (2012).

[15] A. Kumar, P. K. Vemula, P. M. Ajayan, and G. John, Nature Mater. 7, 236 (2008).

Chapter 3

Results and discussion

This chapter provides detailed information on the physico-chemical characterization of GO nanosheets synthesis by Hummers method, GO nanosheets with various degrees of oxidation and reduction of graphene oxide by various methods viz (i) sonochemical, (ii) hydrothermal, (iii) using D-galactose and (iv) plasma assisted reduction reaction.

3.1 Graphene oxide nanosheets – physicochemical characterization

3.1.1 UV-vis spectra and X-ray diffraction of GO nanosheets

This study employed the harsh oxidation of graphite powder to synthesize the graphene oxide nanosheets using the modified Hummers method. Finally, a brownish colloidal suspension of GO was obtained as shown in Figure 3.1a. The UV-vis spectroscopy of GO nanosheets is shown in Figure 3.1b. It shows a maximum absorption peak at 227 nm and is attributed to the π-π^* of the aromatic C-C bonds [1]. The XRD pattern of graphite (precursor) and the GO nanosheets is shown in Figure 3.2. The XRD pattern of graphite shows a diffraction peak at $2\theta = 26.3^{\circ}$ corresponding to an interlayer spacing of about 0.34 nm [2].

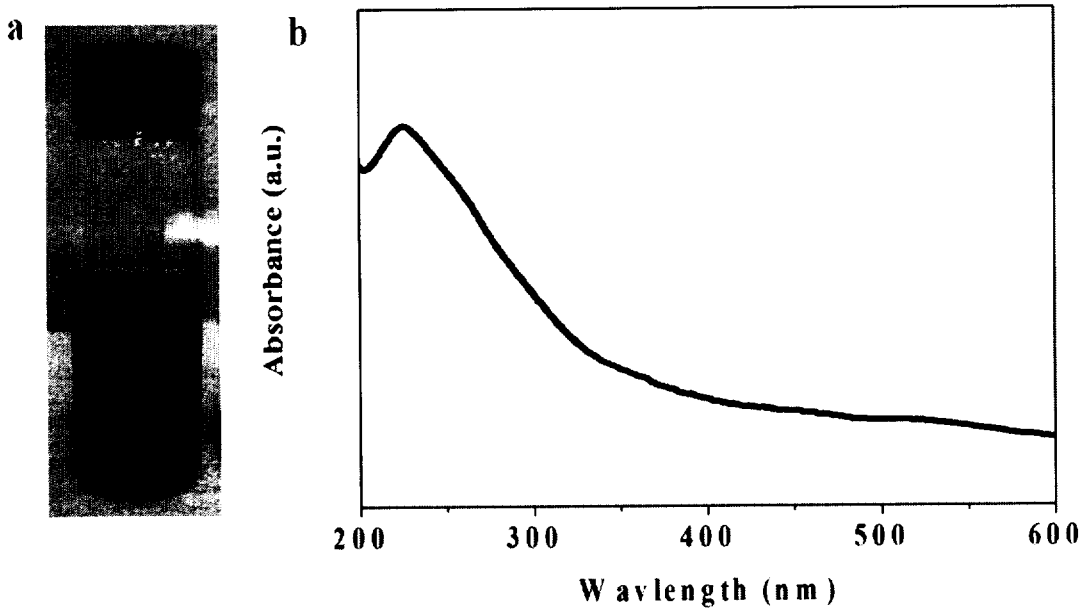

Figure 3.1 a) Digital image of GO dispersion in water. b) UV-vis spectrum of GO nanosheet.

The XRD pattern of GO nanosheets shows a diffraction peak at $2\theta = 10.2^{\circ}$ is attributed to the GO and the corresponding interlayer spacing of 0.88 nm. The complete disappearance of the graphitic peak at $2\theta = 26.3^{\circ}$ and the formation of new broad peak at the lower diffraction area ensure the graphite is completely oxidized [3]. No characteristic peaks of impurities were detected, suggesting that high quality of graphene oxide was obtained.

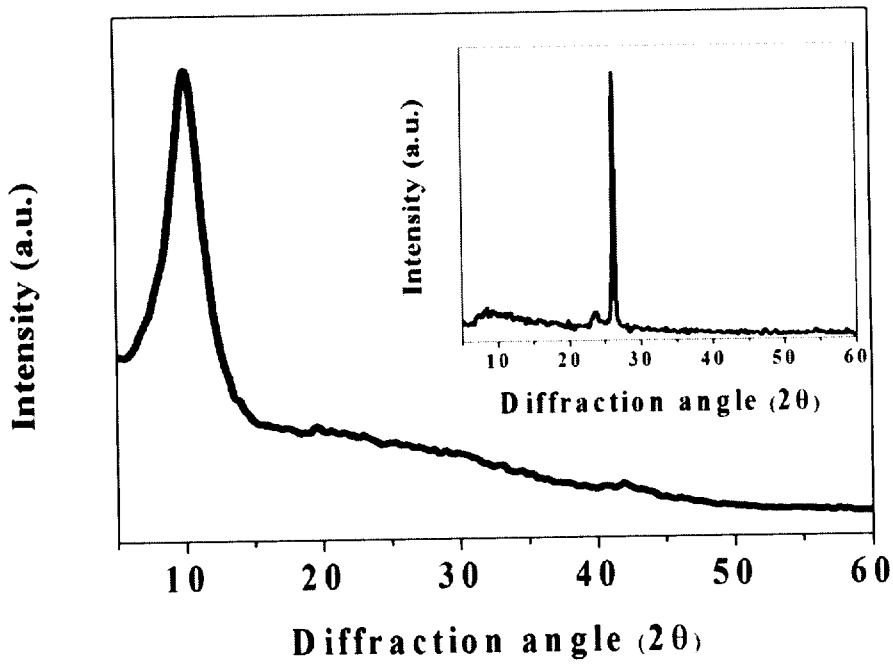

Figure 3.2 X-ray diffraction pattern of GO nanosheets. The inset shows the XRD pattern of graphite.

3.1.2 Surface morphology of GO nanosheets

The surface morphology of the GO nanosheets is studied by the high resolution transmission electron microscope (HR-TEM) analysis. Figure 3.3 shows the HR-TEM image of GO representing the sheet like morphology of the synthesized GO with high transparency. The presence of wrinkles and folded regions is observed

at the edges of the sheet. The corresponding SAED pattern shows clear diffraction spots with six fold symmetry which is in consistent with a hexagonal lattice [4].

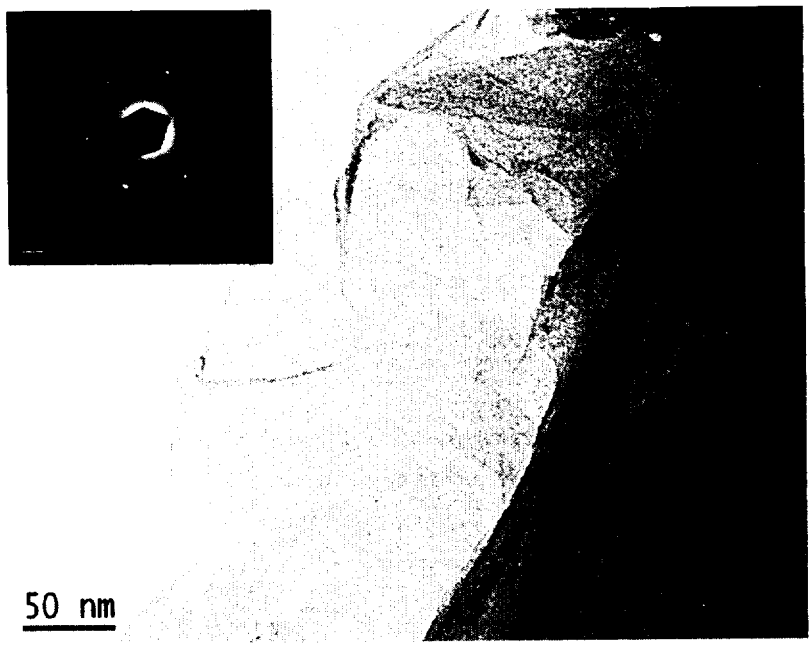

Figure 3.3 High resolution transmission electron microscopic (HR-TEM) image of GO nanosheets. The inset shows the corresponding SAED pattern.

3.1.3 Fourier Transform Infra Red Spectra of GO nanosheets

The oxidation of graphite results in the formation of different types of oxygenated functional groups in GO. We employed the FT-IR analysis in order to study the oxidation of graphite and the type of oxygenated groups attached to the graphite lattice after oxidation reaction. The FT-IR spectrum of GO nanosheets is shown in Figure 3.4. It shows the presence of C=O in carboxylic acid ($\nu_{C=O}$ at 1728 cm^{-1}), C-OH (ν_{C-OH} at 1413 cm^{-1}), C-O (ν_{C-O} at 1050 cm^{-1}) and C-O-C (ν_{C-O-C} at 1250 cm^{-1}) [3]. The peak at 1600 cm^{-1} arises due to the C-C vibrations from the graphitic

domains [5]. The relatively broad peak at 3200 cm^{-1} is due to the adsorbed water content in the surface of graphene oxide [6].

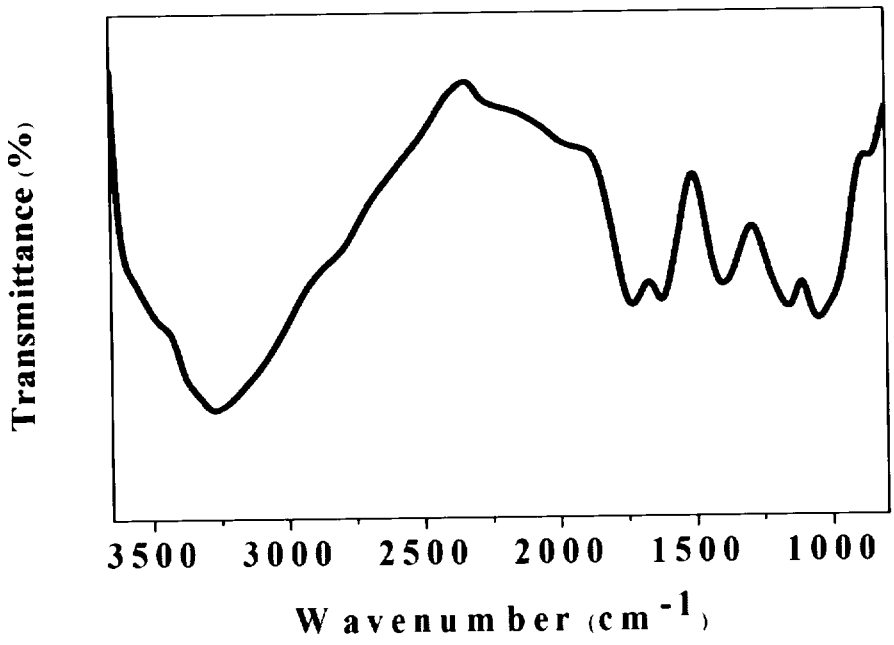

Figure 3.4 Fourier transform infra red spectrum of GO nanosheets.

3.1.4 X-ray photoelectron spectra of GO nanosheets

Further, we studied the XPS analysis of GO nanosheets in order to further study the formation of oxygenated functional groups in GO. Figure 3.5 represents the XPS survey spectrum of GO nanosheets showing the presence of carbon and oxygen at binding energies 284.5 eV and 530 eV, respectively [7]. This confirms the formation of oxygen containing groups on the carbon skeleton of the graphene oxide. The measured O/C intensity ratio of the graphene oxide is 2.1 which are in close agreement with the previous reports on GO. The de-convoluted C 1s spectrum of precursor graphite shows only the presence of C-C skeleton around 284.5 eV (Figure 3.6a). The deconvoluted

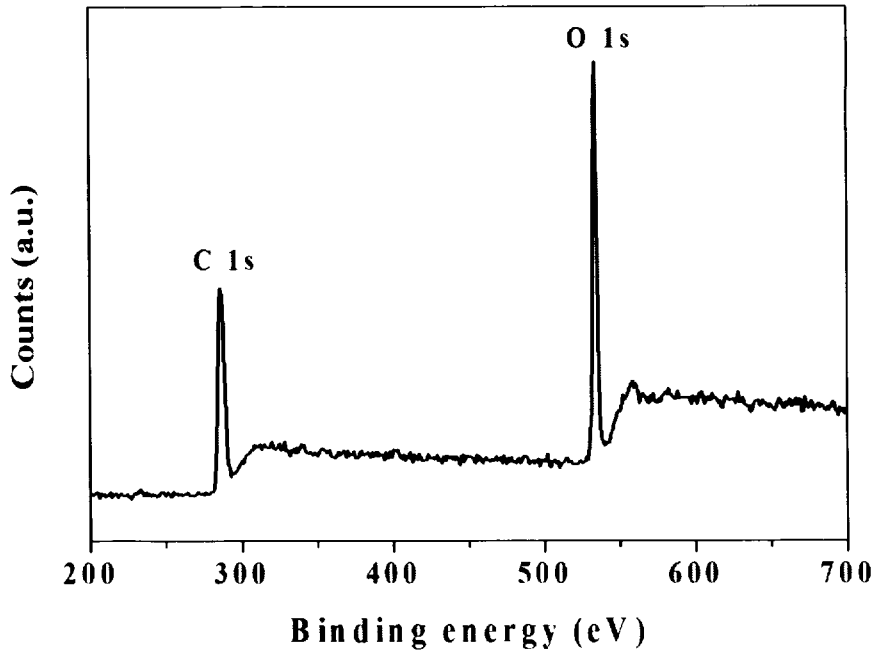

Figure 3.5 X-ray photoelectron spectrum (survey) of GO nanosheets.

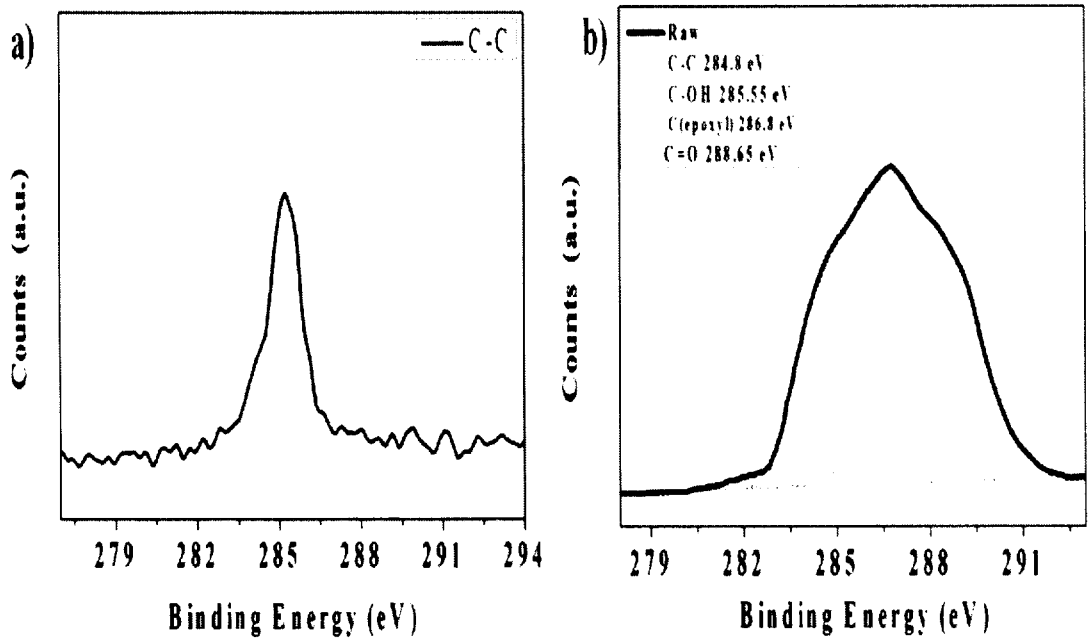

Figure 3.6 C 1s deconvolution spectrum of a) graphite and b) GO nanosheets.

spectrum of GO nanosheets is provided in Figure 3.6b. It shows the presence of four different peaks centered at 284.8 eV, 285.55 eV, 286.8 eV and 288.65 eV were observed corresponding to the C-C in the aromatic rings, hydroxyl, epoxyl and carbonyl groups, respectively [8]. These results indicate that the synthesized GO nanosheets are highly oxygenated.

3.1.5 Raman spectra of GO nanosheets

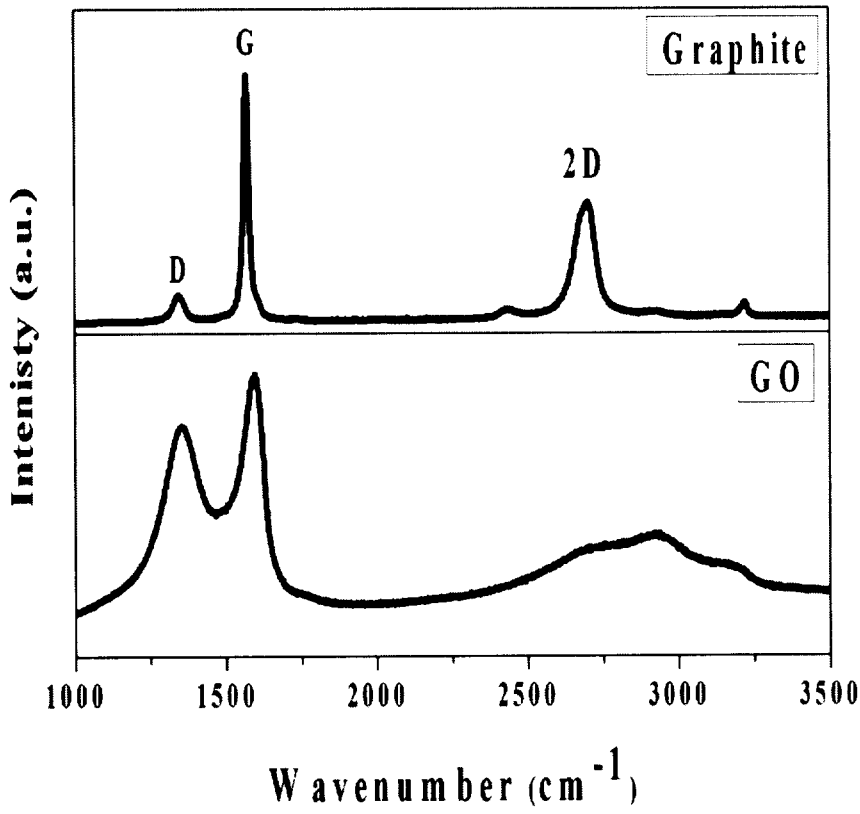

Figure 3.7 Raman spectra of graphite and GO nanosheets.

Raman spectroscopy is the important technique used to characterize the structural and electronic properties of GO nanosheets including the disorders, defects and doping levels. The Raman spectra of graphite and GO nanosheets are shown in

Figure 3.7. The Raman spectrum of the graphite shows a prominent G band as the only feature at 1570 cm^{-1}, corresponding to the first-order scattering of the E2g mode [9]. It also shows a small band at 1354 cm^{-1} named as D band is an evidence for the presence of defects in the graphite material such as bond-angle disorder, bond-length disorder, vacancies, edge defects, etc. [10]. The other important features in the Raman spectra of graphite is the presence of *2D* band at 2700 cm^{-1} (also called as *G'* band) is the overtone of the *D* band [11]. In the Raman spectra of GO, the G band is broadened and shifted to 1596 cm^{-1} due to the oxygenation of the graphite planes which confirms the formation of new sp^3 carbon atoms [12]. In addition to this, the D band at 1350 cm^{-1} is also broadened and increase in intensity which is due to the reduction in size of in-plane sp^2 domains of graphite induced by the creation of defects, vacancies and distortions of the sp^2 domains after complete oxidation [13]. The 2D band becomes broadened in GO with respect to the graphite which is due to the disruption of the stacking order of graphite after oxidation [14]. All changes occurred in the GO are mainly due to the harsh oxidation process subjected to the graphite crystal lattice involved in the synthesis of GO.

3.1.5 Photoluminescence of GO nanosheets

The oxidation of graphite during the preparation of graphene oxide results in the formation of graphitic islands in the graphene oxide [15]. This is in agreement with the density functional studies of have shown the formation of graphitic nanoislands in graphene oxide [16]. This graphitic islands in GO is expected to produce quantum confinement effects in graphene oxide. This results in the origin of band gap in electronic structure of graphene oxide. Hence, we studied the photoluminescence (PL) spectrum of GO using an excitation wavelength of 325

nm and is shown in Figure 3.8. The PL spectrum shows a sharp emission peak in the near UV region at 365 nm due to the near band emission of GO [17]. The unusual strong emission peak in the visible range at 650 nm is not associated with GO but due to the overlap of second order emissions associated to the excitation wavelength [17].

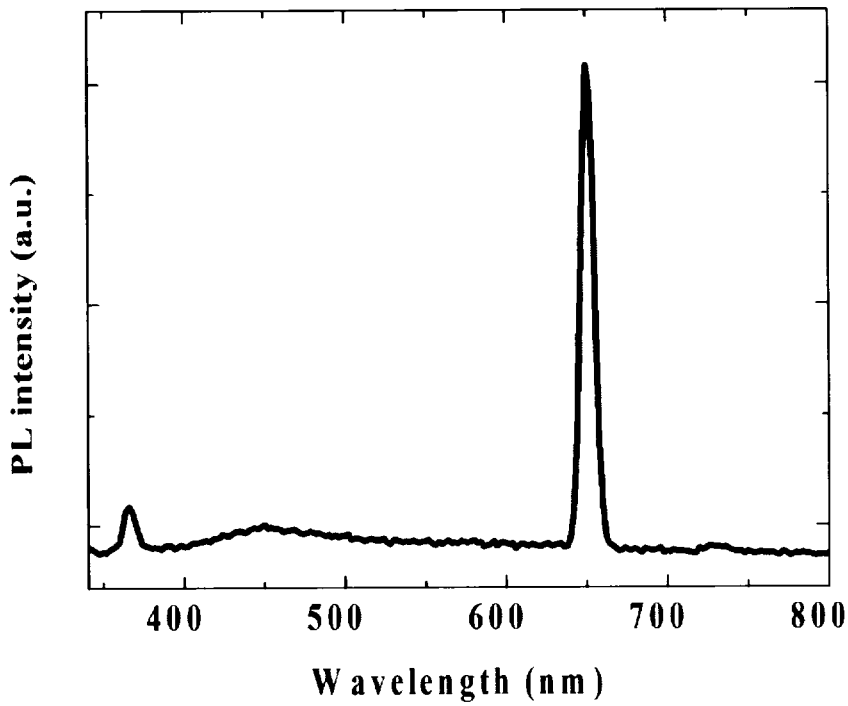

Figure 3.8 Photoluminescence spectrum of GO nanosheets.

These results ensure that a GO nanosheet synthesized using Hummers method possesses are different types of oxygenated functional groups in the graphite lattice due to oxidation and also make structural changes in GO after oxidation. The formation of sp^2 island in sp^3 matrix in GO results in opening of band gap in GO.

3.2 Tunable properties of graphene oxide with different degrees of oxidation

In this study, we used a modified Hummers method to synthesize GO with different degrees of oxidation by adjusting the quantity of oxidizing agent ($KMnO_4$) used in the synthesis reaction. In total, 6 different oxidation levels were synthesized; these were denoted as S-1, S-2, S-3, S-4, S-5 and S-6 where the numbers of the samples indicate the amount (in grams) of $KMnO_4$ used in the oxidation reaction. The photographic images of all samples are presented in Figure 3.9. We can a change in color from black into blackish brown and finally a brownish yellow color as we move through the samples with different levels of oxygenated functional groups.

Figure 3.9 Photographic images of GO samples with different degrees of oxidation.

3.2.1 XRD analysis

XRD analysis was used to characterize the crystalline nature and phase purity of the as-synthesized GO with different degrees of oxidation. The XRD pattern of the graphite (See chapter 1)) shows a diffraction peak at $2\theta = 26.3^{\circ}$ corresponding to an interlayer spacing of about 0.34 nm [2]. The XRD patterns of all samples are shown in Figure 3.10, these clearly show that with increasing oxidation levels, the intensity

of the peak at $2\theta = 26.3^{\circ}$ starts decreases, and finally, disappears at the higher oxidation levels. Simultaneously, we can also observe the appearance of a new peak at a lower diffraction angle starts to grow with increasing oxidation levels corresponding to the diffraction pattern of GO. The XRD pattern of the synthesized samples shows significant changes in the crystallinity of GO at each stage of oxidation. At upon lower oxidation level of graphite using 1 g of $KMnO_4$, we can see a result in peak broadening around $2\theta = 26.15^{\circ}$

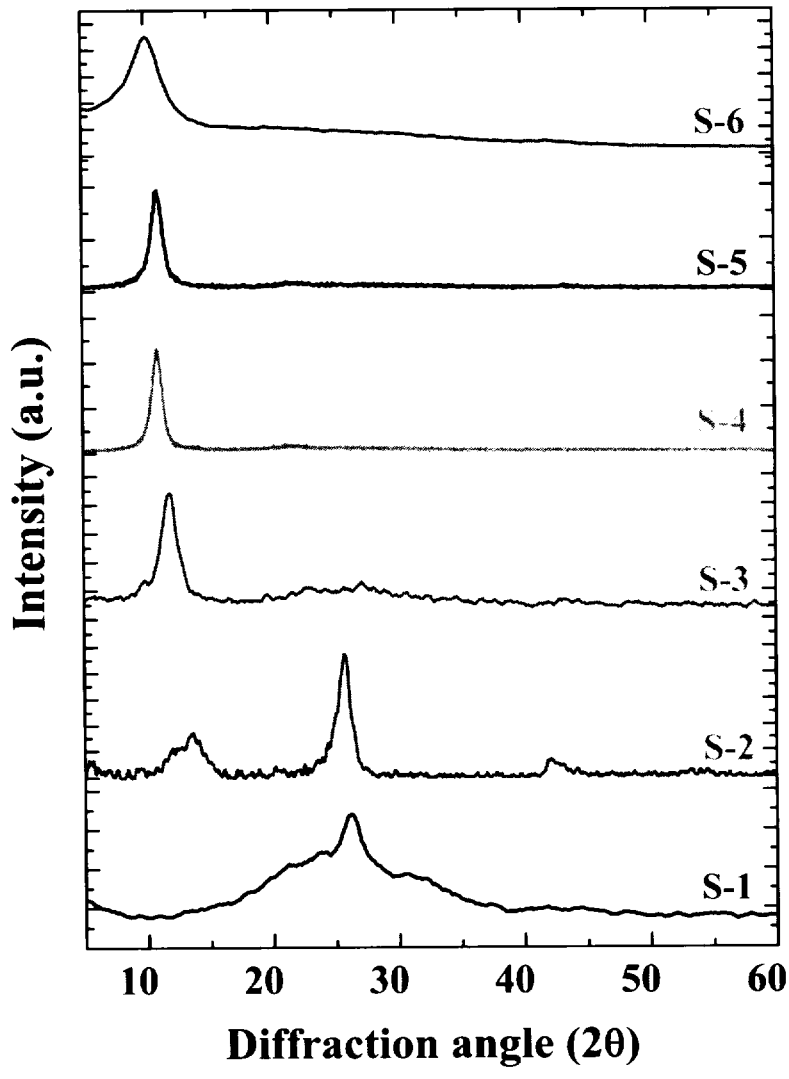

Figure 3.10 X-ray diffraction patterns of GO with different degrees of oxidation.

in the XRD pattern of S-1. The peak broadening effect is due to the lattice distortion that occurs in the *AB* stacking order of the graphite lattice due to mild oxidation. The peak broadening effect due to mild oxidation of graphite is in good agreement with the experimental results of Jeong et al. [18,19] The increase in oxidation quantity (2 g of $KMnO_4$) results in the following changes as shown in the XRD of sample S-2, viz (i) the graphitic peak at $2\theta = 26.15^{\circ}$ becomes narrower and (ii) the formation of a new broad peak at $2\theta = 13.3^{\circ}$ with a lower intensity compared to the graphitic peak. These changes come from the heterogeneous nature of the oxidized graphite comprised of both sp^2 domains from graphite and the sp^3 domains from oxidized graphite. Upto this point, the sample possesses more graphitic domains and less oxidized domains.

When the concentration of $KMnO_4$ was increased to 3 g, the XRD pattern of S-3 shows that the intensity of the peak at $2\theta = 11.74^{\circ}$ becomes higher and the peaks due to graphite disappear. The observed interlayer spacing of S-3 was 0.74 which corresponds to the GO. With further increases in the oxidation content, the XRD pattern of samples S-4, S-5, and S-6 contain only the diffraction peaks due to the GO at $2\theta = 10.91^{\circ}$, 10.52° and 10.12° with an interlayer spacing about 0.81, 0.84, and 0.89 nm, respectively. All together, the XRD analysis revealed that the samples S-1 and S-2 contain more graphitic domains are graphite oxide and the samples S-3, S-4, S-5 and S-6 possess interlayer spacings between 0.74 to 0.89 nm corresponding to the GO. The XRD results of the GO samples are in good agreement with published reports available in the literatures [3,1 9,20,21]. The increasing interlayer spacing of the GO samples suggests that different levels of oxygen containing groups were attached to the graphite lattice. There were no significant changes occurred in the XRD pattern of GO samples other than the increase in interlayer spacing. This finding is supported by the observations of Lucas et al [22].

3.2.2 Morphological characterization and crystallinity analysis

The surface morphology and crystalline nature of the synthesized GO with different degrees of oxidation was analyzed using HR-TEM and selected area electron diffraction (SAED) pattern as shown in Figure 3.11. It is obvious that all the samples possess a sheet like morphology with different transparencies. This is probably due to the number of layers present in the stacked structure of GO. The HR-TEM results of samples

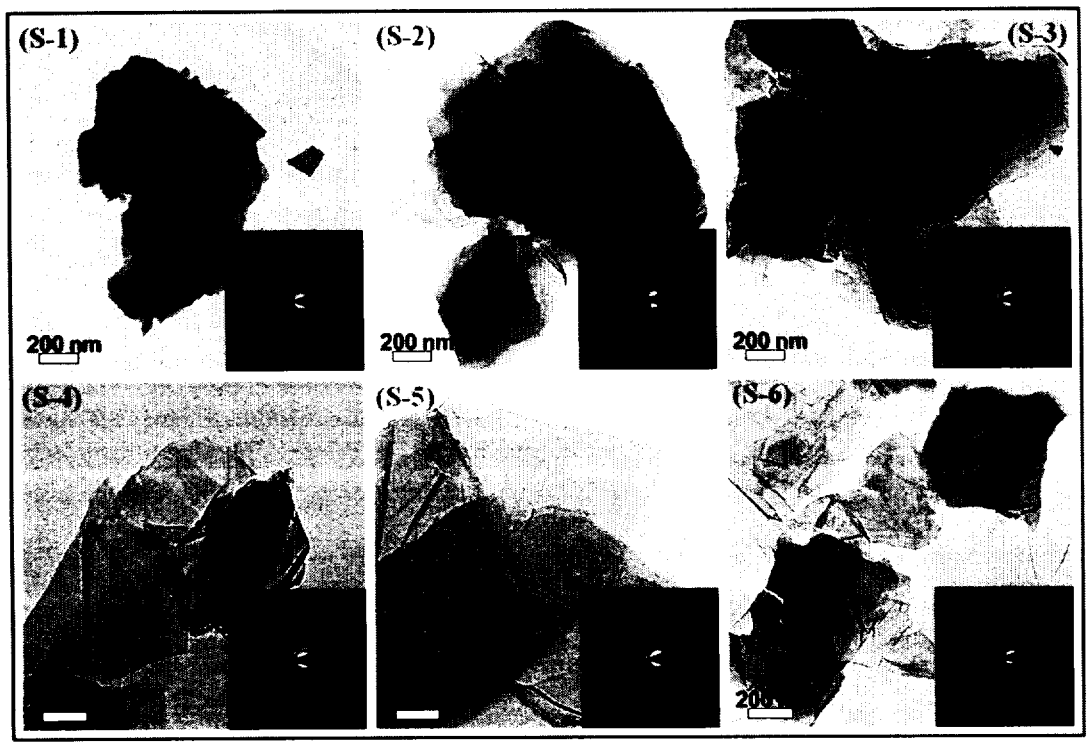

Figure 3.11 High resolution transmission electron microscope images of GO with different degrees of oxidation. The inset in each image shows the SAED pattern of the corresponding sample.

S-1 and S-2 show the sheet like morphology comprised of many layers of partially oxidized graphite oxide. The samples S-1 and S-2 contains less oxygenated functional groups which limits them in terms of exfoliation into monolayers or few layers after

the exfoliation process. Also the transparency of these samples is less than the others due to the presence of more layers. However, with increases in the oxidation level, GO samples (S-3, S-4, S-5 and S-6) become highly transparent, since these samples possess high amounts of oxygenated functional groups, which makes suitable for exfoliation into monolayers or just a few layers of GO after ultrasonication. The dimension of the samples is high in the less oxidized samples (S-1 and S-2) and a reduction in sheet length is observed with increasing oxidation level. An overall analysis of the HR-TEM observations shows that the sheets morphology, dimension and the transparency are highly dependent on the level of oxidation and the exfoliation strategy.

The SAED pattern is one of the tools used to characterize the crystalline nature of nanosized materials. The SAED pattern of all the GO samples with different oxidation level is shown in the inset of their corresponding TEM images, as can be seen in Figure 3.11. It is observed that the SAED pattern of all the samples possess clear diffraction spots with a six-fold pattern that is consistent with the hexagonal lattice [4]. These observations indicate that the graphitic AB stacking order is preserved in the lattice even after higher oxidation levels. This is in accordance with the previous studies of Jeong at al [19], which contains evidence of AB stacking order in graphitic oxide produced using Brodie's method. The SAED pattern of the S-1 and S-2 samples shows a typical ring like pattern indicating the polycrystalline nature of the samples. These rings like pattern arise from the merging of the diffraction spots due to the greater number of layers in the samples [23]. This is in accordance with the XRD patterns of the corresponding samples. However an increase in oxidation levels leads to exfoliation into a single or few layered GO resulting in a diffraction pattern due to the superposition of two or three hexagonal pattern of few layered GO. The

SAED pattern of the S-6 sample is in accordance with previous studies on the SAED pattern of GO as shown by Wilson et al [23]. This observed pattern for our sample (S-6) also closely matches graphite oxide samples studied by other groups [24,25]. Similar phenomenon was also observed by Wilson et al. and their work concluded that GO is not only comprised of fully amorphous regions but some crystalline regions are also present [23]. The amorphous region in GO occurred due to the presence of several sp^3 carbon atoms formed during the oxidation reaction. There are a few reports showing the presence of graphitic islands or unoxidized domains (sp^2 content) within the oxidized domains (sp^3 content) in GO [26,27]. Our previous study also showed that the presence of graphitic islands in GO results in quantum fluctuations leading to an opening of the band gap in the electronic structure of GO [28]. No diffraction pattern was observed for the oxygenated functional groups in all the samples, rather the hexagonal spots of graphitic nature indicate that the oxygenated functional groups formed on the graphite lattice are not resulted in the formation of any superlattice type ordered arrays [23].

We have also studied the morphology of the GO sample (S-6) using atomic force microscopy. The AFM topography of the GO sample S-6 is shown in Figure 3.12. It shows a typical sheet like morphology and also resembles the presence of monolayers (Figure 3.12 (d)) and few layered GO (Figure 3.12(e)). The difference in the number of layers can be easily distinguished using the contrast of the sheets. The monolayers of GO have a light in color whereas the few layered GO are bright in color Figure 3.12 (a). The presence of a few layers in the sample is due to the aggregation or self assembly of two or three layers of GO during the drying process in the specimen preparation. We also examined the nature of monolayer GO, as seen in

Figure 3.12 (b) which shows high transparency and some folded regions. Similarly, Figure 3.12 (c) shows the presence of monolayer and few layered GO depicting the presence of wrinkles in the sheets. The AFM studies are in agreement with the HR-TEM observations mentioned above.

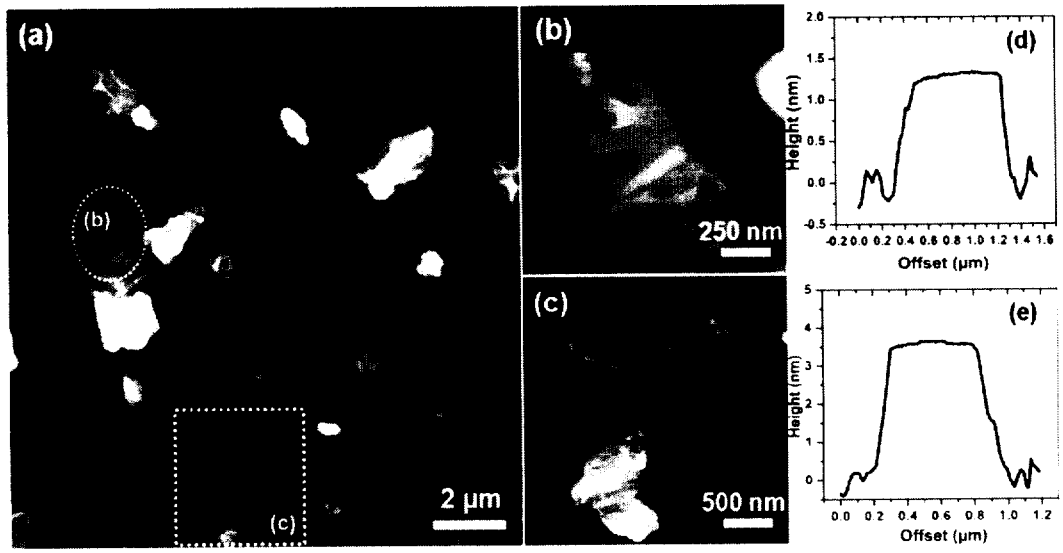

Figure 3.12 (a) Atomic force microscopic image of GO (S-6) nanosheets; (b) enlarged circled area from (a) and; (c) enlarged squared area from (a). The line profile of the GO nanosheets shown in (c) is represented in (d) and (e).

3.2.3 FT-IR characterization

In order to study the different types of functional groups formed in the GO at different degrees of functional groups, FT-IR spectroscopy was used. The FT-IR spectra of all samples are shown in Figure 3. 13. The FT-IR shows band at 1573 cm^{-1} due to the presence of C-C stretching in graphitic domains found in S-1. With further increases in oxidation level, the FT-IR spectrum reveal the presence of C=O (1720 cm^{-1}), C-O (1050 cm^{-1}), C-O-C (1250 cm^{-1}) C-OH (1403 cm^{-1}) in the GO samples [3]. The peak found at 1620 cm^{-1} is a resonance peak that can be assigned to the C-C stretching and absorbed hydroxyl groups in the GO [5]. We also measured the XPS

spectroscopy of all samples in order to study the different types of functional groups formed in GO with respect to the degree of oxidation.

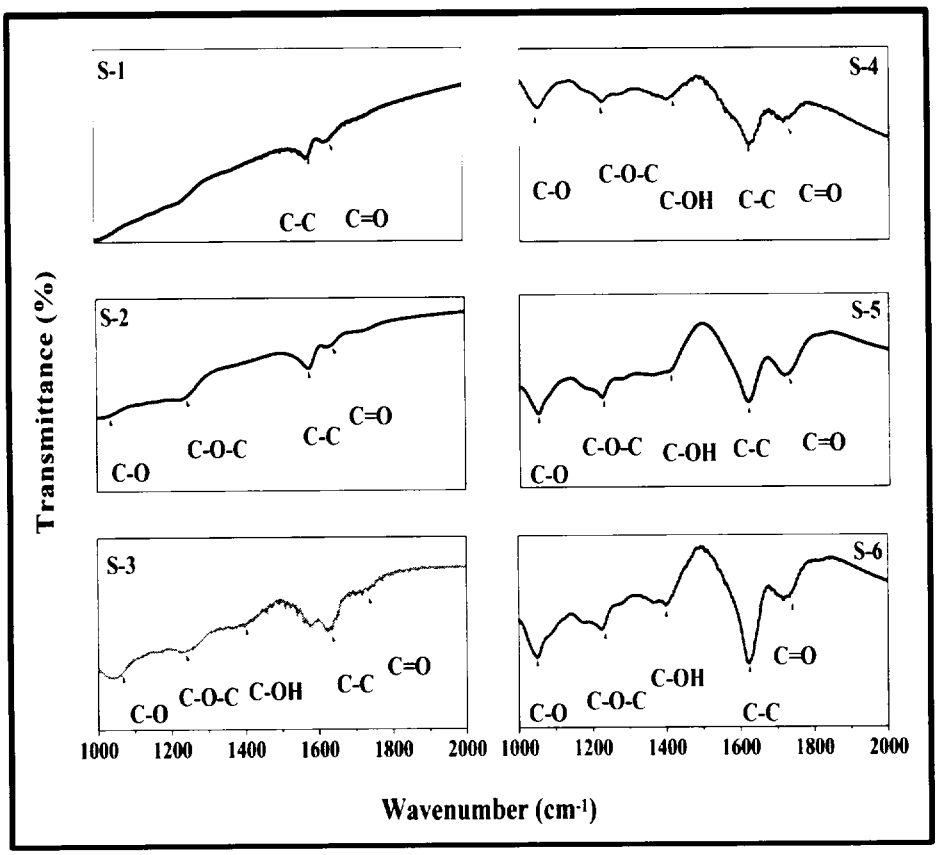

Figure 3.13 Fourier transform infrared spectra of GO with different degrees of oxidation.

3.2.4 XPS analysis

The chemical states of all the samples were investigated by the use of XPS spectra and are shown in Figure 3.14. For comparison, the XPS of the pristine graphite was also measured and is given in section 3.1. In the XPS of graphite, we can see only a peak corresponding to C-C stretching at 284.5 eV indicating the absence of any oxygenated function groups [7]. With increasing the oxidation level, the intensity of the C-C peak due to the sp^2 carbon bond in graphite gradually decreases and an increase in intensity of new

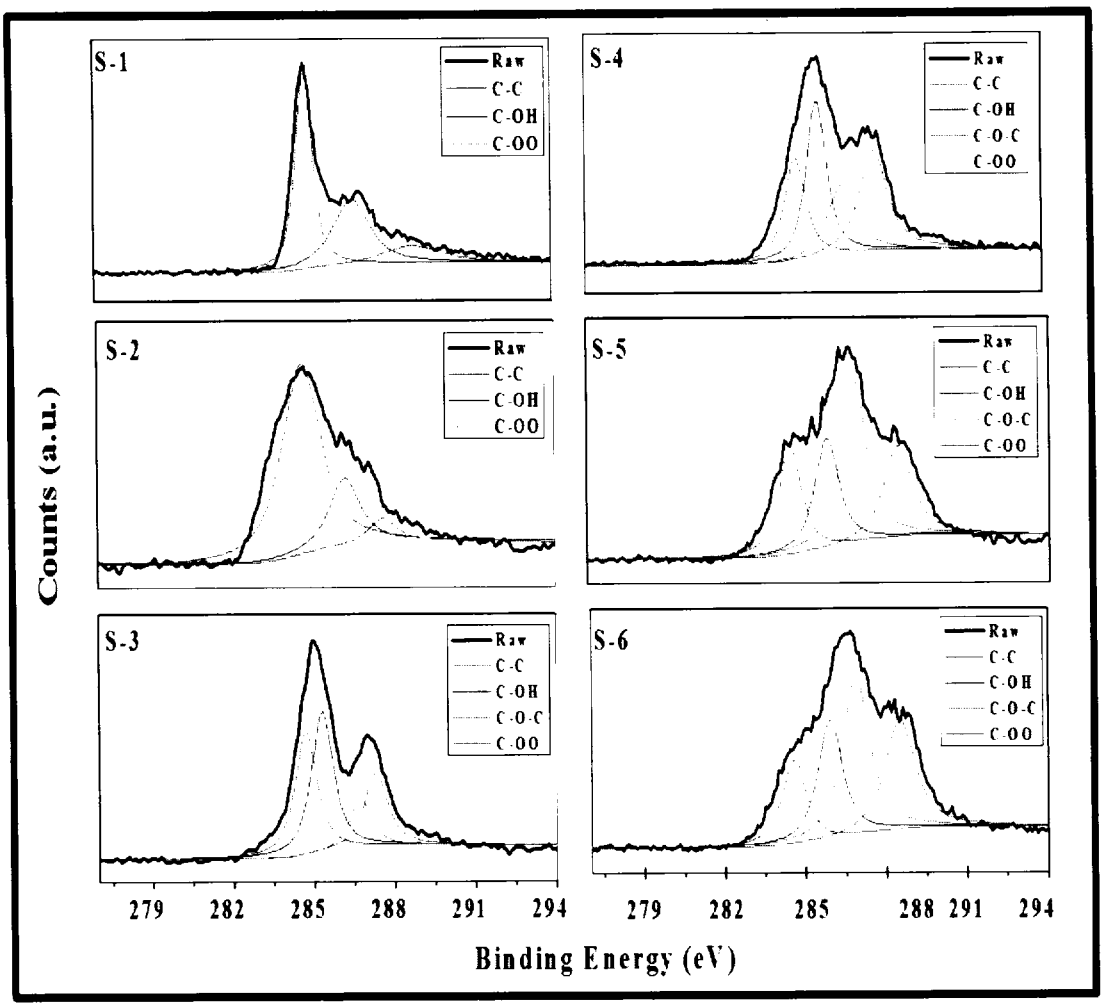

Figure 3.14 X-ray photoelectron spectra of GO with different degrees of oxidation.

functional group's peaks, such as hydroxyl, carboxyl and epoxyl groups, due to oxidation of graphite are clearly evident from the XPS of the GO at various stages of oxidation. The XPS of sample S-1 shows the presence of C-OH groups in addition to the C-C group in the material and also it possesses a small amount of -O-C=O groups. When the oxidation level is increased, S-2 shows increases in intensity of the C-OH and -O-C=O functional groups and the corresponding intensity of C-C is lower than S-1. Further increases in the oxidation result in the formation of epoxide groups along with the hydroxyl and carboxyl groups, which are clearly noticeable in the XPS of S-3.

When the oxidation level is further increased, the XPS of samples S-4, S-5 and S-6 shows that there is an increase in the intensity of epoxide (O-C-O) groups and a decrease in the hydroxyl and carboxyl groups. The sp^2/sp^3 ratio measured from the XPS spectra of samples S-1, S-2, S-3, S-4, S-5, and S-6 are found to be 2.15, 1.52, 0.36, 0.31, 0.27, and 0.25, respectively. The sp^2/sp^3 ratio decreases with increasing oxidation level and is matched well with the previous report in graphite oxide using Staudenmaier process and Brodie method by Lee et al [29]. This clearly demonstrates that the hydroxyl and carboxyl groups, on further oxidation, lead to the formation of the epoxide groups which results in the increased interlayer spacing in S-6, as seen in the XRD results. The formation of epoxide groups from S-3 level signifies the increase in interlayer spacing and exfoliation of graphitic oxide into GO. This is in agreement with the XRD results of our samples in which S-1 and S-2 samples are graphitic oxide whereas the remaining samples are GO with different oxygen groups.

Hence, the overall analysis of the XPS results demonstrates that the hydroxyl and carboxyl groups are formed at lower oxidation levels and are converted into epoxy groups when the oxidation level is increased. The reason for this complicated mechanism is as follows: the Hummers method employs $KMnO_4$ in conc. H_2SO_4 as the oxidizing agent; this can produce dimanganese heptoxide (Mn_2O_7) which is a strong oxidizer [30]. Mn_2O_7 is capable of epoxidation of unsaturated oxygenated groups [31] formed in the graphite during the oxidation reaction and this results in the higher O-C-O groups in the GO samples with a high oxidation level. To the best of our knowledge no other research group has analyzed the different oxidation levels of GO using Hummers method. The results of the XRD and XPS analysis support the previous finding of Lucas et al [22].

3.2.5 Zeta potential analysis

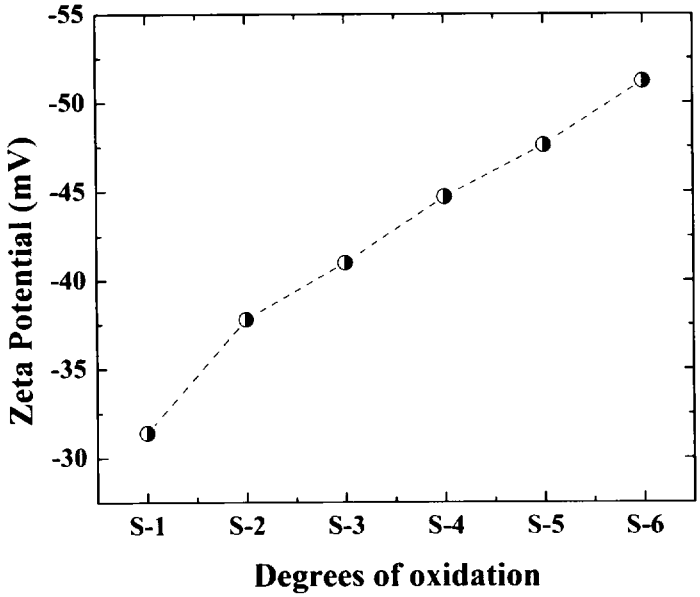

Figure 3.15 Plot of zeta potential vs samples with different oxidation levels.

The influence of oxygenated functional groups in GO with different degrees of oxidation was evaluated by zeta potential analysis. The zeta potential is a physical property exhibited by any material in dispersion and is an important parameter used for characterizing the electrical properties of interfacial layers in dispersion, which is closely related to the pseudocapacitance behavior of electrode materials used in electrochemical double layer supercapacitors [32]. The zeta potential of all the samples was measured in an aqueous medium and is shown in Figure 3.15 as a plot of zeta potential against the different degrees of oxidation. We used the Smoluchowski approximation [33] for the measurement of the zeta potential of GO. The Smoluchowski expression for plate-like particles [34] is given as $\zeta = \eta\mu/\varepsilon_r\varepsilon_o$, *where* ζ is the zeta potential, η is the solution viscosity, μ is the electrophoretic mobility and ε is the permittivity of the solution, $\varepsilon=\varepsilon_r\varepsilon_o$.This expression holds good for the zeta potential measurement of lamella type structures like graphene and GO. This finding

supports the previous study of Lotya et al. on the zeta analysis of graphene nanosheets [35].

The zeta potential measurements show a linear increase in the zeta potential with respect to increasing oxidation level. The zeta potential values of S-1, S-2, S-3, S-4, S-5 and S-6 were found to be -31.4, -37.8, -41, -44.7, -47.6, and -51.2 mV, respectively. The negative zeta potential values are due to the presence of electronegative functional groups formed at the graphite lattice during the oxidation [36]. With the successive increase in the oxidation quantity, a greater number of electronegative functional groups are formed in GO resulting in the increase of the zeta potential at higher oxidation levels. Finally, the results for the GO sample S-6 possessing more oxygenated functional groups with a higher zeta potential in an aqueous medium is more likely due to the dissociation of a greater number of acidic groups ($COOH \rightarrow COO^- + H^+$) at the surface thereby resulting in a higher zeta potential. According to the ASTM standard for stability of colloidal suspensions, a zeta potential between 30-40 mV (either positive or negative) shows moderate stability, higher than 40 mV (either positive or negative) resembles high stability [37]. Hence, the samples S-1 and S-2 with lower oxidation levels (graphitic oxide) exhibit "moderate stability" whereas the samples with higher oxidation levels (S-3, S-4, S-5 and S-6) exhibit "high stability".

3.2.6 Raman analysis

Raman spectroscopy is a standard non-destructive tool for the analysis of structural elucidation of carbon materials, such as graphite, diamond, carbon nanotubes, graphene and GO. Raman spectra were carried out for all the samples with

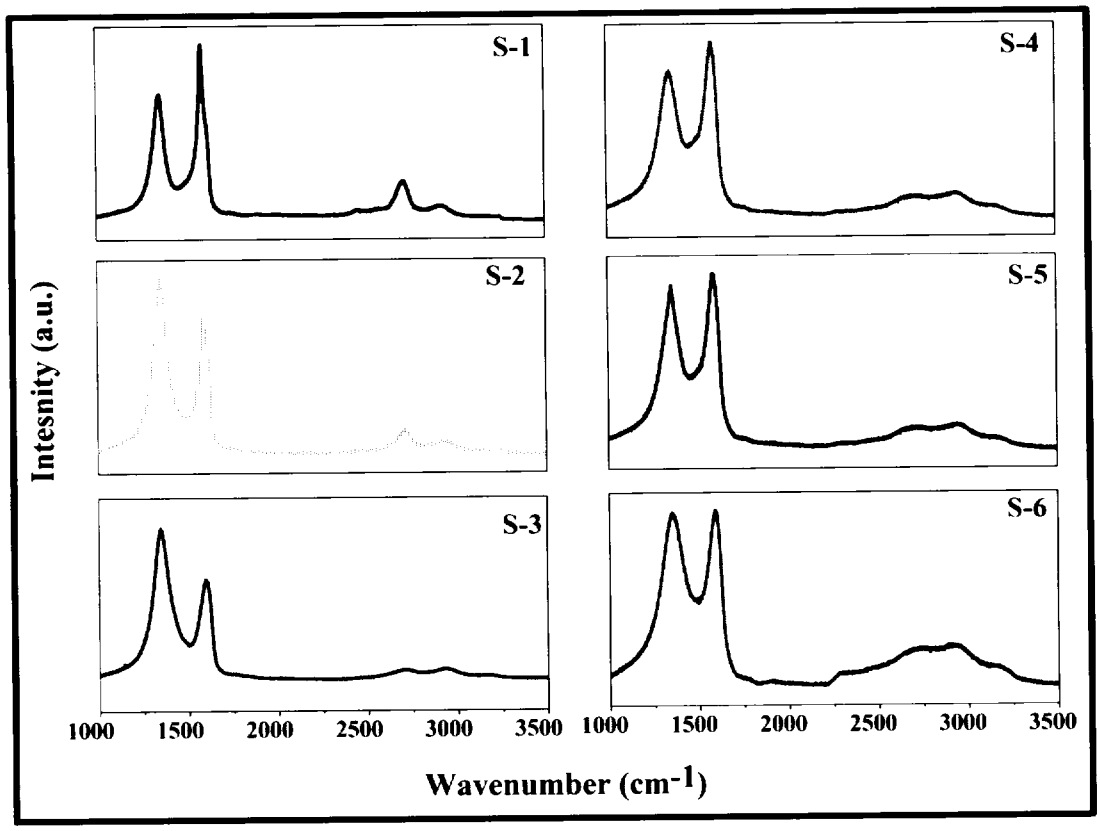

Figure 3.16 Raman spectroscopy of GO with different degrees of oxidation.

different oxygen contents from S-1 to S6 as shown in Figure 3.16. As a reference, the Raman spectrum of precursor graphite was also measured and is shown in the section 3.1. The spectrum of graphite shows a strong *G* band at 1570 cm^{-1} due to first order scattering of the *E2g* mode [9]. It also contains a small band at 1354 cm^{-1} named the *D* band, which is evidence for the presence of defects in the graphite material such as bond-angle disorder, bond-length disorder, vacancies, edge defects, etc.,[10] Another important features in the Raman spectra of graphite is the presence of a *2D* band at 2700 cm^{-1} (also called the *G'* band), this is the overtone of the *D* band [38]. The 2D band is used to evaluate the structural parameters of the *c-axis* orientation, since this band is very sensitive to the stacking order of the graphite along the *c-axis* [39]. It is expected that the harsh chemical oxidation process will result in predominant

structural changes in the graphite lattice due to the formation of different types of oxygenated functional groups at the basal plane and also at the edges. Figure 3.16 shows the Raman spectra of all the samples and shows significant changes at different degrees of oxidation. In S-1, the G band is shifted towards a higher wavenumber (1585 cm^{-1}) due to the oxidation of graphite and the D band has a higher intensity, which can attributed to the formation of defects and disorder such as the presence of *in-plane* hetero-atoms, grain boundaries, aliphatic chain, etc., On the other hand, the intensity of the *2D* band is smaller after oxidation, a new band appeared around 2950 cm^{-1} which is denoted as *D+G* band. The decrease in the *2D* band is due to the breaking of the stacking order due to the oxidation reaction.

Figure 3.17 (a) shows the corresponding changes in the G band with respect to levels of oxidation. It shows that the G band is shifted towards a higher wavenumber with the increase in oxidation level. At the highest oxidation level, the G band position reaches a position at 1596 cm^{-1}. The shift in G band is associated with the formation of new sp^3 carbon atoms in the graphite lattice [40]. In addition to the shift in G band position; the full width half maximum (FWHM) of the G band also increases with respect to the oxidation level. The FWHM of the G band with increasing oxidation level was 45, 54, 70, 103, 114, and 124 cm^{-1}, for the samples S-1, S-2, S-3, S-4, S-5, and S-6, respectively. The shift in G band increase in FWHM suggests that the presence of sp^3 carbons is increased with respect to oxidation level. Similarly, the different degrees of oxidation affect the nature of D band. The intensity of the D band increases with increasing oxidation and becomes constant at higher oxidation levels. The FWHM of the D band linearly increase with the increase in oxidation levels indicating that the oxidation process highly influences the *in-plane* sp^2 domains of the graphite with defects [40]. Figure 3.17(b) shows the variation of

$I_{(D)}/I_{(G)}$ with respect to the oxidation level. It shows that lower oxidation levels result in an increase in the $I_{(D)}/I_{(G)}$ ratio, which decreases with increasing oxidation, and finally becomes saturated at higher oxidation levels. The decrease in $I_{(D)}/I_{(G)}$ ratio at higher levels of oxidation is compensated by the increase in the FWHM of the G band.

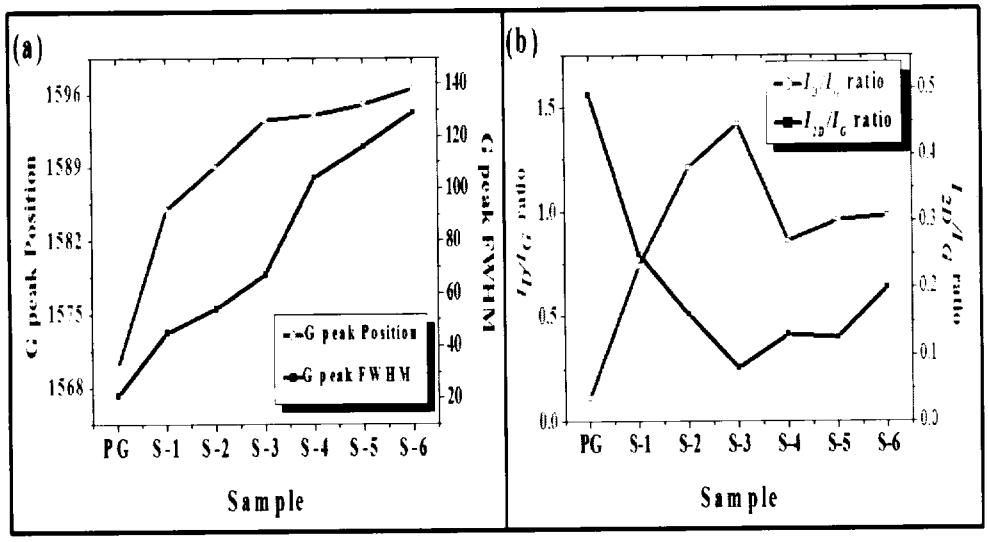

Figure 3.17 (a) Dependence of G band position and FWHM with respect to oxidation level. (b) Variation of $I_{(D)}/I_{(G)}$ ratio and $I_{(2D)}/I_{(G)}$ ratio with respect to oxidation level. PG refers to pristine graphite.

The peaks correspond to overtones, such as the 2D, D+G and 2G bands, which also display significant changes depending on the oxidation. The intensity of the 2D band decreases with increases in oxidation level and broadens at the higher oxidation levels. Figure 3.17 (b) represents the change in $I_{(2D)}/I_{(G)}$ ratio with respect to oxidation level. It decreases up to S-3 and then increases oxidation levels higher than S-3. Since the 2D band is structure sensitive [39], the $I_{(2D)}/I_{(G)}$ ratio clearly illustrates the transition from crystalline to an amorphous phase in GO upon oxidation. Similarly, the other overtone bands D+G (2922 cm^{-1}) and 2G (3171 cm^{-1}) increased with increasing oxidation level. The changes in overtone bands, such as 2D, D+G and 2G

bands, illustrate the disruption of the graphitic *ab* stacking order in GO with increasing oxidation level. The average crystallite size of the sp^2 domains in the GO samples can be calculated by the intensity measures of the D band ($I_{(D)}$) and G band ($I_{(G)}$) [40]. Many equations such as Tuinstra and Koenig's equation [41], the Knight and White relation [42], have been employed to measure the average crystallite size of the sp^2 domains using the $I_{(D)}/I_{(G)}$ ratio. Later on, the general equation of the average crystallite size of the sp^2 domains L_a in the nanographite sytems was given by Cancodo et al. [43] by relating the $I_{(D)}/I_{(G)}$ ratio to the fourth power of the laser energy used in the experiment. This modified equation can be given as

$$L_a\,(\text{nm}) = [(2.4*10^{-10})\,(\lambda_l)^4] \,/\, [I_{(D)}/I_{(G)}] \quad \ldots\ldots\ldots\ldots\ldots\ldots [1]$$

where L_a is the average crystallite size of the sp^2 domains, λ_l is the input laser energy, $I_{(D)}$ is the intensity of the D band, and $I_{(G)}$ is the intensity of the G band. The calculated L_a values are 18.24, 11.25, 9.63, 15.67, 14.06, and 13.77 nm, for samples S-1, S-2, S-3, S-4, S-5 and S-6, respectively. The L_a value of the precursor graphite was calculated to be 122 nm. The results indicate that the average crystallite size decreases with less oxidation; this may be due to the breaking of crystallites with initial oxidation resulting in the formation of defects, disorders, sp^3 hybridization and changes in crystallinity. At the same time, L_a starts increasing for sample S-4 and becomes constant (around 14 nm for S-5 and S-6) at higher levels of oxidation. This is in agreement with the previous investigations on the crystallite size of series of graphite oxide using Staudenmaier method as evaluated by Lucas et al [22]. The recent investigation on the oxidation of mechanically exfoliated graphene by Wang et al. also supports our findings [44]. In these aspects, there is no straightforward relation between the oxidized (sp^3) and unoxidized (sp^2) states with respect to level of oxidation. Overall, the Raman spectroscopy results show the transition of crystalline

graphite into an amorphous state and the disruption of stacking order with respect to increases in the oxidation level. However, there are much further investigations needed to study the detailed physics and chemistry underlying the structure of GO.

3.2.7 Electrochemical properties

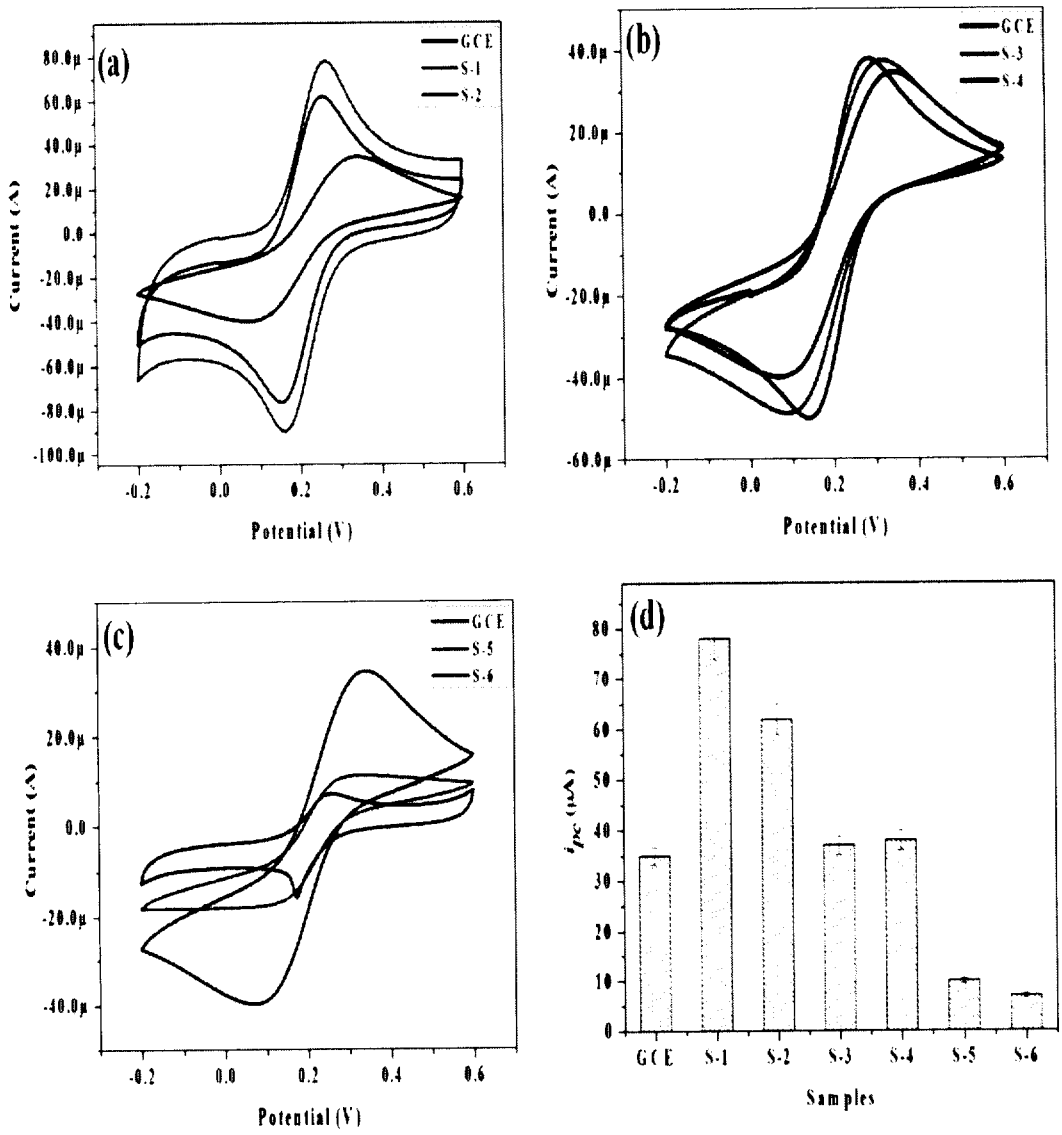

Figure 3.18 (a-c) Cyclic voltammetry of GO samples (S-1 to S-6) modified on GCE electrodes in 5 mM $K_3[Fe(CN)_6]$ containing 0.1 M KCl solution. (d) Comparison of I_{pc} of the samples with different oxidation levels.

The influence of oxygenated functional groups in GO was also studied by using CV measurements using a 5mM solution of potassium ferricyanide [$K_3(FeCN)_6$] containing 0.1 M KCl solution. The oxygenated functional groups present in GO nanosheets play a key role in electrochemical biosensors for glucose sensing, supercapacitors, etc., [45]. Hence a study on the electrochemical properties of GO with different oxidation level is an area of potential interest. Herein, the GO sample is modified onto the surface of a GCE electrode. Figure 3.18 shows the CV curves of all the tested samples in comparison with the GCE electrode. It shows that the typical redox reaction occurred at the electrode surface indicating the presence of an anodic peak and cathodic peak in the CV curves. It is clear from Figure 3.18 (a), that samples S-1 and S-2 show a higher current value for the redox reaction than the GCE electrode. As evident from the XPS and zeta potential measurement stated above, these samples contain less oxygenated functional groups, thereby less surface charge which enables them to attract ferricyanide ions to the electrode surface for the electrochemical reaction. Similarly, the samples S-3 and S-4 show higher electrochemical reactions compared with the GCE (as shown in Figure. 3.18 b) but lower than the samples S-1 and S-2. This is due to the increase in surface oxygen groups and surface charge. Figure 3.18 (c) displays the CV curves of samples S-5 and S-6 and shows a significant reduction in the cathodic peak current (I_{pc}) compared with the GCE and is due to the high surface charge of these samples (as evident from the XPS and zeta potential measurements). Both S-5 and S-6 with higher levels of oxidation act as an insulating layer on the GCE electrode and due to their high surface charge, the ferricyanide ions are repelled at the electrode surface thereby limiting electrochemical reactions. The electrochemical behavior of the S-6 sample is consistent with the previous studies of GuO et al [46]. However, it is still remaining elusive to determine the contribution of

each functional group on the electrochemical properties of GO due to its structural and chemical inhomogeneous nature. The histogram curve of all the samples in comparison with the GCE electrode is shown in Figure 3.18 (d). It shows that the I_{pc} value decreases with increasing levels of oxidation, thereby showing the transition from metallic to semiconducting and insulating behavior due to increases in oxidation level.

In this study, we synthesized GO using a modified Hummers method with different degrees of oxidation. The formation of various oxygenated functional groups at different stages of oxidation and their influence on the chemical and structural analysis was investigated. XPS analyses showed the formation of hydroxyl and carboxyl groups in the graphite lattice during the initial stage of oxidation and these were converted into epoxide groups at higher oxidation levels. The various degrees of oxidation significantly altered the zeta potential properties exhibiting moderate stability at lower oxidation levels and high stability at higher oxidation levels. Moreover, a detailed study on the Raman spectra at various levels of the oxidized samples was presented. It showed that the sp^3 domains are increasing with increase in oxidation level with the disruption of the graphitic stacking order. The influence of oxygenated functional groups in different GO significantly altered the electrochemical properties of GO. The key findings of our work support the view of the tunable properties of GO, that is, by varying the oxidization degree which can provide new positive features in the development of GO-based device applications.

3.3 Ultrasound assisted synthesis of graphene oxide

In this experiment, the GO nanosheets are reduced into graphene nanosheets under alkaline condition with little amount of hydrazine in the presence of ultrasonic irradiation. In recent years, sonochemical method becomes more promising in the synthesis of variety of nanomaterials including nanochalcogenides, metal and metal oxide nanoparticles [47,48]. The mechanism of sonochemistry relies on the acoustic cavitation phenomenon, i.e., the formation, growth, and collapse of bubbles in liquid medium [49]. According to the hot spot theory, extremely high temperature about 5000 K, pressure about 20 MPa and very high cooling rate about 10^{10} Ks^{-1} arises during the acoustic cavitation, thus enabling reaction conditions which further results in unique properties of the synthesized particles [50]. The sonochemical method can be more suitable for the reduction of GO due to the extreme reaction conditions such as high temperature, pressure, rapid cooling times which permits to a range of chemical reaction generally not accessible in the conventional synthesis methods. Herein, we are reporting a facile sonochemical method for the redcution of GO into graphene nanosheets within a short reaction time.

3.3.1 Mechanism of reduction of graphene oxide

In this study, a sonochemical method for the preparation of graphene nanosheets was employed. At first, graphene oxide was synthesized by harsh oxidation of graphite followed by ultrasonic exfoliation according to the Hummer's method. The graphitic oxide is exfoliated into graphene oxide by the aid of ultrasonication as shown in Scheme 1. In general, both graphitic oxide and graphene oxide possess same chemical structure and layered structure as in graphite. The only difference between them is the number of individual layers present in them in which graphitic oxide possesses more number of layers like graphite whereas graphene

oxide possesses monolayers or few numbers of layers of oxidized graphite [51]. The presence of oxygenated functional groups in graphitic oxide makes them hydrophilic which facilitates the exfoliation into monolayers of graphene oxide under sonication.

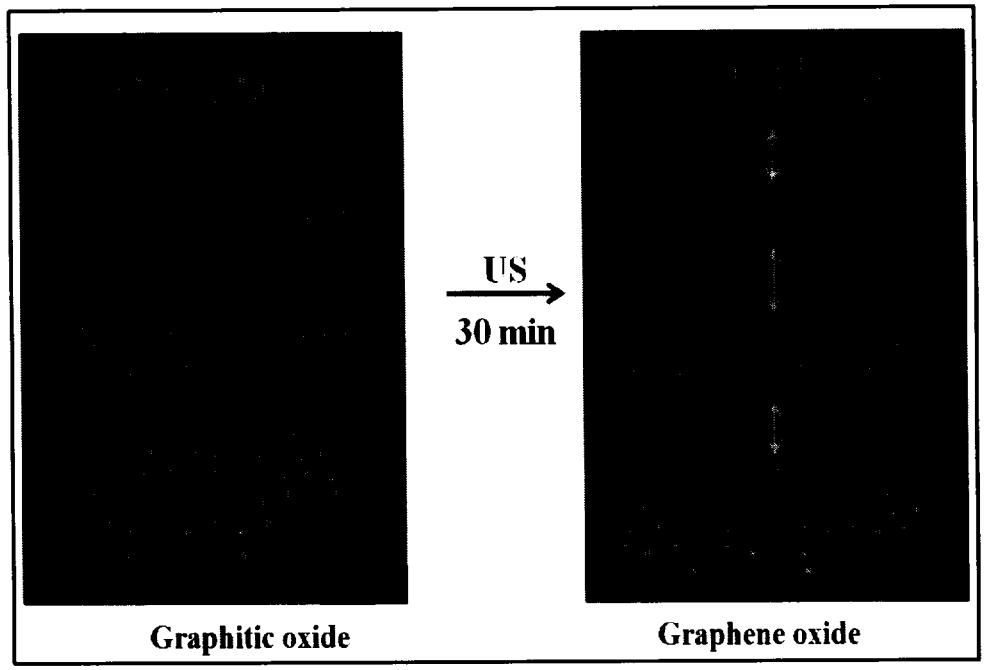

Scheme.1 Exfoliation of graphitic oxide into graphene oxide by sonication for 30 min. Arrow marks in graphene oxide (right) indicates the increase in inter-layer spacing after sonication process. The cyan color indicated the carbon skeleton in graphene sheet and the red color indicated the oxygenated functional groups. US - ultrasonic irradiation.

The reduction of graphene oxide into graphene nanosheets was achieved by sonochemical method. The most important issue in the reduction of the graphene oxide into graphene nanosheets is the occurrence of agglomeration of graphene oxide or its partially reduced state during the reduction reaction which results in the formation aggregated graphene sheets [52-54]. This limits the efficiency of reduction

thereby, removal of oxygenated functional groups in graphene oxide is not fully achieved and often it takes longer reaction time. In this regards, sonochemical synthesis of graphene is more promising for the reduction of graphene oxide since ultrasound irradiation drives some special features that are usually not occurred in the ordinary chemical reactions such as elevated temperature, high pressure and rapid cooling rates etc., [55].

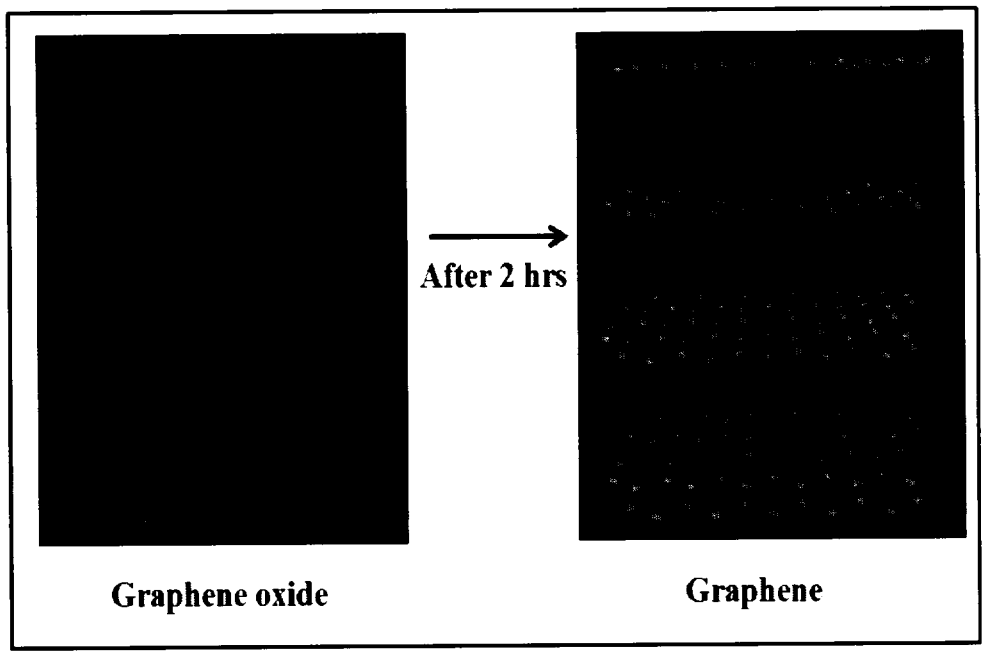

Scheme.2 Sonochemical synthesis of graphene oxide into graphene nanosheets in the presence of hydrazine and NaOH. The advantage of ultrasound in the reduction reaction is that it prevents the agglomeration of the graphene oxide or its partially reduced state during the reduction reaction, thereby enabling more space for the reduction of epoxyl groups in between the two layers of the graphene sheet. US - ultrasonic irradiation.

The mechanism of sonochemical synthesis of graphene is shown in Scheme. 2. In this study, we utilized the reaction at alkaline conditions (NaOH) in presence of

little amount of hydrazine. Under alkaline conditions, the de-oxygenation of functional groups in graphene oxide should occur as demonstrated by Fan *et al* [56]. The use of hydrazine is to reduce the epoxide groups which present at the basal plane of graphene oxide which is in agreement with the theoretical studies by Kim *et al* and experimental studies by Stankovich *et al* [57,58].

As shown in Scheme 2, the use of ultrasound irradiation prevents the agglomeration of graphene oxide nanosheets during the reduction reaction which facilitates more reactions in between the layers of graphene oxide which was not practical in the conventional chemical reaction. In addition to this, the radicals produced in the reaction medium during ultrasound irradiation will also plays an important role in the reduction of GO into graphene. The previous study of Vinodgopal et al demonstrated the partial reduction of GO into graphene nanosheets after 4 hrs of ultrasound irradiation [59]. Due to ultrasound irradiation, more reactive site for the epoxide and hydroxyl removal using hydrazine was created in the reaction and additionally, the effect of extreme temperature, pressure and high cooling rates due to the acoustic cavitation phenomena catalyzes the reduction reaction in a shorter time. Since graphene oxide is not thermally stable material above 200 °C, the high temperature produced during the ultrasound irradiation itself able to reduce GO into graphene. Hence, the ultrasound assisted approach for the synthesis of graphene sheets is a combined approach for the mechanical exfoliation and simultaneous reduction of graphene oxide into graphene nanosheets.

3.3.2 UV-visible spectral studies

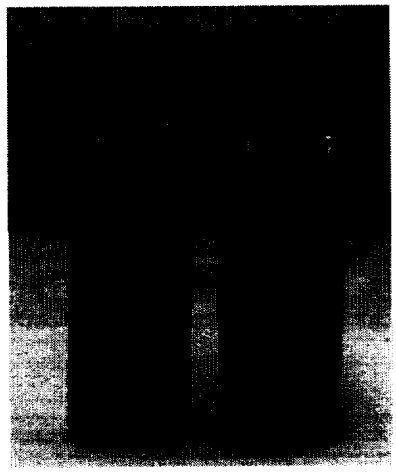

Figure 3.19 Digital image of aqueous dispersion of GO (brownish yellow) and graphene nanosheets (black).

The reduction reaction was monitored by the color change from brownish yellow to black. Figure 3.19 shows the digital image of graphene oxide solution before and after reducing into graphene. The black color of the US-rGO nanosheets confirmed the process of re-graphitization of GO by the removal of oxygenated functional groups. The UV-vis spectra of the GO and US-rGO were shown in Figure 3.20. The spectrum of GO shows a sharp absorption peak at 226 nm attributed to the π–π^* of the C–C aromatic rings [1] whereas the absorption peak of US-rGO was red shifted towards into 270 nm due to the increased electron concentration, structural ordering and consistent with the restoration of sp^2 carbon atoms [60]. The UV-vis spectrum of the control graphene shows the maximum absorbance around 254 nm depicting the partially reduced GO. This is in consistent with the previous results of Mathkar et al [61].

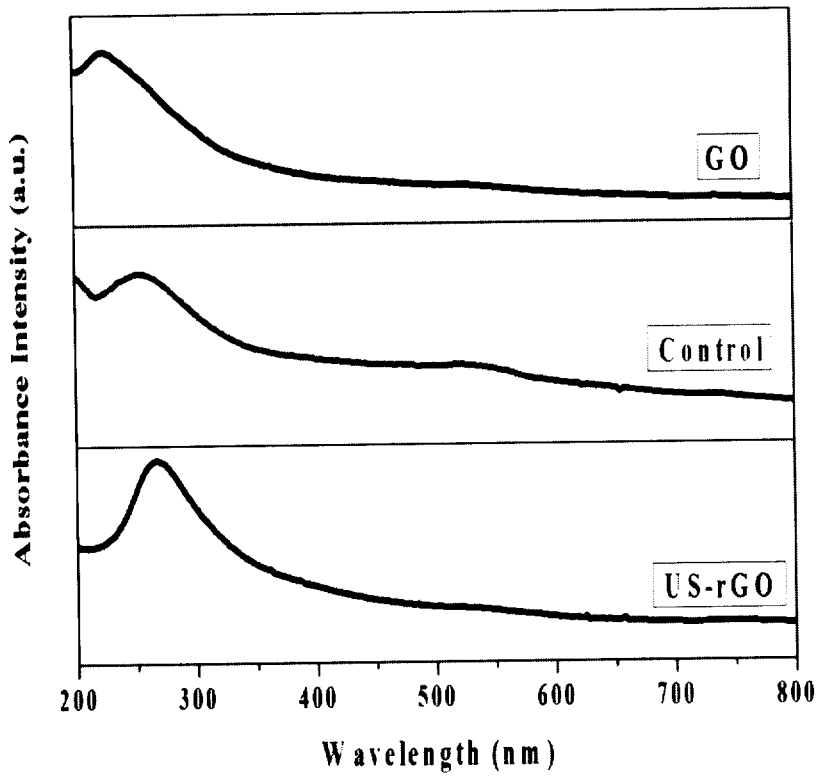

Figure 3.20 UV-vis spectra of GO, control graphene and US-rGO nanosheets.

3.3.3 Morphological characterization

Figure 3.21 shows a typical high resolution transmission electron microcopy (HR-TEM) image of the sonochemically synthesized graphene nanosheets and the control graphene. The HR-TEM image of the samples synthesized in the absence of ultrasound is given in Figure 3.21 (a). It shows the presence of aggregated sheets and the SAED pattern also confirms the polycrystalline nature of the sheets. There is no clear diffraction spots observed in the SAED pattern of control samples which is due to the aggregated sheets of partially reduced graphene oxide which results in the ring like pattern in the SAED pattern [62,63]. The HR-TEM image of the samples synthesized in the presence of ultrasound is given in Figure 3.21 (b). It depicts that the graphene sheets are of high transparency with the presence of wrinkles and folded

regions. The SAED pattern of the US-rGO nanosheets clearly shows the hexagonal diffraction spots corresponding to the monolayer graphene. This is in consistent with the previous report of Kim et al [62].

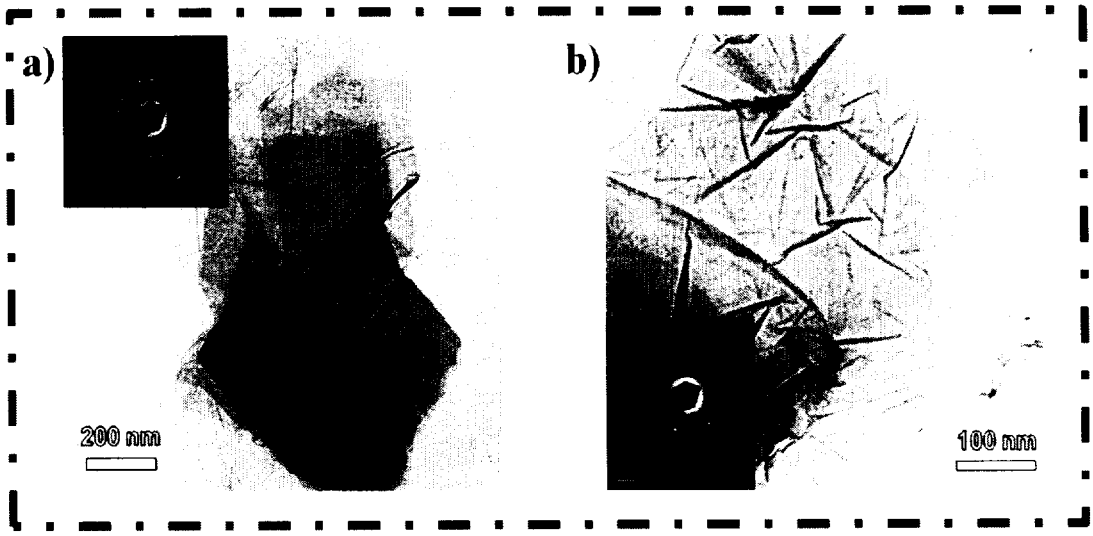

Figure 3.21 High resolution transmission electron microscopic images of a) control graphene and b) UV-rGO

3.3.4 XPS analysis

The XPS spectra of GO and graphene nanosheets are given in Figure 3.22. The XPS spectrum of GO exhibited the characteristic peaks of C–C skeleton, hydroxyl, epoxyl and carbonyl groups at 284.5, 286.2, 287.8 and 288.9 eV respectively [8]. As we expected, the XPS spectrum of US-rGO sheets shows only the binding energy corresponding to the C-C skeleton (at 284.5 eV) present in the graphene lattice with smaller amount of epoxyl groups. It clearly indicates that the intensities of other peaks related to the oxygenated functional groups such as hydroxyl, epoxyl and carbonyl are almost completely decreased which confirm the removal of the oxygenated functional groups [64]. The XPS of the graphene synthesized in the

absence of ultrasound shows the presence of C-O-C and C-OH groups along with the C-C skeleton. These results suggested that the control graphene is still not reduced since the reaction time is only two hours which is not sufficient for the complete reduction reaction. This can be agreed well with the previous report demonstrating the hydrazine reduction of GO into graphene in which the reaction time is about 12 hrs and 24 hrs respectively [65]. Hence, it confirms that within the same reaction time in the absence of ultrasound results in partially reduced graphene oxide. It also signifies the crucial role of ultrasound in the reduction reaction.

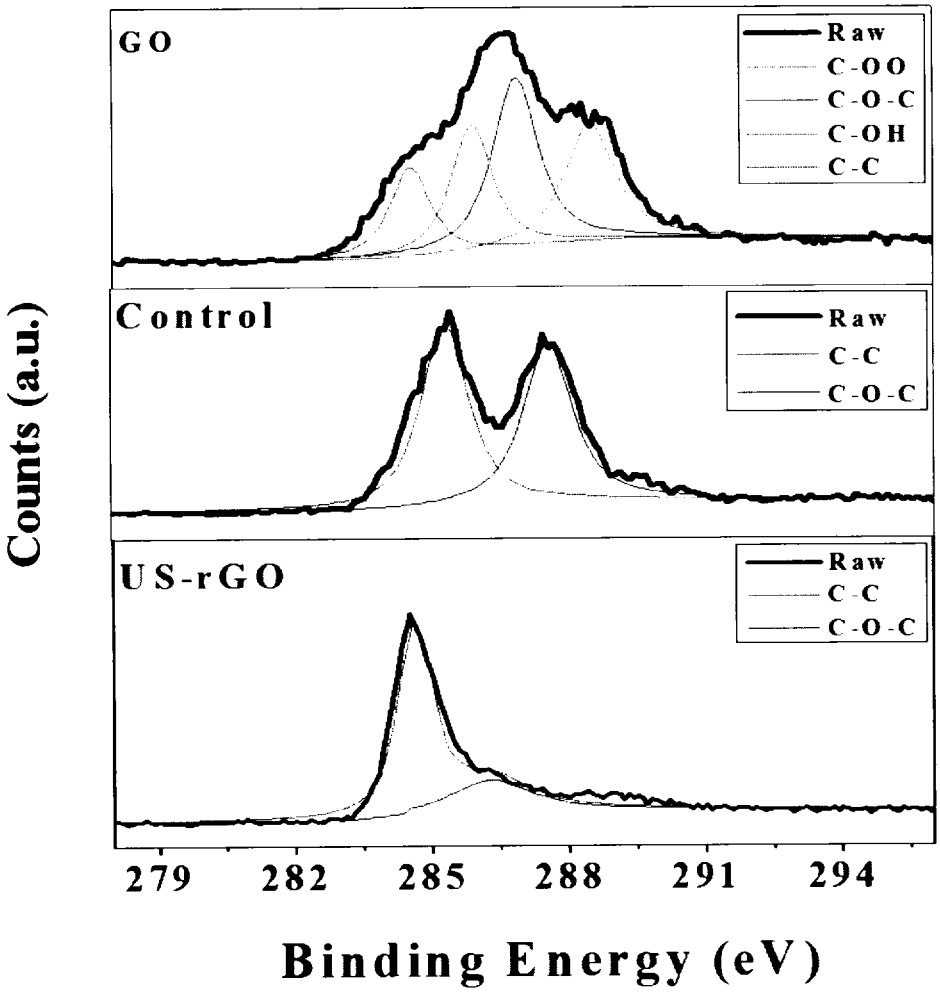

Figure 3.22 X-ray photoelectron (C 1s) spectra of GO, control graphene and US-rGO nanosheets.

3.3.5 Raman analysis

Raman spectroscopy provides us a non-destructive technique to study the bonding nature of various carbon materials such as graphene, GO and CNTs. Further characterizing the reduction of GO, Raman spectroscopy was employed to study the structure, defect levels and crystallinity of the as-synthesized graphene nanosheets and are compared with GO. In general, Raman spectrum of graphite exhibits a band at 1580 cm^{-1} named as "G band" and other band at 1350 cm^{-1} named as "D band". The former is due to the first order scattering of E_{2g} mode and latter associates with the defects in the graphite lattice [9]. The Raman spectra of GO and graphene nanosheets are provided in Figure 3.23. The Raman spectrum of GO possesses the G band at 1595.89 cm^{-1} and D band at 1354 cm^{-1} [10]. As compared with the Raman spectrum of graphite, the G band in GO is shifted towards higher wavenumber which is due to the oxygenation of graphite [12]. The increase in FWHM of the G band in the GO compared with the graphite suggests the presence of sp^3 carbon in GO. The D band in GO is broadened which was due to the reduction in size of in plane sp^2 domains by the creation of defects, vacancies and distortions of the sp^2 domains after complete oxidation [13]. The Raman spectrum of US-rGO shows significant changes compared with the spectrum of GO. In case of graphene, the G band is shifted towards lower wave number (1588.41 cm^{-1}) due to the recovery of hexagonal network of carbon atoms with defects. In case of the D band, it becomes narrow and the intensity is increased in graphene compared to that of GO which illustrates the sonochemical reduction process modified the structure of graphene with defects. Moreover, the FWHM of the D peak in graphene becomes decreased due to the increase in average size of the sp^2 clusters. The Raman spectrum of the sample synthesized in the absence

of ultrasound clearly evidenced that the reduction reaction results in partially reduced state since the G peak is observed at 1593.6 cm^{-1} [28]. This is in consistent with the reduced graphene oxide was obtained using galactose. There is no obvious change in D band and the I_D/I_G value of the control graphene compared to GO suggests that the reduction reaction is not well proceeded since the control graphene is in partially reduced state.

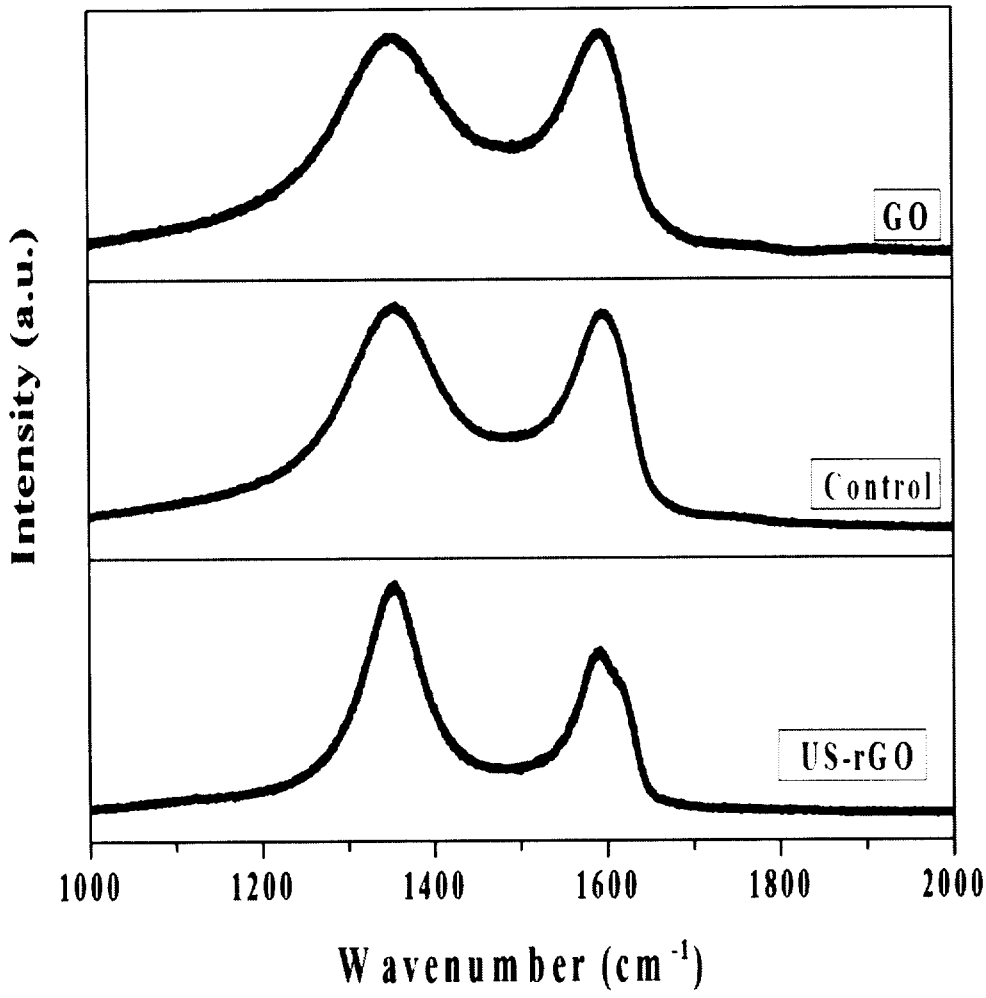

Figure 3.23 Raman spectra of GO, control graphene and US-rGO nanosheets.

The intensity of G band $(I_{(G)})$ and D band $(I_{(D)})$ is used to measure the average crystallite size of the sp^2 domains. The well known Tuinstra and Koenig (TK) relation

is employed to determine the average size of the sp^2 clusters in GO and graphene as follows [41]:

$$I_{(D)}/I_{(G)} = C(\lambda)/L_a \quad \text{..... [2]}$$

where $I_{(D)}$ is the intensity of the D peak, $I_{(G)}$ is the intensity of the G peak, $C(\lambda)$ is the wavelength dependent prefactor and L_a is the average crystallite size of sp^2 domains. The average crystallite size of the sp^2 domains in GO and graphene were measured as 4.48 and 3.25 nm, respectively. The average crystallite size of sp^2 domains is decreased in US-rGO nanosheets compared to GO. This is due to the formation of new sp^2 carbon atoms which are smaller in size compared to the sp^2 carbon atoms present in GO before reduction [12]. The decrease in FWHM of G band in graphene ensures the formation of new sp^2 carbon atoms in graphene.

Overall, the reduction of graphene oxide into graphene nanosheets was achieved by a facile sonochemical approach. The physiochemical characterizations performed above suggests the reduction of GO into graphene nanosheets. However, a detailed study about the effect of ultrasonic frequency, time and amount of reducing agent will provide a new strategy for graphene synthesis using sonochemical approach. Still compared with the other conventional methods reported for the synthesis of graphene, the sonochemical method reported here is relatively fast, since graphene can be synthesized within 2 hrs.

Being fast, effective and economical benign, we believe that the ultrasound assisted synthesis of graphene nanosheets may become a promising method for preparation of graphene due to their wide spread applications in various sectors.

3.4 Hydrothermal reduction of graphene oxide into graphene nanosheets

Graphene nanosheets were successfully synthesized by improved hydrothermal reduction of GO. At first, the GO nanosheets are synthesized according to the modified Hummers method. The obtained GO nanosheets are exfoliated into monolayers of GO by ultrasonication prior to the reduction reaction. The solution is adjusted to reach pH 10 by the addition of NaOH and then hydrazine hydrate followed by the hydrothermal treatment as described in the experimental section. The mechanism of reduction of GO into graphene nanosheets can be described as follows: GO with several oxygenated functional groups on its basal plane and at the edges can be deoxygenated in alkaline solution as suggested by Fan et al [56]. Hydrazine hydrate is commonly used for the reduction of functional groups in GO [12]. Additionally, the hydrothermal reaction enhances the reaction rate and kinetics due to the high pressure in hydrothermal conditions. [66] The obtained graphene nanosheets are black in color, which confirms the reduction of GO into graphene nanosheets was successfully achieved.

3.4.2 UV-vis spectroscopy studies

A photographic image of the aqueous dispersions of graphene nanosheets (black) is shown in the inset of Figure 3.24. The change in color from brownish yellow (GO) to black confirms the reduction of GO into graphene by the hydrothermal approach. The reduction of GO into graphene is characterized by UV-vis spectroscopy studies as shown in Figure 3.24. The UV-vis spectrum of GO shows a sharp absorption peak at 226 nm, this is attributed to the π–π * of the C–C aromatic rings. After the reduction reaction, the absorption spectrum of graphene shows a maximum absorption at 267 nm. The occurrence of a red shift in the absorption

spectra of graphene is due to the increased electron concentration due to removal of sp^3 carbon atoms and is also consistent with the restoration of sp^2 carbon atoms [60].

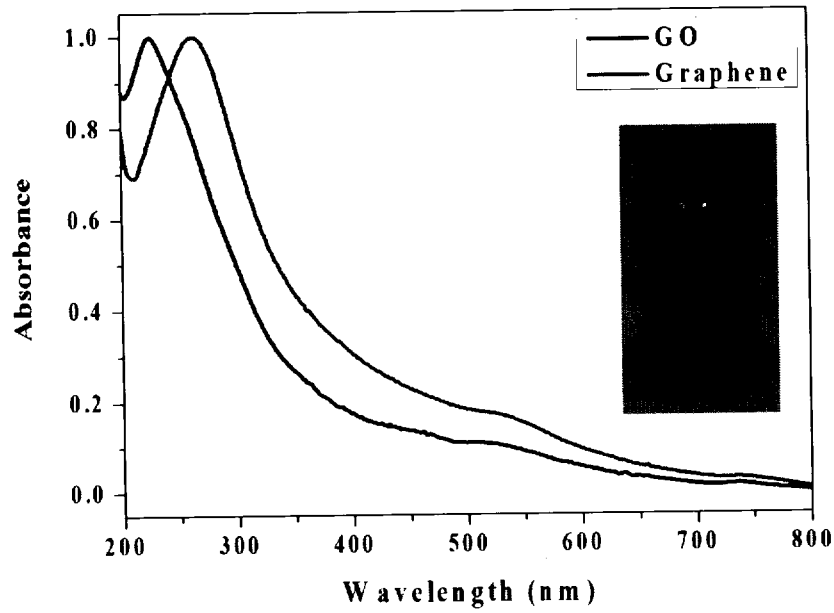

Figure 3.24 UV-vis spectra of GO and graphene nanosheets (hydrothermal method)

3.4.3 X-ray diffraction studies.

Figure 3.25 depicts the XRD pattern of the GO and graphene nanosheets. The diffraction peak of pure graphite is found around 26°. After successful oxidation, the diffraction peak of graphite at 2θ = 26° completely disappeared and a new broad peak around 2θ = 10° due to the oxidation of graphite appears. The corresponding interlayer spacing of GO was measured as 0.85 nm. The reduction of GO into graphene is confirmed by the XRD pattern of graphene which shows a broad diffraction peak at 2θ = 26° corresponding to an interlayer spacing of 0.35 nm. The disappearance of the peak at 2θ = 10° in the GO and the formation of new broad peak at 2θ = 26° further supports that the GO is completely reduced into graphene. The obtained XRD results are in agreement with the previous findings of Zhang et al [67].

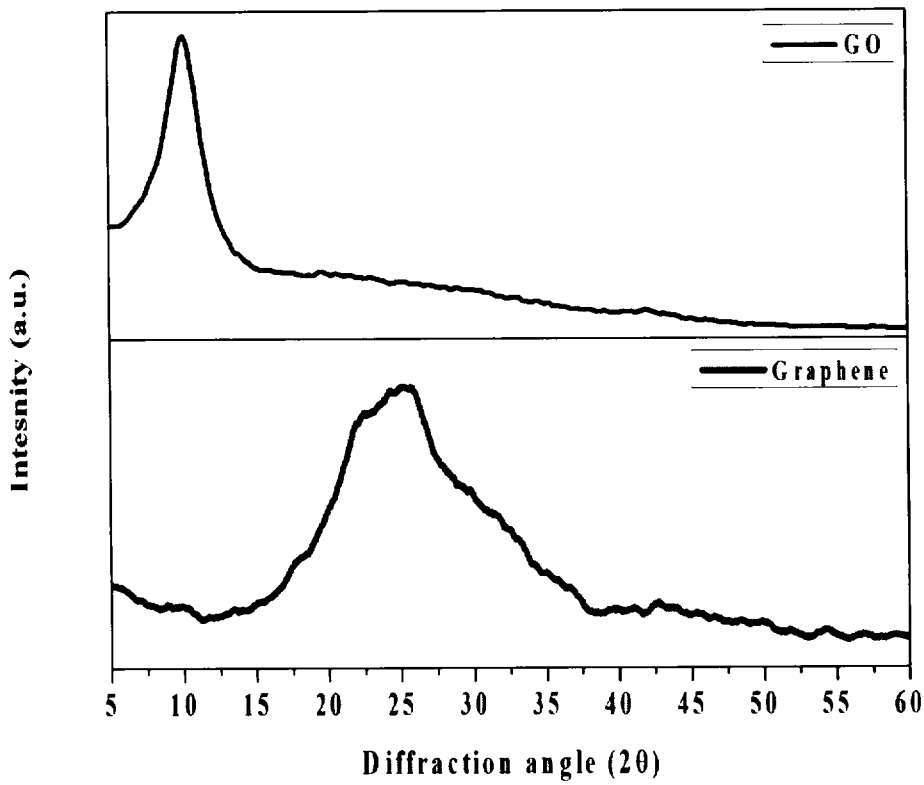

Figure 3.25 XRD pattern of GO and graphene nanosheets (hydrothermal method).

3.4.4 Surface morphology studies

Figure 3.26 (a) and (b) shows the field-emission scanning electron micrograph (FE-SEM) of the hydrothermally synthesized graphene nanosheets with different magnifications. It shows the wavy features of graphene, which are due to the surface crumpling. Figure 3.26 (c) and (d) shows the typical transmission electron microcopy images of the graphene nanosheets. It depicts that the sheets like morphology of graphene with high transparency. It also shows the presence of wrinkles and folded regions in the synthesized graphene nanosheets. The clear diffraction spots obtained in the SAED pattern [as shown in inset of Figure 3.26 (d)] illustrates the hexagonal lattice and the discontinuity in the pattern is due to the super position of two hexagonal patterns which is generally observed in few layer graphene [62].

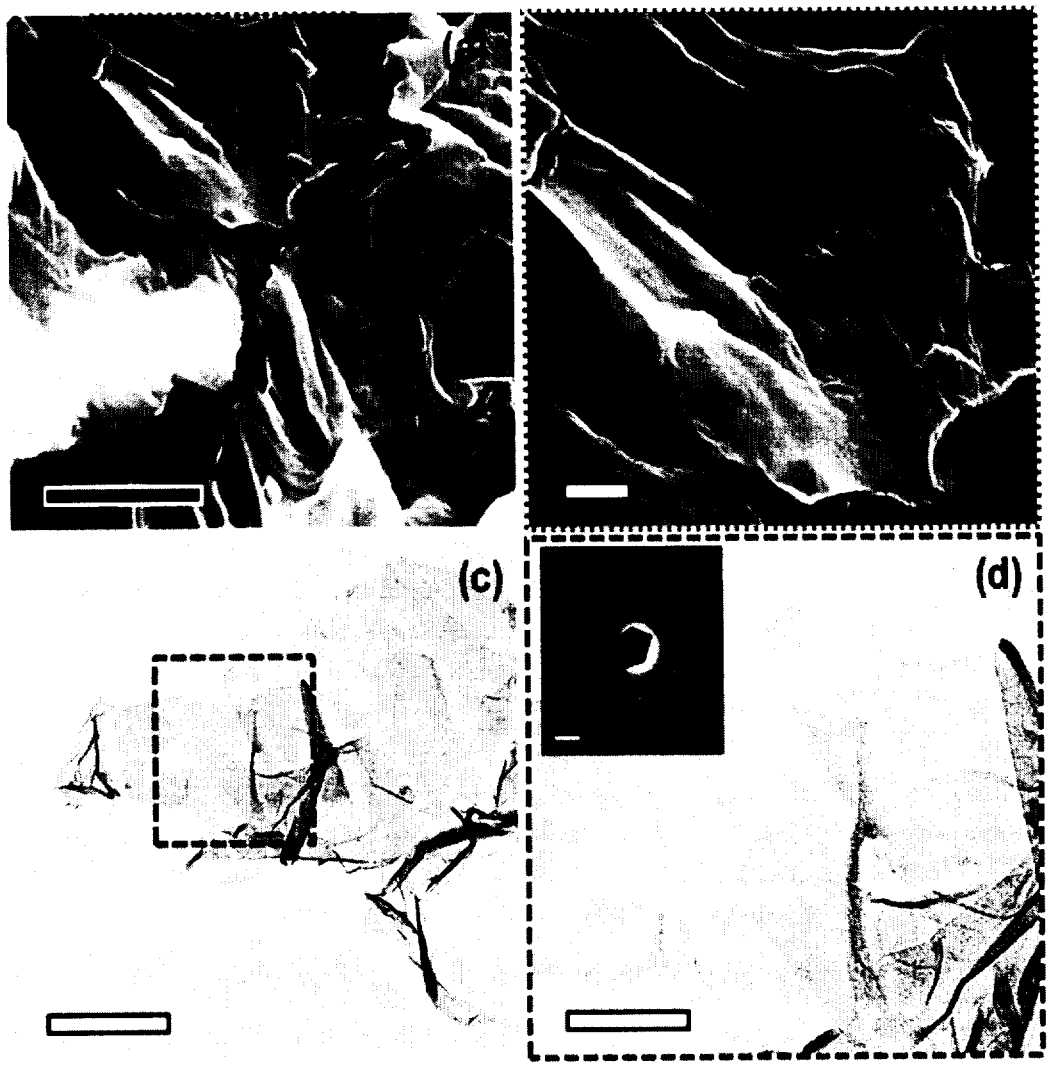

Figure 3.26 FE-SEM (a: scale bar = 1 μm; b: scale bar = 100 nm) and HR-TEM images (c: scale bar = 200 nm; d: scale bar = 50 nm) of graphene nanosheets. Inset in (d) shows the SAED pattern of graphene nanosheets (scale bar = 2 nm^{-1}).

3.4.5 FT-IR studies

The FTIR spectra of GO and graphene nanosheets are measured to study the removal of oxygen containing functional groups in graphene after the reduction reaction. Figure 3.27 shows the FTIR spectra of the GO and graphene nanosheets. The

FTIR spectra of the GO clearly shows the presence of carboxyl, hydroxyl, epoxyl and carbonyl groups at 1728 cm^{-1}, 1413 cm^{-1}, 1200 cm^{-1} and 1050 cm^{-1} respectively. The peak due to the C–C vibrations from the graphitic domains is observed at 1600 cm^{-1}. In the FTIR spectra of graphene, the peak at 1600 cm^{-1} arises due to the C-C skeleton and the other peaks due to the oxygenated functional groups such as carboxyl, hydroxyl, epoxyl and carbonyl groups are not observed suggesting that GO was reduced into graphene nanosheets [68].

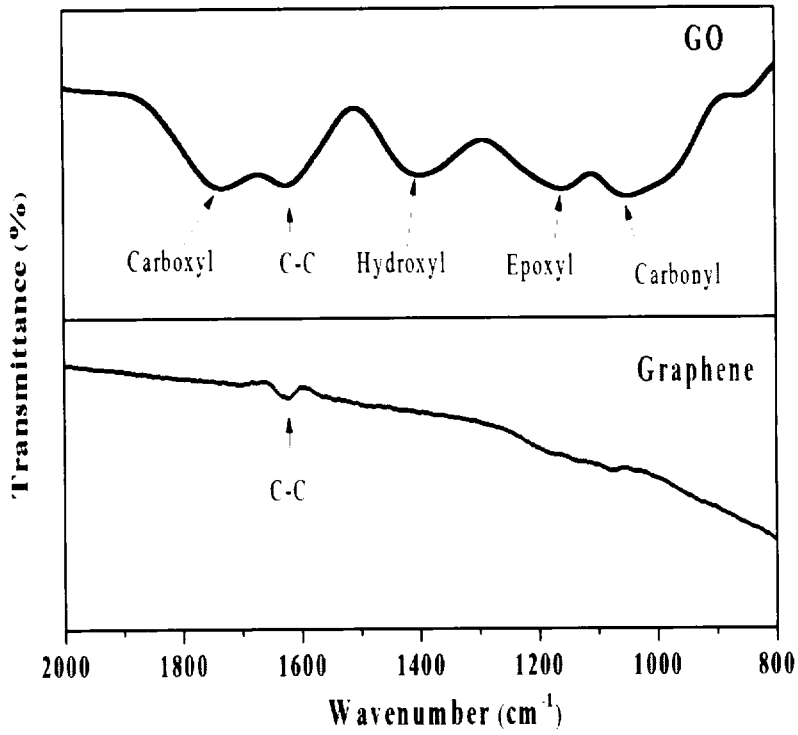

Figure 3.27 FT-IR pattern of GO and graphene nanosheets (hydrothermal method).

3.4.6 X-ray photoelectron studies

The chemical composition and state of elements present in GO and graphene are characterized by X-ray photoelectron spectroscopy. The comparative XPS spectra of GO and graphene nanosheets are given in Figure 3.28. The XPS spectrum of the

GO exhibited the characteristic peaks of C–C skeleton, hydroxyl, epoxyl and carbonyl groups at 284.5, 286.2, 287.8 and 288.9 eV respectively [8]. The presence of these different oxygenated functional groups in GO is due to the oxidation of graphite which makes them hydrophilic in nature. The reduction of GO into graphene shows a drastic change in the XPS spectrum of graphene. From Figure 3.28, it is clear that graphene sheets show only the presence of a C-C skeleton (at 284.5 eV) with presence of a smaller amount of epoxyl groups. In comparison with the XPS of GO, the fact that the intensities of peaks related to the oxygen related functional groups such as hydroxyl, epoxyl and carbonyl almost completely disappeared in the XPS of graphene further confirms the removal of the oxygenated functional groups due to the hydrothermal reduction process [69].

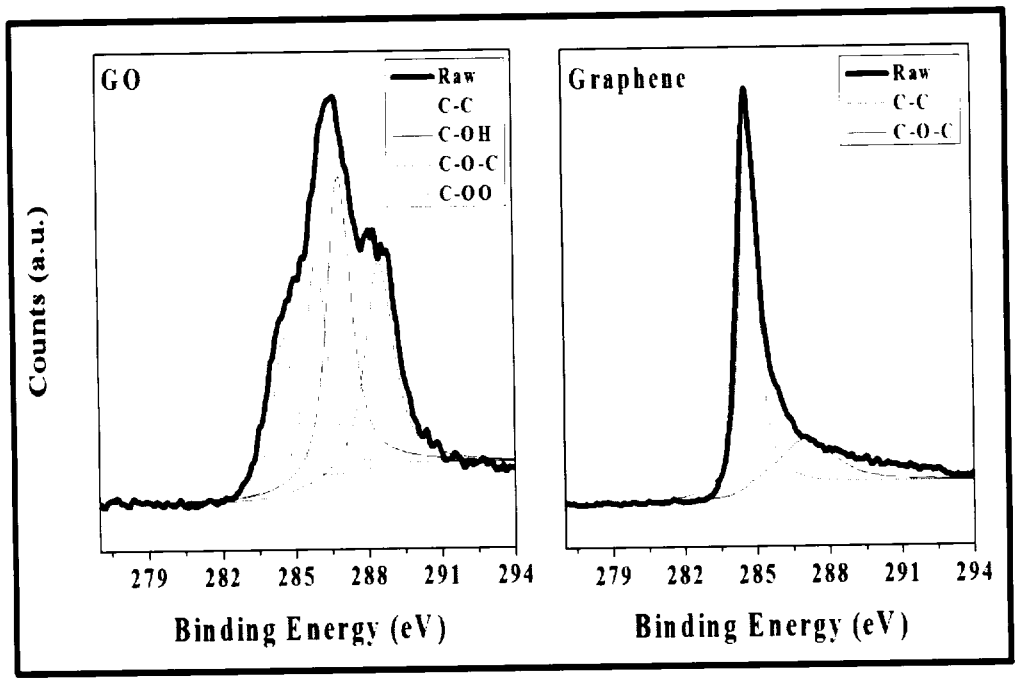

Figure 3.28 XPS spectra of GO and graphene nanosheets (hydrothermal method)

3.4.7 Raman spectroscopic investigations.

Raman spectroscopy was employed to study the crystallinity, disorder and defect levels of the graphene nanosheets which are compared with GO. In general, the Raman spectrum of graphite exhibits a "G band" at 1570 cm^{-1} and a "D band" at 1350 cm^{-1}. The occurrence of the G band is due to the first order scattering of the E_{2g} mode and the "D band" associates with the defects in the graphite lattice [9,10]. The Raman spectrum of the GO and graphene nanosheets are shown in Figure 3.29. The Raman spectrum of GO shows the presence of a G band at 1595.89 cm^{-1} and a D band at 1354 cm^{-1}. The G band in GO is shifted towards a higher wavenumber, this is due to the oxygenation of graphite which results in the formation of sp^3 carbon atoms. The D band in the GO is broadened due to the reduction in size of the in-plane sp^2 domains by the creation of defects, vacancies and distortions of the sp^2 domains during oxidation. The Raman spectrum of graphene shows significant changes compared with the spectrum of GO. In the case of graphene, the G band is shifted towards a lower wave number (1589.41 cm^{-1}) due to the re-graphitization that results in the formation of more sp^2 carbon atoms. This is in agreement with previous reports on chemically synthesized graphene [70]. The D band becomes narrow and the intensity is increased suggests that the hydrothermal process modified the structure of graphene with defects.

The intensity of the G band ($I_{(G)}$) and D band ($I_{(D)}$) is used to measure the average crystallite size of the sp^2 domains. Cancodo et al. provided the general equation [43] of determination for the average crystallite size of the sp^2 domains L_a in the nanographite sytems by relating the $I_{(D)}/I_{(G)}$ ratio to the fourth power of the laser energy used in the experiment as follows:

$$L_a\,(\text{nm}) = [(2.4*10^{-10})\,(\lambda_l)^4] \,/\, [I_{(D)}/I_{(G)}] \quad \ldots\ldots\ldots\ldots\ldots\ldots\ldots\ldots (1)$$

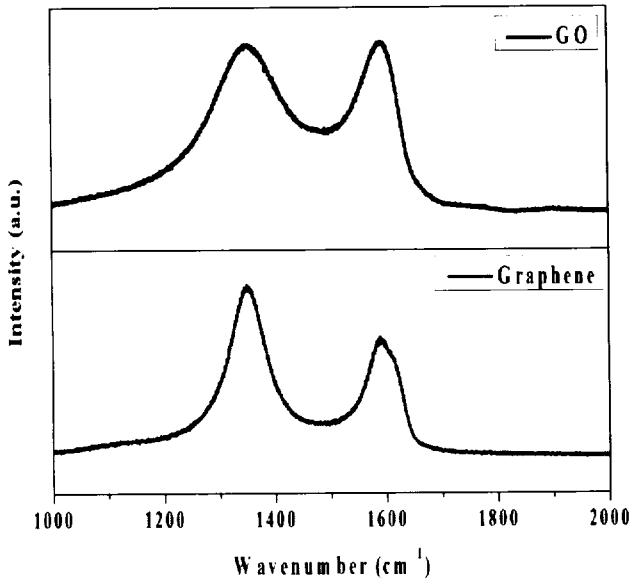

Figure 3.29 Raman of GO and graphene nanosheets (hydrothermal method).

where L_a is the average crystallite size of the sp^2 domains, λ_l is the input laser energy $I_{(D)}$ is the intensity of the D band, and $I_{(G)}$ is the intensity of the G band. The average crystallite size of the sp^2 domains in GO and graphene were measured as 15.45 and 11.76 nm, respectively. The average crystallite size of sp^2 domains is decreased in graphene compared to GO. This is due to the formation of new sp^2 carbon atoms which are smaller in size than the sp^2 carbon atoms present in GO before the reduction [12]. The decrease in FWHM of the G band in graphene ensures the formation of new sp^2 carbon atoms in graphene.

3.4.8 Zeta potential studies

The stability of nanomaterials in dispersion state is one significant issues for the biomedical applications of nanoparticles [71]. Hence, we measured the zeta potential of graphene nanosheets in an aqueous dispersion and is shown in Figure 3.30. The zeta potential of graphene nanosheets was found to be -26.75 mV (whereas the

zeta potential of GO is -51.2 mV). It is well known that GO has a highly negative zeta potential due to the ionization of edge carboxylic groups [72]. The reduction in zeta potential of the graphene nanosheets is attributed to the removal of functional groups after the reduction reaction. The observed zeta potential of graphene nanosheets (-26.75 mV) is well beyond the accepted values of colloidal stability (±25 mV) indicating its high stability in dispersion [73]. The observed value of the zeta potential of graphene nanosheets is matched well with the previous published reports [74].

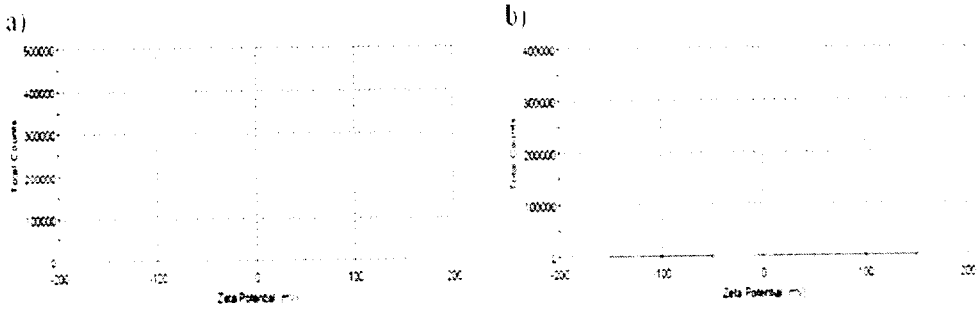

Figure 3.30 Zeta potential of a) GO dispersion and b) graphene dispersion.

Finally, graphene nanosheets were synthesized by a hydrothermal method under alkaline conditions. The XRD and UV-vis spectra showed the formation of graphene nanosheets with a re-graphitization process. The FE-SEM and HR-TEM studies showed the sheet like morphology of the as-synthesized graphene. The FT-IR and XPS spectra confirmed the removal of oxygenated functional groups in graphene after the reduction reaction. The Raman spectroscopy illustrated the formation of new sp^2 carbon atoms in graphene due to the reduction of GO.

3.5 Reduction of GO by D-galactose

In this study, we a used a bio-sugar D-galactose as a reducing agent for the reduction of GO into graphene. The use of this new reducing agent offers a way to the eco-friendly non-toxic reducing agent compared to the conventional reducing agents such as hydrazine, sodium borohydrate which are toxic to environment.

3.5.1 UV-visible spectra

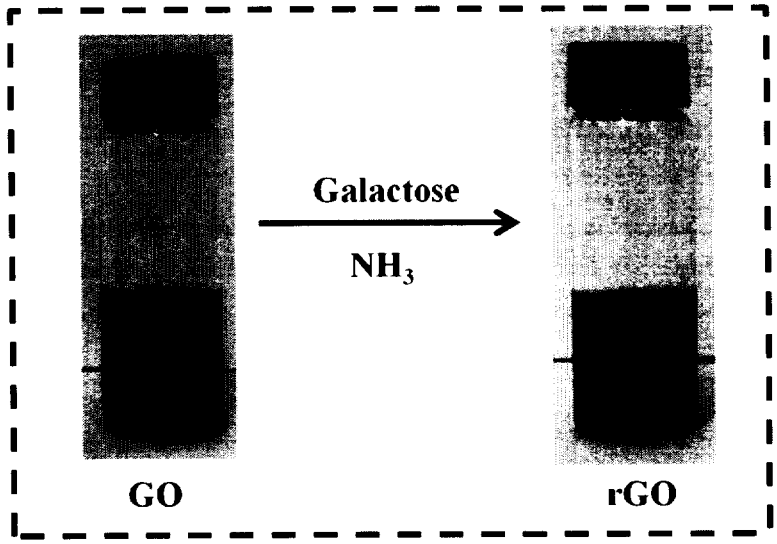

Figure 3.31 Reduction of GO nanosheets into reduced graphene oxide (rGO) nanosheets results in a color change from brown (GO) into black (rGO).

In this study, GO was synthesized according to the modified Hummers method and is discussed in chapter 1. The reduction reaction of graphene oxide into graphene sheets was monitored by the color change from brown into black as shown in Figure 3.31 followed by the UV-vis spectroscopy. The black color of the rGO material suggested the re-graphitization of the exfoliated GO by the removal of oxygenated functional groups. Figure 3.32 depicts the UV-vis spectra of the GO showing a sharp absorption peak at 226 nm which is attributed to the π-π^* of the C-C aromatic rings. After the reduction of GO, the absorption peak was red shifted towards into 270 nm due to the formation of rGO. The significant red shift in rGO is due to the increased

electron concentration, structural ordering and consistent with the restoration of sp^2 carbon atoms [60].

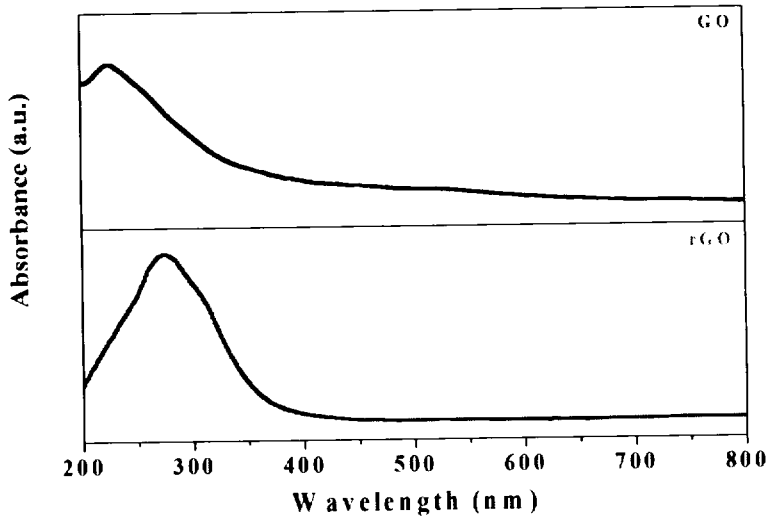

Figure 3.32 UV-visible spectra of GO and rGO nanosheets.

3.5.2 X-ray diffraction analysis and surface morphology

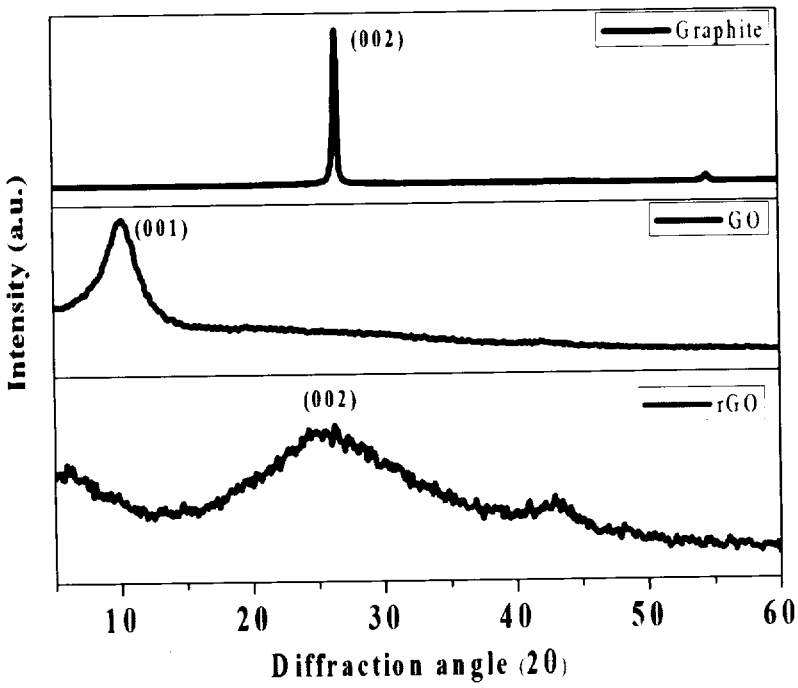

Figure 3.33 X-ray diffraction patterns of graphite, GO and rGO.

Figure 3.33 shows the XRD pattern of graphite, GO and rGO respectively. The diffraction peak of pure graphite is found around 26°. After successful oxidation, the diffraction peak of GO shifted towards $2\theta = 10°$ which is mainly due to the oxidation of graphite and the corresponding interlayer spacing was 0.85 nm [3]. The reduction of graphene oxide into rGO is also confirmed by the XRD pattern of rGO which shows a broad diffraction peak at $2\theta = 26°$ corresponding to the interlayer spacing of 0.35 nm. The complete disappearance of peak at $2\theta = 10°$ of the GO and the formation of new broad peak at $2\theta = 26°$ further supports that the graphene oxide is completely reduced into rGO[67]. Figure 3.34 shows the TEM image of the reduced graphene oxide showing sheet like morphology which are transparent and wrinkled at the edges.

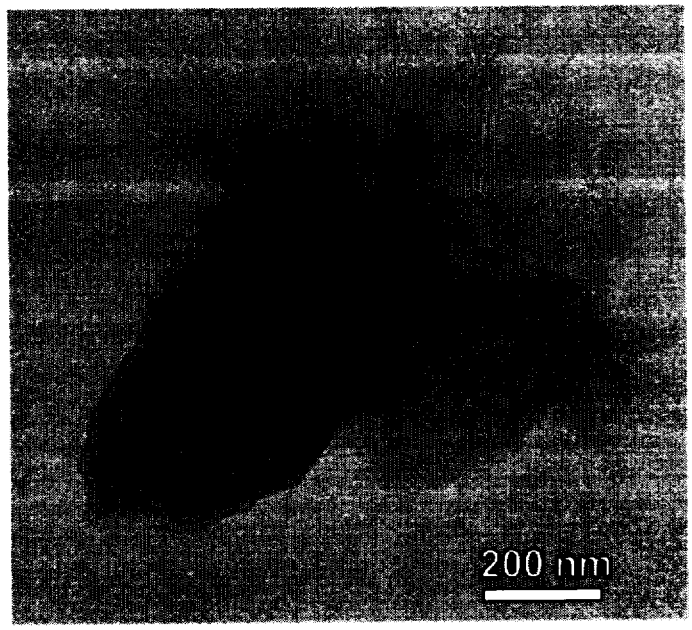

Figure 3.34. TEM image of synthesized rGO showing sheet like morphology.

3.5.3 XPS analysis

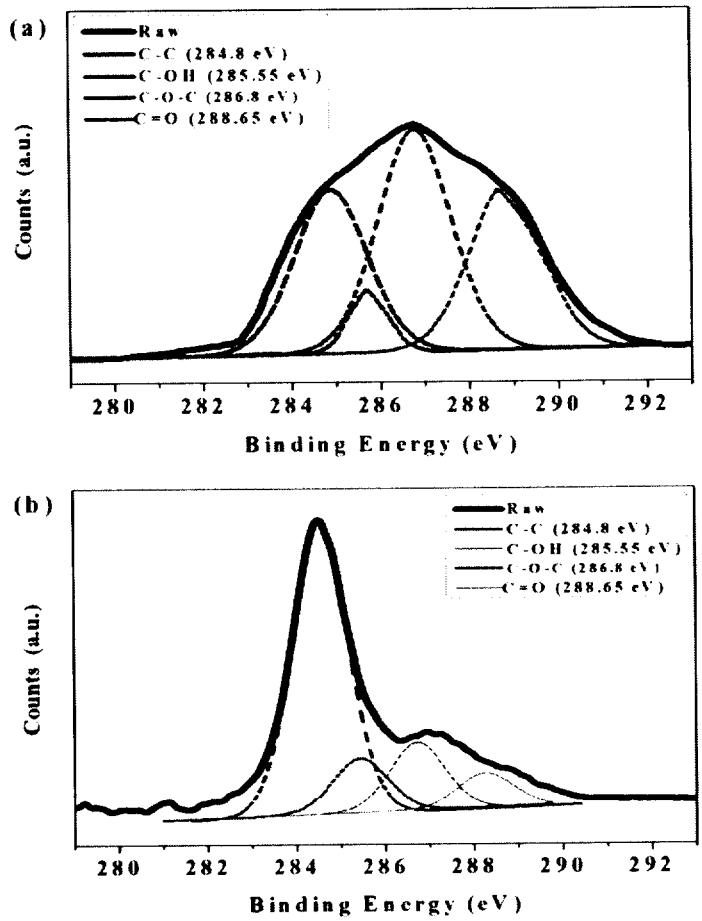

Figure 3.35. X-ray photoelectron spectra (XPS) of (a) GO and (b) rGO.

The removal of oxygenated functional groups from GO after reduction into graphene is studied by XPS technique as shown in Figure 3.35. XPS of GO exhibits the following peaks at 284.8, 285.55, 286.8 and 288.65 eV corresponding to the C-C in the aromatic rings, hydroxyl, epoxyl and carbonyl groups respectively [8]. During the reduction reaction, the hydroxyl, carbonyl and epoxyl groups in GO were effectively reduced by D-galactose. In the XPS of rGO, only the peak due to the C-C bond at 284.8 eV is preserved and all the intensities of other peaks related to the

bonding between the carbon and the oxygen such as hydroxyl, epoxyl and carbonyl are relatively decreased, strongly suggests the removal of the oxygenated functional groups [64].

3.5.4 Raman spectral analysis

In order to further characterize the reduction reaction and to study the nature of sp^2 domains, Raman analysis were performed on the reduced GO and compared with GO as shown in Figure 3.36. The Raman spectra of graphite show a strong G peak at 1570 cm^{-1} due to the first order scattering of E2g mode [9]. The Raman spectra of graphene oxide show that the G peak is shifted towards 1595.89 cm^{-1} due to the oxygenation of graphite [12]. In addition to this, a broadened D peak at 1350 cm^{-1} is also appeared due to the reduction in size of *in plane* sp^2 domains in graphite induced by the creation of defects, vacancies and distortions of the sp^2 domains after complete oxidation [13].

After reduction of graphene oxide, the G peak is shifted towards lower wave number (1591.41 cm^{-1}) compared to that of GO which agrees with the previous reports [70]. This shift was attributed to the recovery of hexagonal network of carbon atoms with defects. The D peak intensity is increased in rGO compared to that of GO suggesting that the reduction process modified the structure of GO with defects. However, the decrease in FWHM of the D peak in rGO is due to the increase in average size of the sp^2 clusters. The $I_{(D)}/I_{(G)}$ ratio are used to evaluate the average size of the sp_2 cluster in the graphene materials. The corresponding $I_{(D)}/I_{(G)}$ ratio of GO and rGO are measured as 0.8 nm and 0.9 nm respectively. The average size of the sp^2 clusters in GO and rGO were calculated using the Tuinstra and Koenig relation as 5.28 and 4.57 nm respectively. The decrease in average size of sp^2 clusters is due to

the formation of new sp^2 clusters which are smaller in size compared to the ones present in GO before reduction [12].

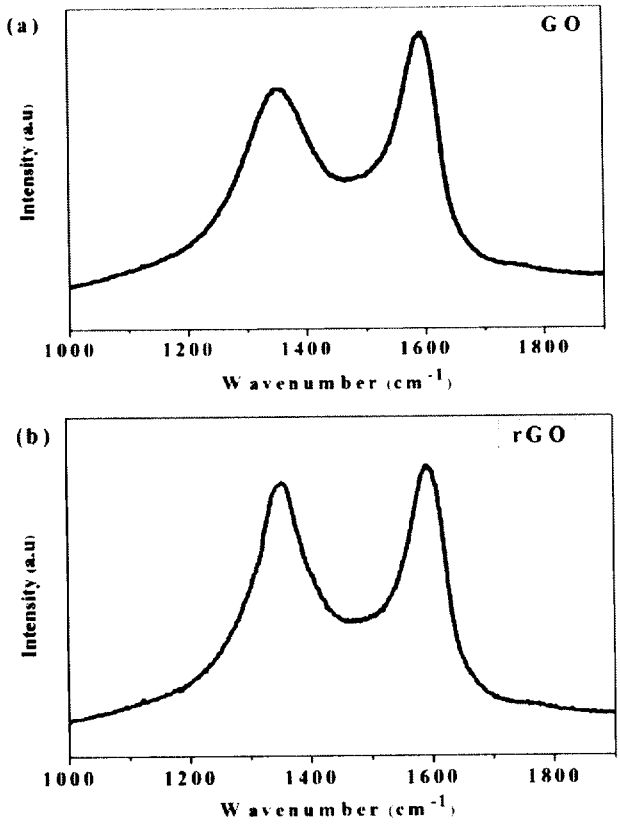

Fig. 3.36. Raman spectra of (a) GO and (b) rGO nanosheets.

3.5.5 Thermal studies

The thermal stability of the rGO is studied using thermo gravimetric analysis (TGA) and compared with the GO and the precursor graphite as shown in Figure 3.37. The TGA analysis of graphite shows the high thermal stability of graphite even at 1000 °C. Since GO is thermally unstable, it starts losing the mass from 100 °C due to the removal of moisture content. The major mass loss occurs at 200 °C due to the removal of oxygen containing functional groups such as CO, CO_2 and H_2O vapors. In case of rGO, already the oxygen containing functional groups were removed during the reduction process, yielding a better thermal stability than the GO. The TGA of

rGO shows the removal of water content at 100 °C. This is well agreed with the previous report on reduced graphene sheets [12]. All these results suggest that graphene oxide is reduced into graphene sheets by using D-galactose as a reducing agent.

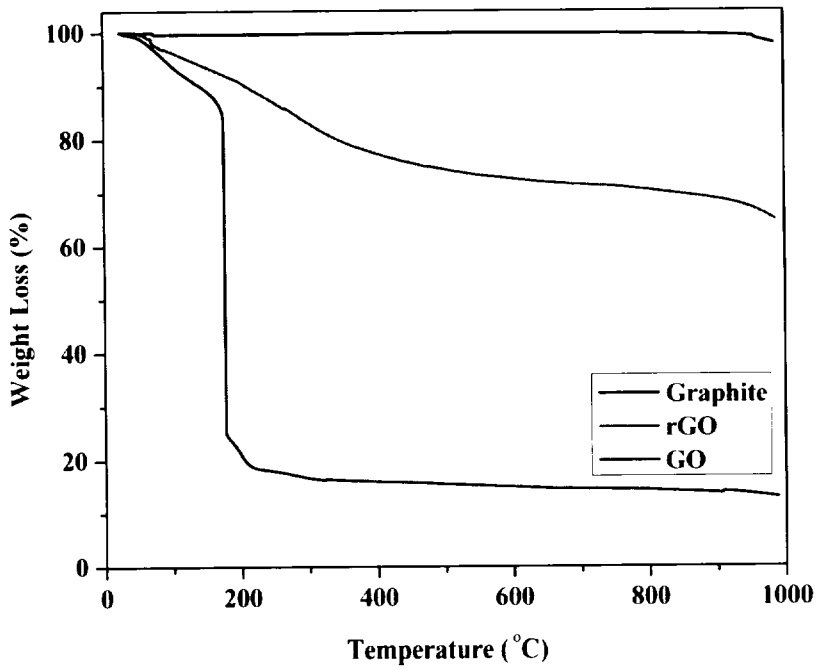

Figure 3.37 Thermogravimetric analysis of graphite, GO and rGO.

3.5.6 Photoluminescence of reduced graphene oxide nanosheets

The study on the optical properties of graphene sheets is an important aspect for its application in photonics [75]. The oxidation of graphite causes the formation of graphitic islands in GO which produces a disruption of the π-network and thus opens up a band gap in the electronic structure [76]. Figure 3.38 shows the photoluminescence spectra of GO and rGO nanosheets recorded using an excitation wavelength of 325 nm. The PL spectrum of GO shows a sharp emission peak in the near ultraviolet UV region at 365 nm corresponding to the band emission of GO. The unusual strong intensity at 650 nm is not due to the GO sample but due to the overlap

of the second order emissions associated to the excitation wavelength. The UV emission in GO is due to the oxidation of graphite which produce various sizes of crystalline graphitic sp^2 clusters surrounded by amorphous sp^3 matrix in GO which act as a high tunnel barrier resulting in the creation of band gap in GO. PL response of graphene oxide in the low energy region has been reported earlier recently [77].

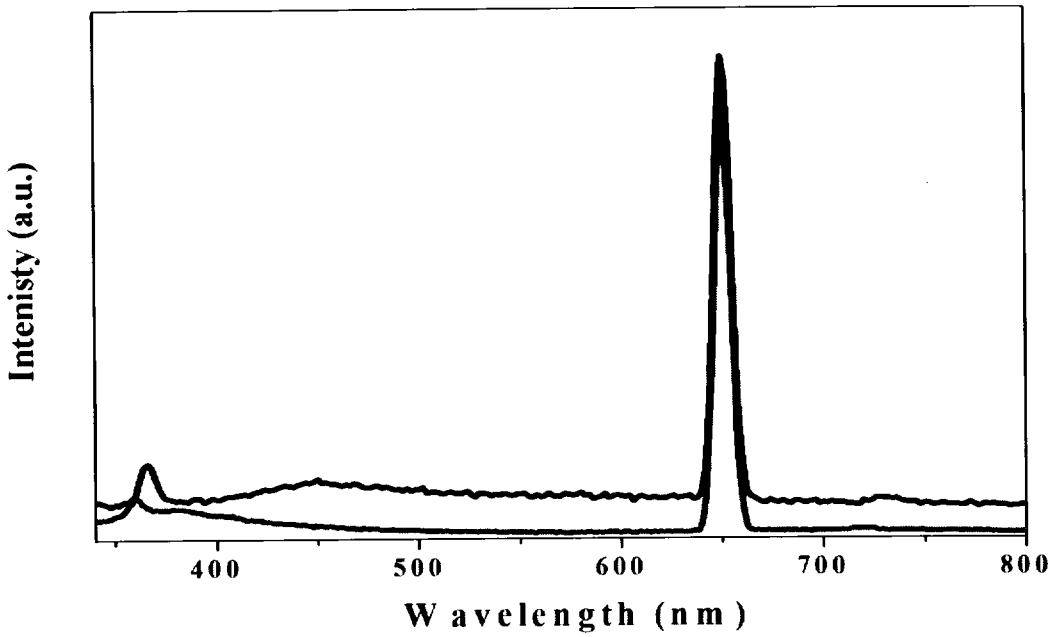

Figure 3.38 Photoluminescence spectra of GO and rGO.

The PL spectrum of rGO nanosheets also exhibit a sharp emission at 650 nm due to the overlap of the second order emissions as similar in GO. This second order emission was verified by using a range of excitation wavelength (325, 400 and 500 nm). The near band emission is quenched and blue shifted (359 nm) after the reduction process. The intensity of the PL emission of rGO is reduced ½ times compared to GO after the reduction process shows the quenching in PL emission. This is in agreement with the recent report by Li et al [78]. Although, the mechanism of light emission from rGO still unclear and remains unexplored, the quenching of PL quantum yields is possibly due to the following reason. The quenching of PL in rGO

is due to the removal of functional groups which is due to the restoration of more number of sp^2 clusters in the graphene sheet after reduction. The newly formed sp^2 clusters in rGO can provide percolation pathways between sp^2 clusters already present. Thus, the reduction of GO results in formation of zero gap regions in the rGO sheets with some of the functional groups remains still unreduced even after the reduction process. This ensures that the ratio of the zero gap sp^2 clusters is comparatively high enough to the sp^3 clusters in the rGO sheets resulting in quenching of photoluminescence due to weak carrier confinement. This is supported with our XPS spectra [Figure 3.35] and Raman spectra [Figure 3.36] of the rGO sheets. Hence with our results, we can believe that the photoluminescence in GO and rGO depends on the size or length scale of the graphitic regions (sp^2 domains) and the oxidized regions (sp^3 domains). In this regard, it is much needed to investigate more about the levels of oxidized and unoxidized region in both GO and rGO since there is no straightforward relationship exists.

Herein, the GO nanosheets are reduced using a combination of galactose and ammonia. The XRD and UV results suggested the reduction of GO into graphene. XPS analysis shows the removal of oxygenated functional groups in GO after reduction. Raman analysis revealed the structural changes occurred in GO after reduction Moreover, the obtained rGO sheets exhibited quenching in PL emission spectra and blue shifted due to increased sp^2 clusters after reduction.

3.6 Plasma assisted reduction of GO into graphene nanosheets

3.6.1 Mechanism of plasma reduction of GO

The mechanism of reduction of GO into graphene nanosheets occurred in this study is probably due to the radical assisted reduction. The radicals generated in the Ar/H_2 plasma plays a key role in the removal of oxygenated functional groups in GO. There are several reports demonstrated the radical chemistry underlying the Ar/H_2 plasma and the following reactions will be occurred during the reaction.

$$Ar + H_2 \longrightarrow ArH^+ + H^\bullet \quad \text{..... (1)}$$

$$ArH^+ + e^- \longrightarrow Ar^* + H^\bullet \quad \text{..... (2)}$$

$$Ar^* + H_2 \longrightarrow Ar + 2H^* \quad \text{..... (3)}$$

$$2H^* \longrightarrow 2H^\bullet \quad \text{..... (4)}$$

It is a series of chain reaction happening during the plasma reaction and is not only limited to the combination of Ar and H_2 since, H_2 alone can be able to produce $H^\bullet$ under plasma environment [79]. It is well known that GO nanosheets possess both sp^2 domains and sp^3 domains in which the former represents the unoxidized region while the later is due to oxidized region. The interaction between the produced atomic hydrogen in the plasma environment with the oxygen containing functional groups in GO and results in the formation of graphene nanosheets by the removal of sp^3 domains. This is in agreement with the previous findings of Lee *et al* [80].

3.6.2 Surface morphology and spectroscopic analysis

Figure 3.39 (a) showed the high resolution transmission electron microscopic image of the synthesized graphene nanosheet. It represents the sheets like morphology of graphene nanosheets with one or two layers. In order to study the structural changes occurred in graphene after the reduction reaction, we examined Raman spectra of GO before and after the reduction reaction and is shown in Figure 3.39 (b). The Raman spectra of GO

shows the presence of G band at 1597 cm^{-1} due to the oxygenation of graphite. In addition to this, a broadened D peak is also observed at 1350 cm^{-1} also appeared due to the reduction in size of *in plane* sp^2 domains in graphite induced by the creation of defects, vacancies and distortions of the sp^2 domains after complete oxidation [12]. After reduction the reduction reaction, the G peak is shifted towards lower wave number (1590.7 cm^{-1}) compared to that of GO. This shift was attributed to the recovery of hexagonal network of carbon atoms with defects. The D peak intensity is increased in graphene compared to that of GO suggesting that the reduction process modified the structure of GO. The intensity ratio of the D band ($I_{(D)}$) and G band ($I_{(G)}$) of GO and graphene is about 0.97 and 0.845 nm respectively. This is in agreement with the previous reports on the chemically synthesized graphene [69].

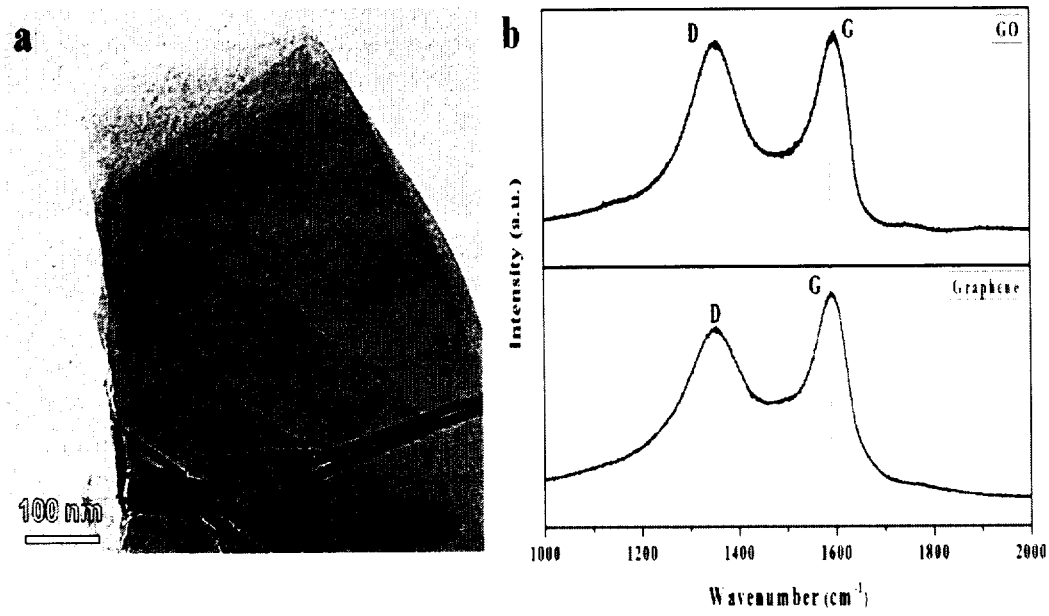

Figure 3.39 (a) HR-TEM image of graphene nanosheets. (b) Comparison of Raman spectra of GO and graphene (plasma reduction)

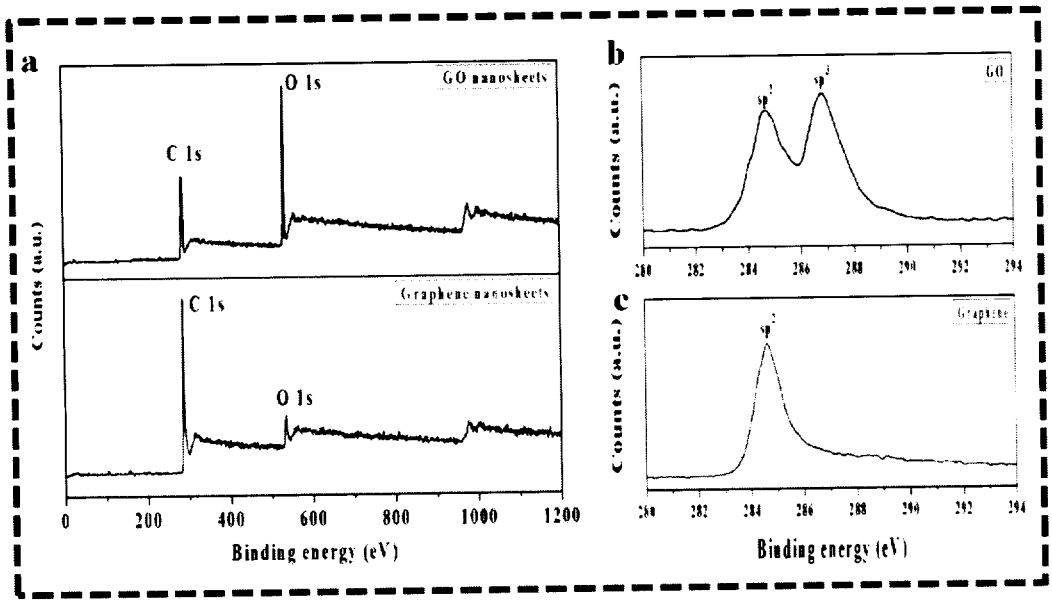

Figure 3.40 (a) XPS survey spectrum and (b) C1s of GO and (c) graphene (plasma reduction).

We also employed X-ray photoelectron spectra of GO nanosheets before and after the hydrogen plasma treatment in order to study the reduction of GO into graphene nanosheets and the about the oxygenated functional groups in GO. The XPS spectra of GO and graphene nanosheets is presented in Figure 3.40 (a). The XPS of GO exhibit the presence of peaks corresponding to both sp^2 domains (284.5 eV) and sp^3 domains (286-289 eV). The sp^3 domains present in GO represents the presence of various oxygenated functional groups such as hydroxyl, epoxyl and carbonyl groups respectively [8]. After plasma assisted reduction, the XPS of the resulting graphene sheets shows significant changes in the levels of oxygenated functional groups which are clearly evidenced from Figure 3.40 (b). It shows a dramatic decrease in the sp^3 domains as compared to GO nanosheets (as seen from Figure 3.40(c)) signifying the reduction reaction altered the electronic states of graphene by the re-graphitization process. Further, the C/O ratio of the GO and graphene nanosheets calculated from

the XPS are 6.2 and 2.6 respectively. The obtained C/O ratio of graphene synthesized by plasma method is in close agreement with the graphene nanosheets synthesized by chemical reduction methods [81].

In this study, graphene nanosheets are synthesized by the low temperature, cost effective, plasma assisted reduction method. The mechanism of the reduction of GO into graphene nanosheets is discussed in detail. The physic-chemical characterization suggested that the reduction of GO into graphene was achieved using hydrogen plasma treatment.

3.7 Conclusion

In this chapter, we studied the physico-chemical characterization of the graphene based materials with synthetic different routes viz.

- Section 3.1 shows the physico-chemical characterization GO nanosheets are synthesized using Hummers method.
- Section 3.2 demonstrated the tunable properties of GO by varying the oxidation level. A detailed spectroscopic study using Raman and XPS analysis is provided. The various oxidation level significantly altered the electrochemical properties of GO.
- Section 3.3 demonstrated a fast and facile method for the reduction of GO into graphene nanosheets
- Section 3.4 showed the hydrothermal reduction of GO into graphene and their spectroscopic and morphological characterization
- Section 3.5 demonstrated the photoluminescence quenching in graphene after reduction by galactose.
- Section 3.6 demonstrated the hydrogen plasma assisted reduction of GO into graphene using a dielectric barrier plasma reactor.

REFERENCES

[1] J. Ito, J. Nakamura, and A. Natori, J. Appl. Phys. **103**, 113712 (2008).

[2] L. Zhang, X. Li, Y. Huang, Y. Ma, X. Wan, and Y. Chen, Carbon **48**, 2367 (2010).

[3] Q. Du, M. Zheng, L. Zhang, Y. Wang, J. Chen, L. Xue, W. Dai, G. Ji, and J. Cao, Electrochim. Acta **55**, 3897 (2010).

[4] N. R. Wilson, P. A. Pandey, R. Beanland, R. J. Young, I. A. Kinloch, L. Gong, ACS Nano **3,** 2547 (2009)

[5] Y. Si and E. T. Samulski, Nano Lett. **8**, 1679 (2008).

[6] J. I. Paredes, S. V. Rodil, A. M. Alonso, and J. M. D. Tascon, Langmuir **24,** 10560 (2008).

[7] V. H. Pham, T. V. Cuong, S. H. Hur, E. Oh, E. J. Kim, E. W. Shin, and J. S. Chung, J. Mater. Chem. **21**, 3371 (2011).

[8] E. C. Salas, Z. Sun, A. Luttge, and J. M. Tour, *ACS Nano.* **4,** 4852 (2010).

[9] F. Tuinstra, and J. L. Koenig, *J. Chem. Phys.* **53,** 1126 (1970).

[10] G. Venugopal, M-H. Jung, M. Suemitsu, and S.-J. Kim, *Carbon.* **49,** 2766 (2011).

[11] K. S. Vasu, B. Chakraborty, S. Sampath and A. K. Sood, *Solid State Comm.* **150,** 1295 (2010).

[12] S. Stankovich, D. A. Dikin, R. D. Piner, K. A. Kohlhaas, A. Kleinhammes, Y. Jia Y, Y. Wu, S. T. Nguyen and R. S. Ruoff, *Carbon.* **45,** 1558 (2007).

[13] C. Zhu, S. Guo, Y. Fang and S. Dong, *ACS Nano.* **4,** 2429, (2010).

[14] M. A. Pimenta, G. Dresselhaus, M. S. Dresselhaus, L. G. Cancado, A. Jorio, and R. Saitoe, Phys. Chem. Chem. Phys. **9,** 1276 (2007).

[15] Z. Luo, P. M. Vora, E. J. Mele, A. T. C. Johnson, and J. M. Kikkawa, Appl. Phys. Lett. **94**, 111909 (2009).

[16] S. Saxena, T. A. Tyson, and E. Negusse, J. Phys. Chem. Lett. **1,** 3433 (2010).

[17] S. Shukla and S. Saxena, Appl. Phys. Lett. **98**, 073104 (2011).

[18] H. K. Jeong, M. H. Jin, K. P. So, S. C. Lim, and Y. H. Lee, J. Phys. D. Appl. Phys. **42**, 065418 (2009).

[19] H. K. Jeong, Y. P. Lee, R. J. W. E. Lahaye, M. H. Park, K. H. An, I. J. Kim, C. W. Yang, C. Y. Park, R. S. Ruoff, and Y. H. Lee, J. Am. Chem. Soc. **130,** 1362 (2008).

[20] G. Wang, X. Sun, C. Li, and J. Lian, Appl. Phys. Lett. **99**, 053114 (2011).

[21] D. C. Marcano, D. V. Kosynkin, J. M. Berlin, A. Sinitskii, Z. Sun, A. Slesarev, L. B. Alemany, W. Lu, and J. M. Tour. ACS Nano **4,** 4806 (2010).

[22] C. H. Lucas, A. J. L. Peinado, D. L. Gonzalez, M. L. R. Cervantes, and R. M. M. Aranda, Carbon **33**, 1585 (1995).

[23] N. R. Wilson, P. A. Pandey, R. Beanland, R. J. Young, I. A. Kinloch, L. Gong, Z. Liu, K. Suenaga, J. P. Rourke, S. J. York, and J. Sloan, ACS Nano **3,** 2547 (2009).

[24] F. A. Cruz, and J. M. Cowley, Nature **196**, 468 (1962).

[25] F. A. Cruz, and J. M. Cowley, Acta. Crystallogr. **16**, 531 (1963).

[26] S. Shukla, and S. Saxena, Appl. Phys. Lett. **98**, 073104 (2011).

[27] F. Bonaccorso, Z. Sun, T. Hasan, and A. C. Ferrari, Nature. Photon. **4,** 611 (2010).

[28] K. Krishnamoorthy, M. Veerapandian, R. Mohan, S. J. Kim, Appl. Phys. A. **106**, 501 (2012).

[29] D. W. Lee, and J. W. Seo, J. Phys. Chem. C. **115**, 2705 (2011).

[30] S. Dash, S. Patel, and B. K. Mishra, Tetrahedron **65**, 707 (2009).

[31] M. Tromel, and M. Russ, Angew. Chem. Int. Ed. Eng. **26**, 1007 (1987).

[32] T. Y. Kim, H. W. Lee, M. Stoller, D. R. Dreyer, C. W. Bielawski, R. S. Ruoff, and K. S. Suh, ACS Nano **5**, 436 (2011).

[33] A. S. Dukhin, P. J. Goetz. Ultrasound for characterizing colloids: Particle sizing, Zeta potential and Rheology. Elsevier; 2002.

[34] H. Ohshima, Theory of Colloid and Interfacial Electric Phenomena. New York: Elsevier; 2006.

[35] M. Lotya, Y. Hernandez, P. J. King, R. J. Smith, V. Nicolosi, L. S. Karlsson, F. M. Blighe, S. De, Z. Wang, I. T. McGovern, G. S. Duesberg, and J. N. Coleman, J. Am. Chem. Soc. **131,** 3611 (2009).

[36] I. Jung, D. A. Dikin, R. D. Piner, and R. S. Ruoff, Nano. Lett. **8**, 4283 (2008).

[37] Zeta Potential of Colloids in Water and Waste Water, ASTM Standard D 4187–82, American Society for Testing and Materials, 1985.

[38] K. S. Vasu, B. Chakraborty, S. Sampath, and A. K. Sood, Solid. State. Comm. **150**, 1295 (2010).

[39] M. A. Pimenta, G. Dresselhaus, M. S. Dresselhaus, L. G. Cancado, A. Jorio, and R. Saitoe, Phys. Chem. Chem. Phys. **9**, 1276 (2007).

[40] A. C. Ferrari, and J. Robertson, Phys. Rev. B. **61**, 14095 (2000).

[41] F. Tuinstra, J. L. Koenig, J. Chem. Phys. **53,** 1126 (1970).

[42] D. S. Knight, and W. White, J. Mater. Res. **4**, 385 (1989).

[43] L. G. Cancado, K. Takai, T. Enoki, M. Endo, Y. A. Kim, H. Mizusaki, et al. General equation for the determination of the crystallite size L_a of nanographite by Raman spectroscopy. Appl. Phys. Lett. **88,** 163106 (2006).

[44] S. Wang, R. Wang, X. Liu, X. Wang, D. Zhang, Y. Guo, and X. Qiu, J. Phys. Chem. C. **116,** 10702 (2012).

[45] B. Xu , S. Yue, Z. Sui, X. Zhang, S. Hou, G. Cao, et al. What is the choice for supercapacitors: graphene or graphene oxide? Energy. Environ. Sci. **4,** 2826 (2011).

[46] H. L. Guo, X. F. Wang, Q. Y. Qian, F. B. Wang, and X. H. Xia, ACS Nano **3**, 2653 (2009).

[47] J. Zhang, H. Yang, G. Shen, P. Cheng, J. Zhang, and S. Guo, Chem. Commun. **46,** 1112 (2010).

[48] A. Gedanken, Ultrason. Sonochem. **11,** 47 (2004).

[49] M. Veerapandian, R. Subbiah, G. S. Lim, S.-H. Park, K. S. Yun, and M. H. Lee, Langmuir **27,** 8934 (2011).

[50] C. Deng, H. Hub, X. Ge, C. Han, D. Zhao, and G. Shao, Ultrason. Sonochem. **18,** 932 (2011).

[51] D. R. Dreyer, S. Park, C. W. Bielawski, and R. S. Ruoff, Chem. Soc. Rev. **39,** 228 (2010).

[52] V. Singh, D. Joung, L. Zhai, S. Das, S.I. Khondaker, and S. Seal, Prog. Mater. Sci. **56,** 1178 (2011).

[53] W. Yang , E. Widenkvist , U. Jansson, and H. Grennberg, New J. Chem. **35,** 780 (2011).

[54] Y. Yang, L. Ren, C. Zhang, S. Huang, and T. Liu, ACS Appl. Mater. Interfaces **3,** 2779 (2011).

[55] A. Ramadoss, and S. J. Kim, J. Alloy Compd. **544,** 115 (2012).

[56] X. Fan, W. Peng, Y. Li, X. Li, S. Wang, G. Zhang, and F. Zhang, Adv. Mater. **20,** 4490 (2008).

[57] M.C. Kim, G.S. Hwang, and R.S. Ruoff, J. Chem. Phys. **131,** 064704 (2009).

[58] S. Stankovich, D.A. Dikin, R.D. Piner, K.A. Kohlhaas, A. Kleinhammes, Y. Jia, Y. Wu, S.T. Nguyen, and R.S. Ruoff, Carbon **45,** 1558 (2007).

[59] K. Vinodgopal, B. Neppolian, I. V. Lightcap, F. Grieser, M. Ashokkumar, and P. V. Kamat, J. Phys. Chem. Lett. **1,** 1987 (2010).

[60] L. Zhang, J. Liang, Y. Huang, Y. Ma, Y. Wang, and Y. Chen, Carbon **47,** 3365 (2009).

[61] A. Mathkar, D. Tozier, P. Cox, P. Ong, C. Galande, K. Balakrishnan, A. L. Reddy, and P. M. Ajayan, J. Phys. Chem. Lett. **3,** 986 (2012).

[62] H. Kim, A. A. Abdala, and C. W. Macosko, Macromolecules, **43,** 6515 (2010).

[63] N. R. Wilson, P. A. Pandey, R. Beanland, R. J. Young, I. A. Kinloch, L. Gong, Z. Liu, K. Suenaga, J. P. Rourke, S. J. York, and J. Sloan, ACS Nano **3,** 2547 (2012).

[64] S. Uhm, N.H. Tuyen, and J. Lee, Electrochem. Comm. **13,** 677 (2011).

[65] P. G. Ren, D. X. Yan, X. Ji, T. Chen, and Z. M. Li, Nanotechnology **22,** 055705 (2011).

[66] Y. Zhou, Q. Bao, L. A. L. Tang, Y. Zhong, and K. P. Loh, Chem. Mater. **21,** 2950 (2009).

[67] J. Zhang, H. Yang, G. Shen, P. Cheng, J. Zhang, and S. Guo, Chem. Comm. **46,** 1112 (2010).

[68] C. Zhu, S. Guo, Y. Fang, and S. Dong, ACS Nano **4,** 2429 (2010).

[69] J. Gao, F. Liu, Y. Liu, N. Ma, Z. Wang, and X. Zhang, Chem. Mater. **22,** 2213 (2010).

[70] X. Zhou, J. Zhang, H. Wu, H. Yang, J. Zhang, and S. Guo, J. Phys. Chem. C **115,** 11957 (2011).

[71] C. Fang, N. Bhattarai, C. Sun, and M. Zhang, Small. **5,** 1637 (2009).

[72] S. Yang, X. Feng, S. Ivanovici, and K. Mullen, Angew. Chem. Int. Ed. **49,** 8408 (2010).

[73] M. Lotya, Y. Hernandez, P. J. King, R. J. Smith, V. Nicolosi, L. S. Karlsson, F. M. Blighe, S. De, Z. Wang, I. T. McGovern, G. S. Duesberg, and J. N. Coleman, J. Am. Chem. Soc. **131,** 3611 (2009).

[74] H. R. Byon, S. W. Lee, S. Chen, P. T. Hammond, and Y. S. Horn, Carbon **49,** 457 (2011).

[75] K. N. Kudin, B. Ozbas, H. C. Schniepp, R. K. Prudhomme, I. A. Aksay, and R. Car, Nano Lett. **8**, 36 (2007).

[76] F. Bonaccorso, Z. Sun, T. Hasan, and A. C. Ferrari, Nature Photonics. **4**, 611 (2010).

[77] Z. Luo, P. M. Vora, E. J. Mele, A. T. C. Johnson, and J. M. Kikkawa, Appl. Phys. Lett. **94,** 111909 (2009).

[78] M. Li, N. Tang, W. Ren, H. Cheng, W. Wu, W. Zhong, and Y. Du, Appl. Phys. Lett. **100,** 233112 (2012)

[79] N. Mayo, U. Carmi, I. Rosenthal, R. Avni, R. Manory, and A. Grill, J. Appl. Phys. **55,** 4404 (1984).

[80] S. W. Lee, C. Mattevi, M. Chhowalla, and R. M. Sankaran, J. Phys. Chem. Lett. **3,** 772 (2012).

[81] K. Krishnamoorthy, M. Veerapandian, L. H. Zhang, K. Yun, and S. J. Kim, Journ. Phys. Chem. C. **116,** 17280 (2012).

Chapter 4

Graphene oxide and graphene nanosheets – Applications

This chapter provides detailed studies on the applications of GO and graphene nanosheets in various disciplines.

(1) Graphene oxide nanosheets are evaluated or their photocatalytic activity by the measuring the photoreduction of resazurin (RZ) in to resorufin (RF) under UV light.

(2) The antibacterial activity of GO nanosheets is evaluated against Gram negative and Gram positive bacteria. The surface modified textiles using GO also showed bacterial toxicity. These studies suggested the biomedical applications of GO towards the prevention of health care associated infection.

(3) GO nanosheets are examined for their application in corrosion inhibition of metal. Thin films of GO nanosheets are coated on to copper foil and electrochemical tests such as Tafel analysis and Electrochemical impedance spectra shows that GO can be used for corrosion inhibition application.

(4) The graphene nanosheets synthesized by hydrothermal method are examined for their antibacterial activity against pathogenic bacteria. The results shows that the MIC values of graphene nanosheets are less in comparison with the MIC value of commercial drug kanamycin, suggesting their application as a potential antibacterial agent.

(5) The plasma synthesized graphene nanosheets are evaluated for their potential application as electrodes for supercapacitor devices.

4.1 Photocatalytic application of graphene oxide

Nanosized particles have been attracted extensively as photocatalysts for the degradation of organic pollutants in water and air under ultraviolet (UV) irradiation [1]. The advantage of using nanosized particles for photocatalytic applications are mainly due to their large surface to volume ratio, high UV absorption, and effective separation of electron and hole pair [2]. The photocatalytic activity of metal oxide nanoparticles such as TiO_2, ZnO, WO_3, ZrO_2, SeO_2, and SiC are well established [3-5]. In order to increase the photocatalytic efficiency, a lot of research has been carried out by modifying the surface properties of the photocatalytic material [6,7]. Most of the photocatalytic materials are wide band gap semiconductors which motivates the researchers to seek new photocatalyst materials due to their huge impact on the environmental issues. The properties of GO such as readily dispersible in water at molecular level, biocompatibility, and tunable band gap motivated us to explore its potential as photocatalytic material. In this chapter, we studied the photocatalytic properties of GO nanosheets by evaluating the reduction in resazurin (RZ) into resorufin (RF) under UV irradiation.

In this study, GO is synthesized by the Hummers method as discussed in section. The oxidation of graphite during the preparation of graphene oxide results in the formation of graphitic islands in the graphene oxide [8]. This graphitic islands in GO is expected to produce quantum confinement effects in graphene oxide [9]. This results in the origin of band gap in electronic structure of graphene oxide. Hence, we studied the photoluminescence (PL) spectrum of GO using an excitation wavelength of 325 nm and is shown in Figure 3.8. The PL spectrum shows a sharp emission peak

in the near UV region at 365 nm due to the near band emission of GO [10]. The unusual strong emission peak in the visible range at 650 nm is not associated with GO but due to the overlap of second order emissions associated to the excitation wavelength [10].

The photocatalytic activity of GO was evaluated by measuring the photoreduction of RZ. RZ is a redox indicator used in various biological assays [11]. It is a phenoxazin-3-one dye, blue in color, having intense absorption at 600 nm and a weak absorption at 380 nm. These bands are assigned to the π-π^* transition of the phenoxazin-3-one and n-π^* transition of the N-oxide. It can be reduced into RF which has maximum absorption at 572 nm [12]. The molecular structure of Resazurin (RZ) and Resorufin (RF) is given in Figure 4.1

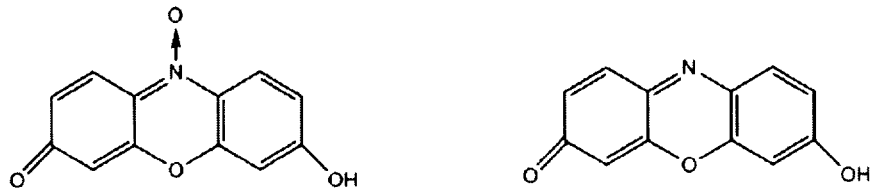

Resazurin (RZ) Resorufin (RF)

Figure 4.1 Structure of resazurin and resorufin dye molecules.

Figure 4.2 shows UV-vis spectroscopic changes occurred during the photoreduction in RZ into RF in the presence of GO (1 mg) under UV irradiation at regular time intervals. It clearly shows that upon regular time intervals of UV irradiation to the GO-RZ solution, the intensity of the RZ (absorption peak at 600 nm) decreased steadily. Simultaneously, another peak at 572 nm starts arising after UV exposure which corresponds to the formation of RF by the reduction of RZ. Figure 4.3 shows the corresponding change in intensity of RZ at 600 nm and RF at 572 nm,

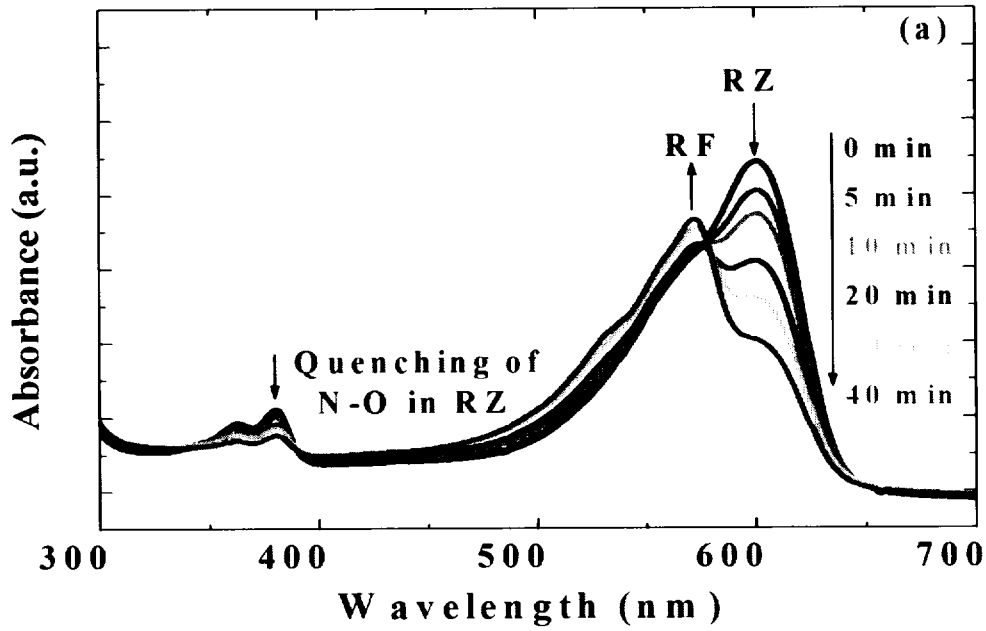

Figure 4.2 Time dependent photoreduction of RZ into RF catalyzed by GO (1mg).

This reaction was monitored by UV-vis spectroscopy.

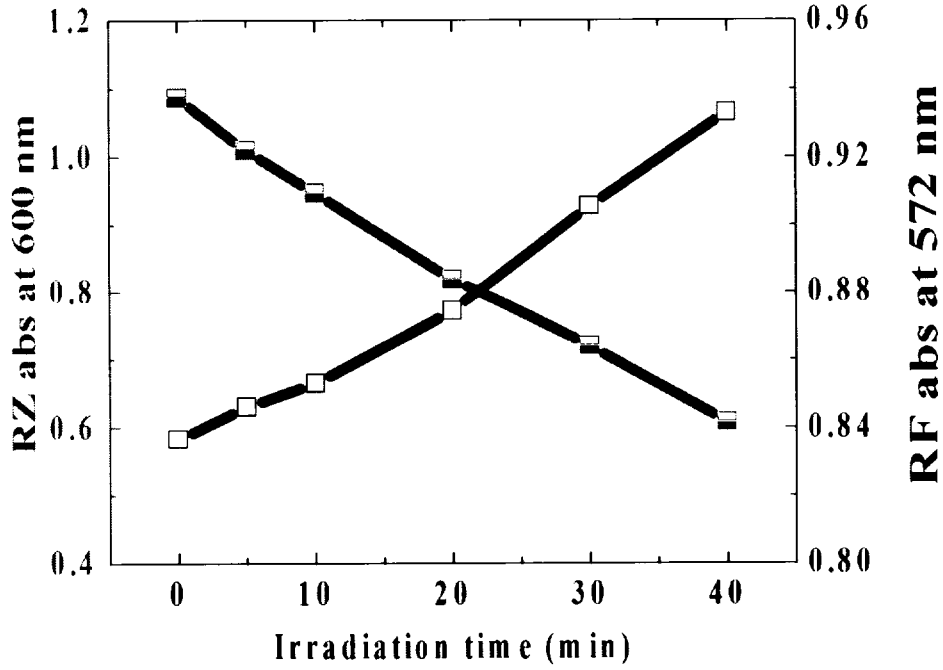

Figure 4.3 Change in intensity of RZ (600 nm) and RF (572 nm) with respect to time

respectively. In the control experiments, there is no reduction in RZ that takes place in the conditions, viz., (a) RZ with GO in the presence of visible light and (b) RZ without GO in the presence of UV irradiation. These observations confirmed that the reduction of RZ into RF occurs only in the presence of GO under UV irradiation.

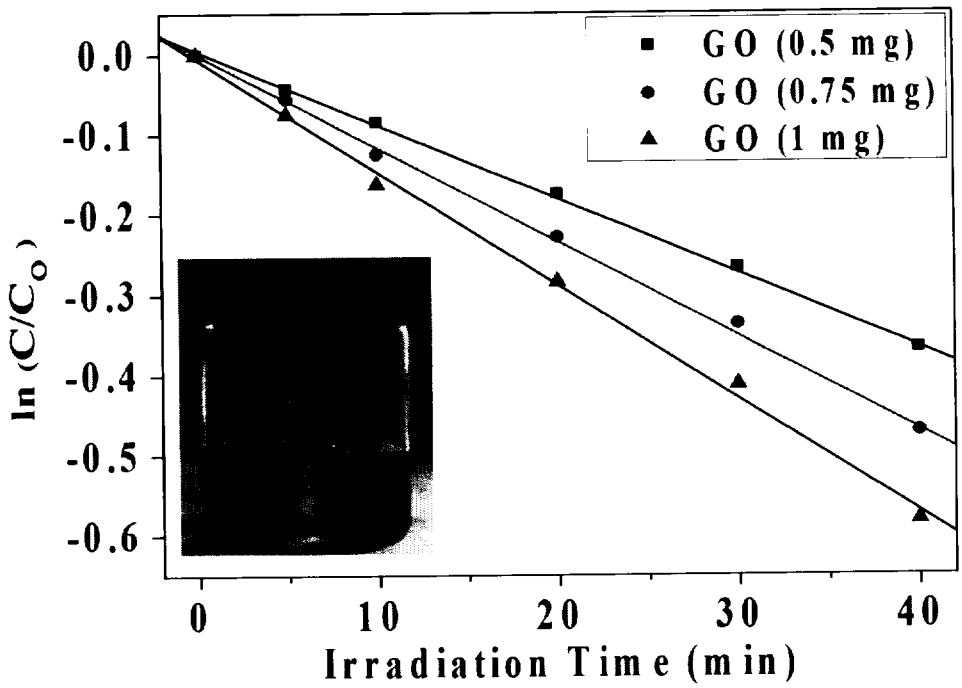

Figure 4.4 Plot of $\ln(C/C_0)$ vs irradiation time for various concentration of GO with same concentration of RZ. Inset: Photographic image of GO–RZ mixture before and after UV exposure shows the color change from blue into pink during the reduction of RZ into RF.

The reduction in the RZ molecule catalyzed by GO nanosheets fits pseudo first order reaction well, i.e., $\ln(C/C_0)=-kt$, where C is the final concentration of RZ, C_0 is the initial concentration of RZ, t is the irradiation time, and k is the apparent rate constant. Figure 4.4 shows the plot of $\ln(C/C_0)$ against the irradiated time (t) for the

various concentration of GO. In our experiment, the value of k for GO with concentration 0.5, 0.75, and 1 mg are found to be 0.0090, 0.0117, and 0.0143 min^{-1}. After 40 min of irradiation, the photocatalytic reduction percentage of RZ was measured as 34.93%, 39.09%, and 44.10% for 0.5 mg, 0.75 mg, and 1 mg concentration of GO, respectively. From these results it is clear that increasing the concentration of GO leads to increased percentage reduction in RZ into RF.

The mechanism of the photoreduction of RZ in presence of GO under UV irradiation can be described as follows:

$$GO + hv \rightarrow e- + h+ \quad \text{..... (1)}$$

$$RZ + e- \rightarrow RF \quad \text{..... (2)}$$

Since the band gap of GO was found as 3.26 eV and when it is excited with an energy gap higher than the band gap energy, the electron and hole pairs will be the generated at the surface of GO. The defect sites in GO can act as trapping center for the excited carriers and thereby hinder the recombination process. RZ molecule, which acts as an electron acceptor, readily accepts the photoexcited electrons resulting in the cleavage of the N–O bond in the RZ molecule and thereby changes the color from blue (RZ) to pink (RF) as shown in the inset of Figure 4.4 This is well supported with our results of UV-vis spectra as shown in Figure 4.2 which shows decrease in intensity in the 380 nm which is the characteristic n-π^* transition of the N-oxide of the RZ molecule.

Overall, the photoexcited electrons from the surface state of GO under UV light was responsible for the reduction of RZ. Our experimental results demonstrated that GO nanostructures have promising applications in photocatalysis.

4.2 Antibacterial activity of graphene oxide and their application in functional textiles

Human beings are often infected by microbes such as bacteria, viruses, and yeasts in the living environment. In recent years, the control of microbial population becomes a universal concern due to the ubiquity of microorganisms and their ability to establish themselves. Several bacteria exhibit multi-drug resistance against chemical antibiotic drugs for many years and they continuously emphasize on human health care [13]. The development of new antibacterial agents are of relevance to a number of industrial sectors including those focused on the environment, food, synthetic textiles, packaging, healthcare, medical care, as well as construction, and home and workplace furnishing [14]. In this regard, nanomaterials are highly recognized as antibacterial agents owing to their ability to inhibit the bacterial growth due to their size, structure, and surface properties [15]. Nanotechnology offers a way to develop potential antibacterial agents to overcome the multi-drug resistance of bacteria [16]. The application of nanotechnology to health care can be termed as "nanomedicine" which requires a combination of various disciplines including physics, chemistry, biology and medicine [17].

In this study, the antibacterial activity of GO nanosheets against both Gram negative (*E. coli*) and Gram positive (*S. iniae)* bacteria were evaluated and the mechanism of toxicity is also studied. The stability of nanomaterial in dispersion state is important prior to the biological applications [18]. Hence, we evaluated the zeta potential analysis in order to study the stability of GO in dispersion state. Figure 4.5 shows the zeta potential of GO nanosheets representing a negative zeta potential value as –46.7 mV which is mainly due to the presence of electronegative functional groups. This reveals that electrostatic repulsion between negatively charged GO nanosheets

could generate a stable aqueous suspension of them. ASTM defines colloids with zeta potentials higher than 40 mV whether it should be negative or positive to have "good stability" [19]. Hence, our dispersion of GO nanosheets shows good stability.

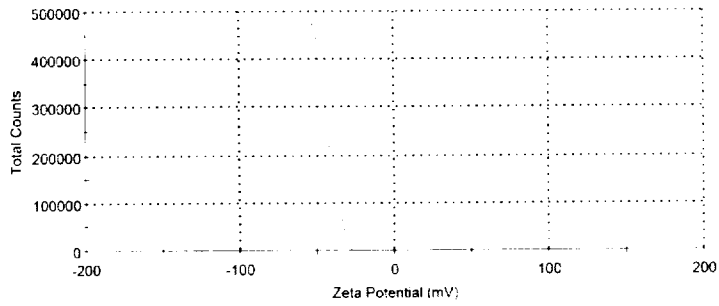

Figure 4.5 Zeta potential measurement of aqueous dispersion of GO nanosheets.

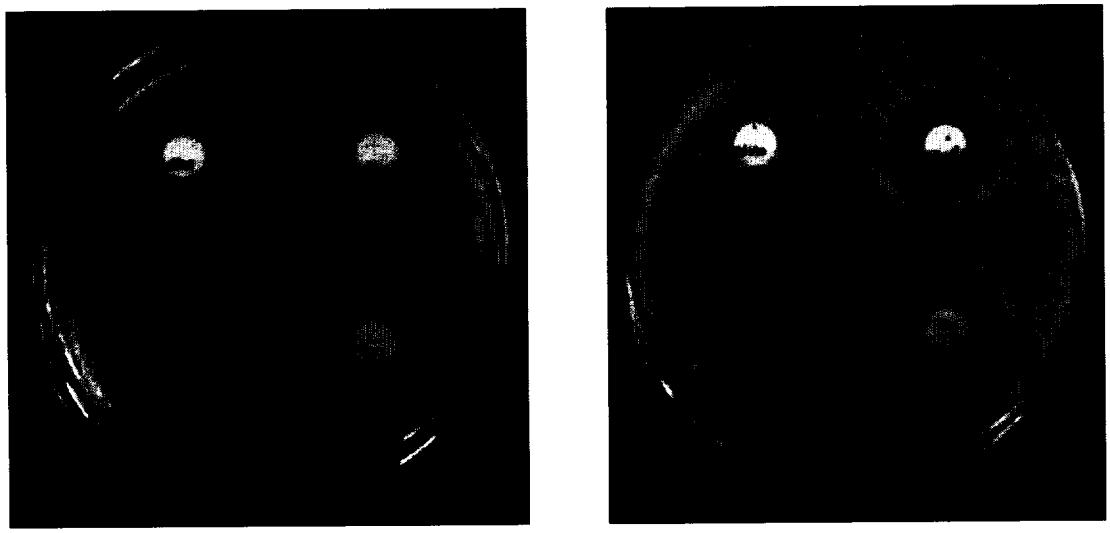

Figure 4.6 Antibacterial activity of GO nanosheets towards (a) *E. coli* and (b) *S. iniae* measured by disc diffusion method.

We examined the antibacterial activity of GO nanosheets using disc diffusion and colony counting methods. In the disc diffusion method, various concentrations of GO nanosheets are loaded into the discs and the corresponding zone of inhibition is measured. The GO nanosheets inhibited both the species with the zone of inhibition of

5 ± 0.2 mm and 8.5 ± 0.2 mm at maximum concentration of 1000 μg/mL against *E. coli* and *S. iniae* respectively as shown in Figure 4.6.

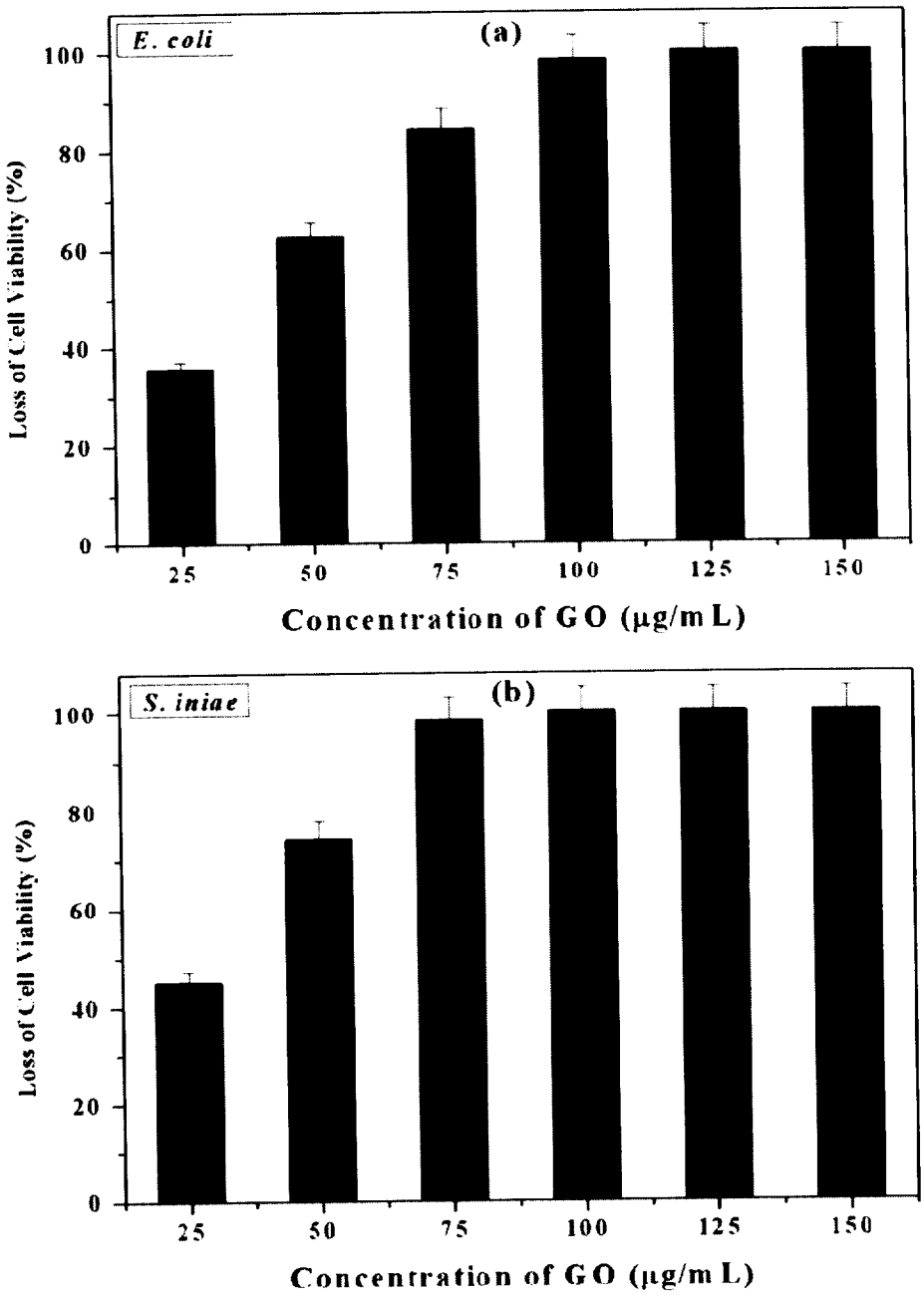

Figure. 4.7 Antibacterial activity of GO nanosheets towards (a) *E. coli* and (b) *S. iniae* by colony counting method.

Figure 4.7 shows the antibacterial activity of the GO nanosheets against *E.coli* and *S. iniae* investigated by colony counting method. The results of colony counting method showed that GO inhibited the growth of both bacterial species in a concentration dependent manner. The EC_{50} value was measured as 38 μg/mL and 29 μg /mL against *E.coli* and *S. iniae*, respectively. There are two types of antibacterials viz. bacteriostatic, which prevents the growth of bacteria without killing, and bacteriocidal which kills the bacteria. Colony counting method confirmed the bacteriocidal property of GO, where it completely inhibited the growth of *E.coli* and *S. iniae* at the concentrations of 100 μg/mL and 125 μg/mL, respectively.

4.3.2 Lipid peroxidation measurement

There are several mechanisms proposed for the antibacterial activity of nanomaterials such as direct contact mechanism and oxidative stress. Hu *et al* reported the antibacterial activity of the graphene and graphene oxide towards the *E.coli*. and loss of cellular integrity due to physical disruption or oxidative stress [20]. Akhavan *et al* demonstrated the antibacterial activity of graphene and graphene oxide nanowalls deposited on stainless steel substrates [21]. Previous study on the antibacterial activity of graphite oxide exhibited no toxicity towards bacterial species when evaluated using disc diffusion method and remarkable toxicity was observed while examined using colony counting method [22]. However, the mechanism governing the antibacterial activity of GO is not yet explored. Reactive oxygen species (ROS) are probably familiar in biology due to their ability to cause oxidative stress [23]. In order to study the role of ROS in the antibacterial activity of GO nanosheets, lipid peroxidation measurements were performed. In comparison with the control group, lipid peroxidation was increased by 129% and 116% after exposure to 20 μg/mL and 10 μg/mL of GO nanosheets, respectively. Our earlier study

demonstrated that lipid peroxidation is enhanced by free ZnO nanoparticles [11]. This evidence partly proves the involvement of free radicals in the reaction process. GO nanosheets enhanced ultrasound-induced lipid peroxidation and thus evidences the role of reactive oxygen species on the antibacterial property of GO. The produced ROS will attack the carbonyl groups present in the peptide linkages of the bacterial cell wall and thus leading to the destruction of the bacteria [24]. This is in agreement with the recent experimental finding on the ROS mediated toxicity of graphene and GO nanosheets on cellular systems [25].

4.3.3 Surface modification of textiles using GO nanosheets:

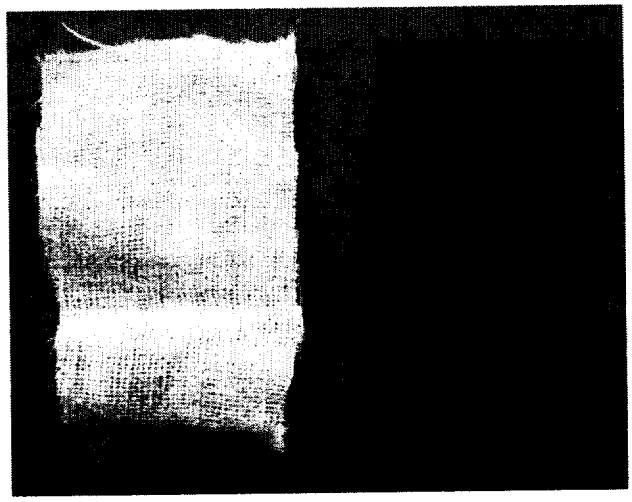

Figure 4.8 Digital images of bare textile and GO modified textile.

The GO nanosheets are coated into the textiles using dip coating process. GO is an attractive material with exceptional properties such as its high stability in aqueous solution, highly electronegative, molecular level dispersion in water etc., allows it to adhere on the surface of the textiles very rapidly. The amount of GO coated onto the textiles calculated as 0.025 g using the weight method. The GO retains on the textile surfaces even after 20 washing cycles. The photographic image of GO coated textiles is shown in Figure 4.8. The white color of the textiles changed

into blackish brown colour after GO coating confirms that GO is uniformly coated on the textiles.

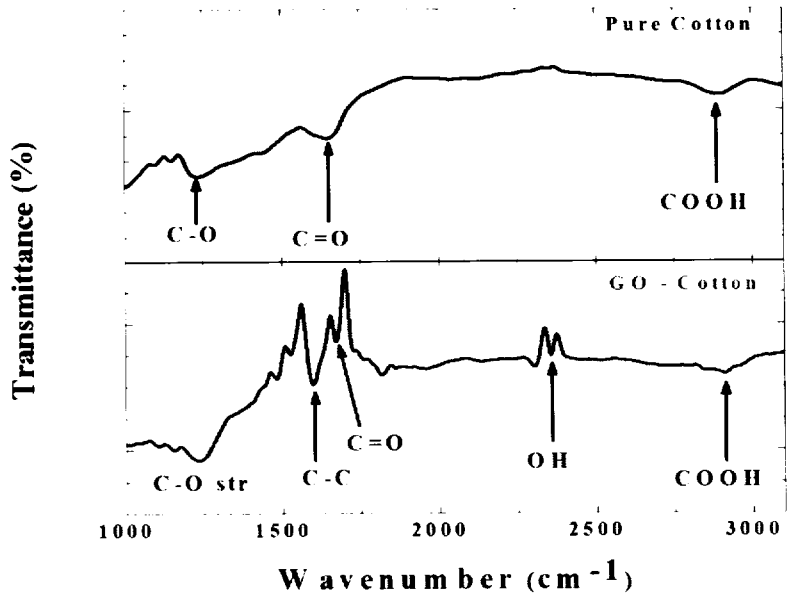

Figure 4.9 FT-IR spectra of pure textiles and GO modified textile.

The mechanism of the adhesion of GO on the surface of textile is described as follows: GO have various functional groups such as carboxyl, carbonyl, hydroxyl, and epoxyl groups make them hydrophilic nature. The hydrophilicity of GO allows them to be readily soluble in water at molecular levels with high surface capacity for adsorption which results in adhere strongly into the surface of textiles during the reaction time. This strong adhesion of GO into the surface of the textiles is confirmed from FTIR spectroscopy of control and GO-treated textiles as shown in Figure 4.9. The FTIR spectra of untreated textile exhibits the vibrational modes of C=O stretching, C-O stretching and O-H deformation mode in the region of 1200 cm^{-1} to 1700 cm^{-1} [26]. The presence of the trace amount of HO-C=O shows peak in the 2800 cm^{-1} region. The FTIR spectra of GO coated textile shows significant changes compared to the free textile. The FTIR of GO coated textile shows the presence of C-

C stretching mode at 1600 cm^{-1} proves that the textile surface is modified by GO nanosheets. The usual carboxyl peak at 1651 cm^{-1} in the textile is shifted towards the higher wavenumber at 1671cm^{-1} after GO is coated. And also the appearance of new peak at 2300 cm^{-1} is due to the O-H stretching modes of vibration which formed as a result of binding of O-H group present in the GO with the textiles. These changes occurred ensure that GO is attached onto the surfaces of textiles successfully.

4.3.4 Antibacterial properties of GO modified textiles:

Antimicrobial textiles are of potential interest in order to control the growth and transfer of bacteria since textiles can provide suitable substrates for the growth of micro-organisms [27]. The major problem in health care especially in hospitals is the transmission of bacteria and pathogens from the patients to the workers and vice versa through the textiles used by them. The increasing concern towards health care has been a motivating factor for the production of antimicrobial textiles towards its direct applications in the environment safety and human health care applications [28]. Several nanoparticles such as Ag, Au, ZnO, TiO_2, CuO etc., exhibited antibacterial activity and they are effectively reinforced into textiles for the development of antimicrobial textiles [29]. The nanoparticles can be effectively reinforced to the textiles by several surface modification process such as dip coating, sonochemical method, sol-gel method, chemical reduction method, pad-dry-cure method, etc [30].

The antibacterial activity of GO modified textile was examined against Gram-negative bacteria *(Escherchia coli DH5α)* and Gram-negative bacteria *(Streptococcus iniae)* are shown in Figure 4.10. The quantitative bacterial reduction test was performed using modified Hohenstein method for the antibacterial efficacy of the GO modified textile [28]. The experimental results revealed the time dependent reduction of bacterial growth when exposed to GO coated textile.

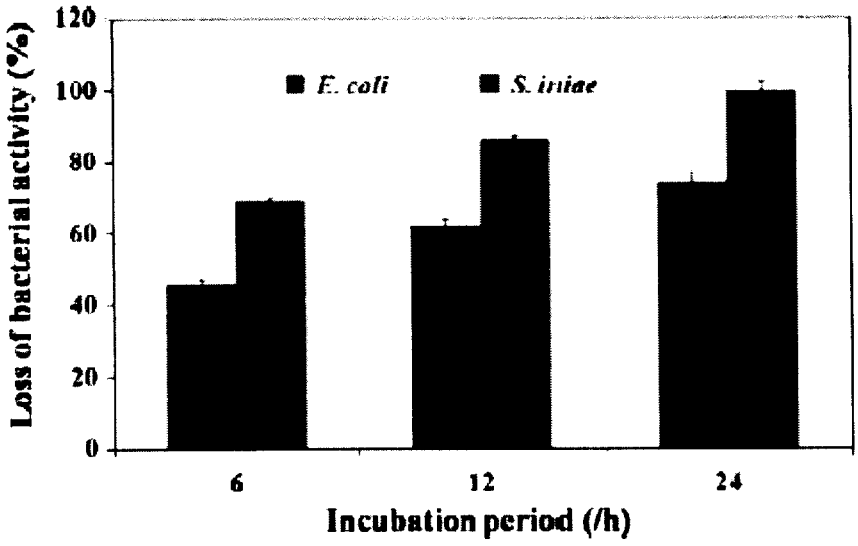

Figure. 4.10 Antibacterial activity of GO-coated textile towards *E. coli* and *S. iniae.*

The percentage reduction of Gram-negative bacteria and Gram-positive bacteria after 6, 12, 24 h exposure with GO coated cotton fabrics are 46, 62, 74 % and 68, 86, 100 % respectively. It shows that GO modified textiles are more effective towards the Gram-positive bacteria than the Gram-negative bacteria. This is in agreement with the antibacterial activity of GO nanosheets studied above. The observed differential toxicity is due to many factors such as the primary difference between the Gram-negative and Gram-positive bacteria with respect to the nature of their cell wall [31]. In addition to this, the Gram-negative bacteria possess an additional outer membrane comprising of lipopolysaccharide which protects the peptidoglycon layer from chemical attacks [32]. It is significant to mention that nanoparticle mediated toxicity towards bacterial species not only relies on the bacterial structure but also depends on several factors including the enzymatic activity [4].

These studies suggested the biomedical applications of GO nanosheets for the prevention of health care associated infections.

4.3 Corrosion inhibition applications of GO thin films

In this study, the GO films were coated on to the copper foils in order to evaluate the corrosion inhibition behavior of GO nanosheets. The protection of refined metals from the reactive environments is of significant relevance in many industrial applications [33]. There are several approaches available for the protection of metals from the corrosive media by introducing a stable protection layer of inert metals, polymers between the metal and the corrosive media [34,35]. The increasing demand for corrosion inhibition coating motivates the researcher to develop new materials with corrosion resistant properties due to their potential impact on the industrial sectors. The exceptional properties of graphene based materials make them a suitable candidate for corrosion inhibition coating.

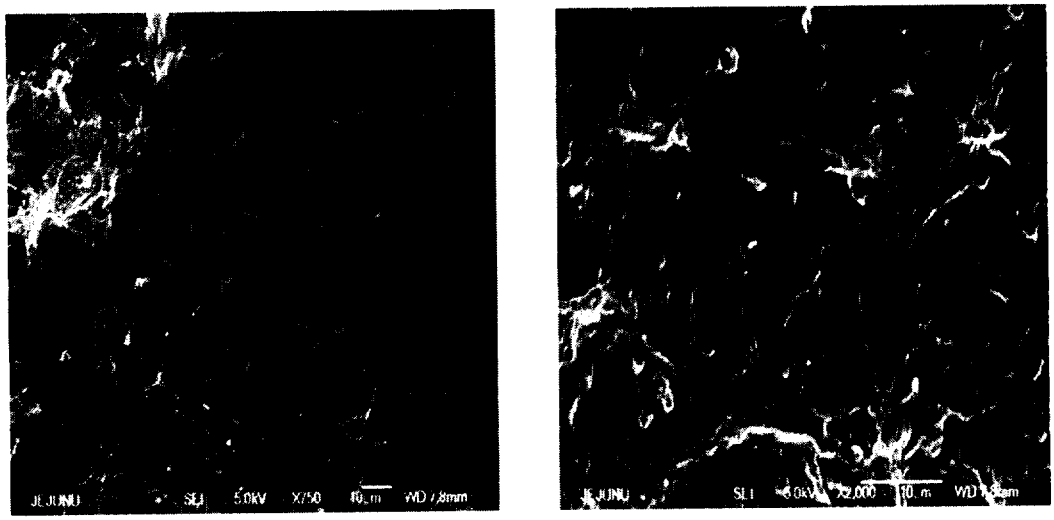

Figure. 4.11 Field emission scanning electron microscope (FE-SEM) of GO thin film deposited on copper substrates (a) low magnification and (b) high magnification.

The surface morphology of the GO thin film deposited on the copper substrate is analyzed using field emission scanning electron microscope (FE-SEM). GO

nanosheets are highly hydrophilic and can be easily dispersed in water or other solvent at molecular level [36]. Herein, the GO films are formed by drop casting of GO dispersion in water and the hydrophilic nature of GO nanosheets results in a uniform thin film on the copper substrate by self assembly after drying process [37]. Figure 4.11. shows both low and high magnification FE-SEM image of GO thin films on copper substrates which clearly revealed that a uniform thin film of GO was achieved using drop casting method.

In general, the corrosion of copper can be accompanied by two processes viz. (i) anodic oxidation and (ii) cathodic reduction which can be explained as follows [38] :

(i) Anodic oxidation:

$$Cu \rightarrow Cu^{+} + e^{-}\,(fast) \quad \text{.....(3)}$$

$$Cu^{+} \rightarrow Cu^{2+} + 2e^{-}\,(slow) \quad \text{.....(4)}$$

(ii) Cathodic reduction:

$$O_2 + H_2O + 4e^{-} \rightarrow 4OH^{-} \quad \text{.....(5)}$$

The above reactions will occur simultaneously. Thus limiting one of the reaction will results in the prevention of corrosion. The potentiodynamic polarization curve and the EIS studies were employed to analyze the corrosion inhibition properties of GO coating. The potentiodynamic polarization curves are obtained for the bare copper substrate and GO coated copper substrate in 3.5% NaCl solution are shown in Figure 4.12 The corrosion potential (E_{corr}) and the corrosion current density (I_{corr}) for bare copper substrate and GO coated copper substrate were calculated from the polarization curves by fitting the Tafel equation. The corrosion potential of the

bare copper substrate is about -269.89 mV. The E_{corr} of the GO coated copper substrates with comparison of the bare copper substrate, shows a shift towards the positive side (E_{corr}= -131.73 mV). GO coating significantly improved the corrosion resistance of the copper substrates by decreasing the I_{corr}.

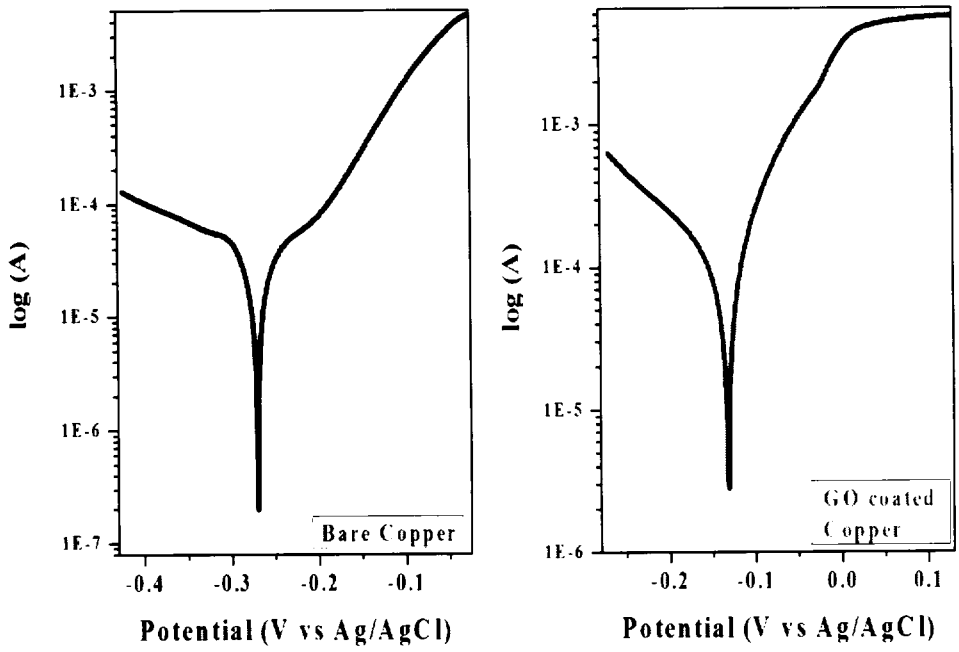

Figure 4.12 Polarization studies of bare copper and GO coated copper substrates.

In order to elucidate the mechanism of corrosion inhibition of GO thin films, we examined the electrochemical impedance spectroscopy of the bare copper substrates and GO coated copper substrates and are shown in Figure 4.13. The double layer capacitance C_{dl} value is obtained from the Nyquist plot using the equation given below [39]:

$$W\ (Z_{im}\ max) = (1/\ C_{dl})\ R_{ct} \quad \ldots\ldots\ldots\ldots\ldots\ldots\ldots\ldots\ldots\ldots\ (6)$$

where R_{ct} is the charge-transfer resistance. The R_{ct} and C_{dl} values obtained from the impedance spectroscopic data for the bare copper substrate are 2.633 Ω and 88.41 mF/cm^2. The increase in R_{ct} value (14.3171Ω) and decrease in C_{dl} value (3.37 mF/cm^2) for the GO coated copper substrates confirms the better corrosion resistance of the GO coated copper substrates compared to bare substrate. The protective efficiency $P_i(\%)$ of the GO coating is obtained from the EIS studies using the given equation [40]:

$$P_i(\%) = [1-(R_{ct} \text{ of copper substrate} / R_{ct} \text{ of GO coated substrate})] \times 100 \quad .....(7)$$

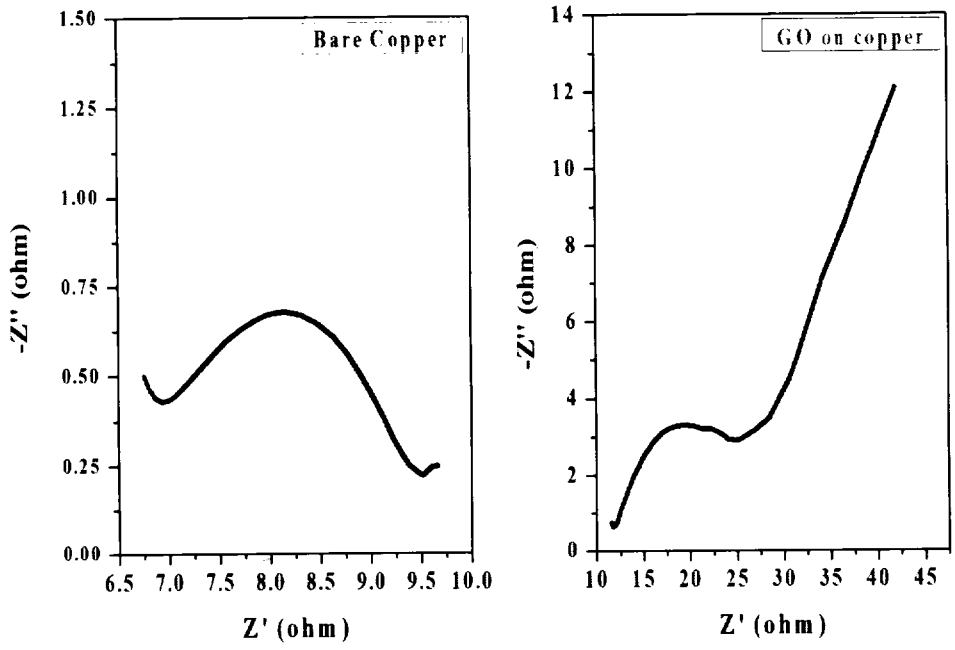

Figure 4.13 EIS studies of bare copper and GO coated copper substrates.

The calculated protective efficiency of the GO coated copper substrates shows 81 % compared to the bare copper foil indicates that GO coating act as a passivation layer to prevent the copper from the corrosive media. The mechanism of corrosion inhibition property of GO can be explained with the physico-chemical structure of GO,

since it contains different types of oxygen related functional groups such as carbonyl, carboxyl, hydroxyl and epoxyl on either side of the basal planes and also at the edges of the graphene sheets [41]. The oxygen related functional groups as evident from the FTIR and XPS data of GO makes them highly electronegative (zeta potential of GO is about -52 mV) surface which result in oxidation resistant surfaces. In our study, we tested the corrosion resistant property of GO on copper substrates in NaCl solution. The Cl^- anions present in NaCl solution is one of the most aggressive anions for the degradation or disrupt the majority of metals or alloy by the formation of salts [42]. The electrochemical polarization studies as shown in Figure 4.13 suggested that the GO coated copper substrates shows a increase in charge transfer resistance of the than the bare copper which is attributed the presence of electronegative functional groups in GO. This is due to the fact that the negatively charged functional groups in GO can effectively repel the Cl^- ions in the corrosive media through electrostatic repulsion, thereby limiting the access of electrolyte ions into the electrode surface. These results suggested that GO coating act as a protection layer for Cu by providing a diffusion pathway for the electrolyte ions in the corrosive media.

Since GO is an exceptional material when compared to other carbon based materials due its chemical structure which can be easily functionalized with other materials through covalent or non-covalent bonding, we believe that these findings might create new horizon in the development of GO based coating for improved corrosion resistance properties.

4.4 Antibacterial Efficiency of Graphene Nanosheets Against Pathogenic Bacteria

In this study, the anti-bacterial activity of graphene nanosheets synthesized by hydrothermal method (as discussed in chapter 2) was tested using a micro dilution method and the MIC values were measured against two Gram-negative strains (*E. coli* and *S. typhimurium*) and Gram-positive strains (*E. faecalis* and *B. subtilis*).

Anti-microbial properties of carbon based materials such as CNT, fullerenes, graphite oxide, and in nanocomposite forms have been looked at in previous literatures [43-45]. The general mechanism of antibacterial activity of carbon materials relies on the size, structure, composition and properties of the individual materials. In addition, nanoscale size distribution, high surface to volume ratio and other physico-chemical properties were also demonstrated to be viable factors for governing anti-microbial effects [16].

Herein, a comparative analysis was performed to evaluate the anti-bacterial property of graphene nanosheets with a standard drug, Kanamycin (aminoglycoside antibiotic). The MIC values of graphene nanosheets for both Gram-negative and Gram-positive bacteria are presented in Table 1. The MIC value of graphene against *E. coli, S. typhimuirum, B. subtilis and E. faecalis* were measured as 1, 1, 8 and 4 μg/mL, respectively. The MIC values of graphene nanosheets towards the tested bacterial species shows that it is more efficient compared with the MIC values of the standard antibiotic drug, Kanamycin. Until now, there has been no such study measuring the MIC values of graphene nanosheets towards Gram-negative and Gram-positive bacteria. Our results showed that graphene nanosheets are more toxic to Gram-negative bacteria than Gram- positive bacteria. This is in agreement with

Table 1. Minimum inhibitory concentration (MIC) of graphene nanosheets and standard drug kanamycin against Gram-negative and Gram-positive bacterial strains. (Results are mean ± standard deviation (n=3).

Bacterial strains	Graphene MIC (μg/mL)	Kanamycin MIC (μg/mL)
Gram-negative strains		
Escherichia coli	1	64
Salmonella typhimurium	1	64
Gram-positive strains		
Enterococcus faecalis	8	128
Bacillus subtilis	4	128

previous findings of Hu et al. and Akhavan et al [20,21]. Hu et al. reported that the antibacterial activity of graphene nanosheets results in the loss of cellular integrity with the disruption of cell walls of *E. coli*, which is either due to physical disruption or oxidative stress mechanism [20]. In the present study, the differential toxicity of graphene towards Gram-negative bacteria compared to Gram-positive bacteria is due to differences in the natures of their cell walls. Gram-negative bacteria possess a thin peptidoglycon layer (7-8 nm thickness) whereas Gram-positive bacteria possess a thick peptidoglycon layer (about 20 -80 nm thickness) [21].

In general, the nanomaterials toxicity against biological systems arises due to physical disruption or oxidative stress [46]. The former is due to direct contact between the nanomaterial and cellular systems while the later is due to the generation of elevated ROS levels [47]. Understanding the nano-biointerface is a key aspect to

elucidate the mechanism of cell death. Therefore, in the current study we observed the electron microscopic (FE-SEM) images of *E. coli* (as representative strain), before and after graphene exposure (see Figure.4.14). As seen in Figure 4.14 (c), the cell morphology of focused single

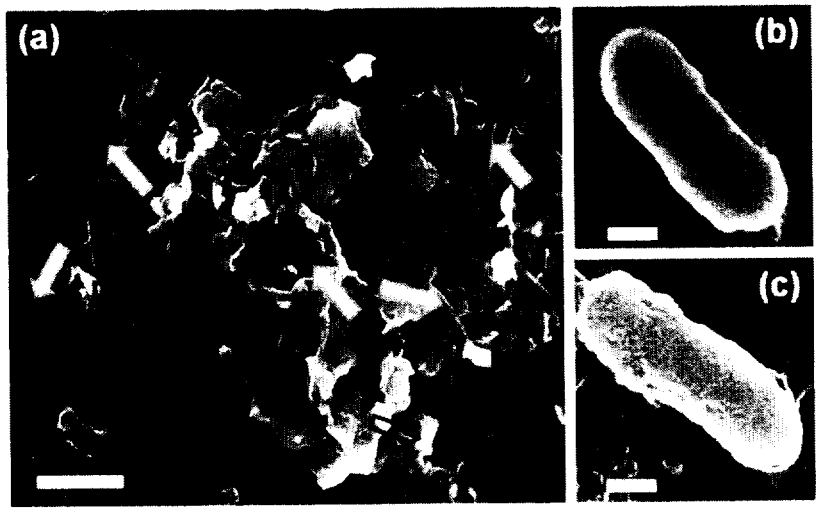

Figure 4. 14 FE-SEM image of E. coli treated with graphene nanosheets (a: scale bar = 1 μm); focused single E. coli cell before (b: scale bar = 500 nm) and after antibacterial study (c: scale bar = 500 nm). Marked arrows shows in (a) denotes the location of graphene nanosheets (black arrow) and E. coli cells (yellow arrow) between the graphene nanosheets.

E. coli cell clearly shows that the graphene sheets interaction with the bacterial surface causes the disruption of outer membrane, which leads to the cell death. This is in agreement with the previous study of Akhavan et al. in that they demonstrated the inactivation of bacteria by trapping the bacteria between the aggregated reduced graphene sheets by melatonin [48]. It should be also noted that nanomaterials toxicity towards biological species not only relies on the nature of the cell wall, but is also dependent on cellular enzymes and biochemical events. There are reports showing that carbon based materials such as CNT, fullerene cause oxidative stress in biological systems [49,50]. The free-radical modulation activity of graphene nanosheets was

determined by ultrasonic irradiation induced lipid peroxidation in liposomes from egg lecithin [11]. Ultrasonic radiation caused lipid peroxidation in the liposomal membrane which results in the detection of three reaction products: conjugated dienes, lipid hydroperoxides, and malondialdehydes in the liposomal membrane [51]. These reaction products are produced at different stages of a lipid peroxidation chain reaction mediated by free radicals. Our earlier study demonstrates that lipid peroxidation is enhanced by ZnO nanoparticles [11]. This evidence partly proves the involvement of free radicals in the reaction process [52].

Graphene nanosheets enhanced the ultrasound-induced lipid peroxidation. In comparison with the control group, lipid peroxidation was increased by 117 and 109 % after exposure to 10 and 5 μg/mL of graphene ($p < 0.05$), respectively. This illustrates the influence of ROS in the toxicity of graphene nanosheets. Evidence for over production of reactive oxygen species (ROS) and its influence on the physiological effects in plants, bacteria and mammalian cells by graphene was discussed in previous literatures [53,54]. The mechanism of cellular toxicity such as elevated ROS levels, that overwhelm the intra-cellular ROS levels causes cells to enter a state of oxidative stress which further results in damage to cellular components such as DNA, lipids and proteins [55,56]. The oxidation of fatty acids leads to the generation of lipid peroxides that stimulate a chain reaction resulting in the disintegration of a cell membrane followed by cell death [11].

Overall, our results on the antibacterial activity of graphene nanosheets show that graphene can act as a suitable antibacterial agent. Currently, we are focusing on the utilization of this material towards biomedical applications such as coating of medical instruments for future work.

4.5 Graphene nanosheets for supercapacitor applications

Supercapacitors, also known as electrochemical capacitors (ECs), have received considerable attention in recent years due to their higher power density, longer cycle life and higher energy density compared to secondary batteries and their conventional electrical double layer capacitors [57]. The mechanism of energy storage in supercapacitors is either due to electrical double layer capacitance or pseudocapacitance phenomenon [58]. The former is due to the reversible electrolyte ions adsorbed at the interface between the electrode and electrolyte, while the later arises due to the sequential redox reactions occurred at the electrode surface [59]. Until now extensive efforts has been taken in the development of supercapacitive materials such as carbon nanomaterials, metal oxide nanostructures and conducting polymers, etc [60]. Compared with the EDLCs, the pseudocapacitive materials provided higher energy densities, but their practical applications are limited due to their non-compatibility with organic electrolytes, high cost and low conductivity [61]. This led the researchers to develop new materials for supercapacitor applications with high EDLC. So far, carbon based materials have the advantage of being a promising electrode for supercapacitor applications. Many carbon materials such as activated carbon, carbon aerogels, CNTs, graphene and graphene oxide are used as high performance supercapacitor electrodes [62].

Further, the graphene nanosheets synthesized by plasma assisted reduction reaction was examined for their applications in supercapacitor devices. At first, we studied the CV curves of the graphene nanosheets with different scan rates as shown in Figure 4.15 (a). The CV curves are measured in 1M solution of KCl electrolyte at different scan rates. It is well known that CV curves of an ideal supercapacitor should be rectangular behavior depicting a lower contact resistance, whereas larger resistance

distorts the CV curve into narrowed curve [63]. The CV curves of the graphene nanosheets synthesized by plasma method shows a typical rectangular behavior with the applied scan rates ranging from 0.005 to 0.1 V/s, depicting an excellent supercapacitive behavior with low contact resistance in the supercapacitor. The CV curves with different scan rate clearly evidences that the current under curve increases with increase in scan rate, this is due to the fact that the voltammetric current is always directly proportional to the scan rate [64]. The similar type of phenomenon is well observed in the CV curves and is also in agreement with the previous reports on the CV of graphene electrodes [65]. The EIS data of the graphene electrodes are analyzed using Nyquist plots and is represented in Figure 4.15(b). The graphene electrodes shows a small arc at the higher frequency region and straight lines at low frequency region in which the former is related to the charge transfer limiting process while the later corresponds to the diffusive resistance of the electrolyte ions into the interior of the electrode and ion diffusion/transport into the electrode surface [66]. The equivalent series resistance calculated from the EIS spectra is 3.6 ohm and this lower value is attributed to the conductivity of graphene nanosheets and also the low contact resistance between the graphene nanosheets and the current collector [67].

The galvanostatic charge-discharge analysis of the graphene electrodes were studied using different current densities (0.5, 0.75, 1 mA cm^{-2}) as shown in Figure 4.15 (c) and (d). The charge-discharge curve shows almost a linear and symmetrical behavior in the total range of potential, which revealed the better capacitive behavior of the as-prepared graphene electrode. At high current densities, the charge-discharge cycle is very fast, while at a lower current density (0.5 mA cm^{-2}) a better charge-discharge cycle was achieved. This is mainly due to the fact that at lower current

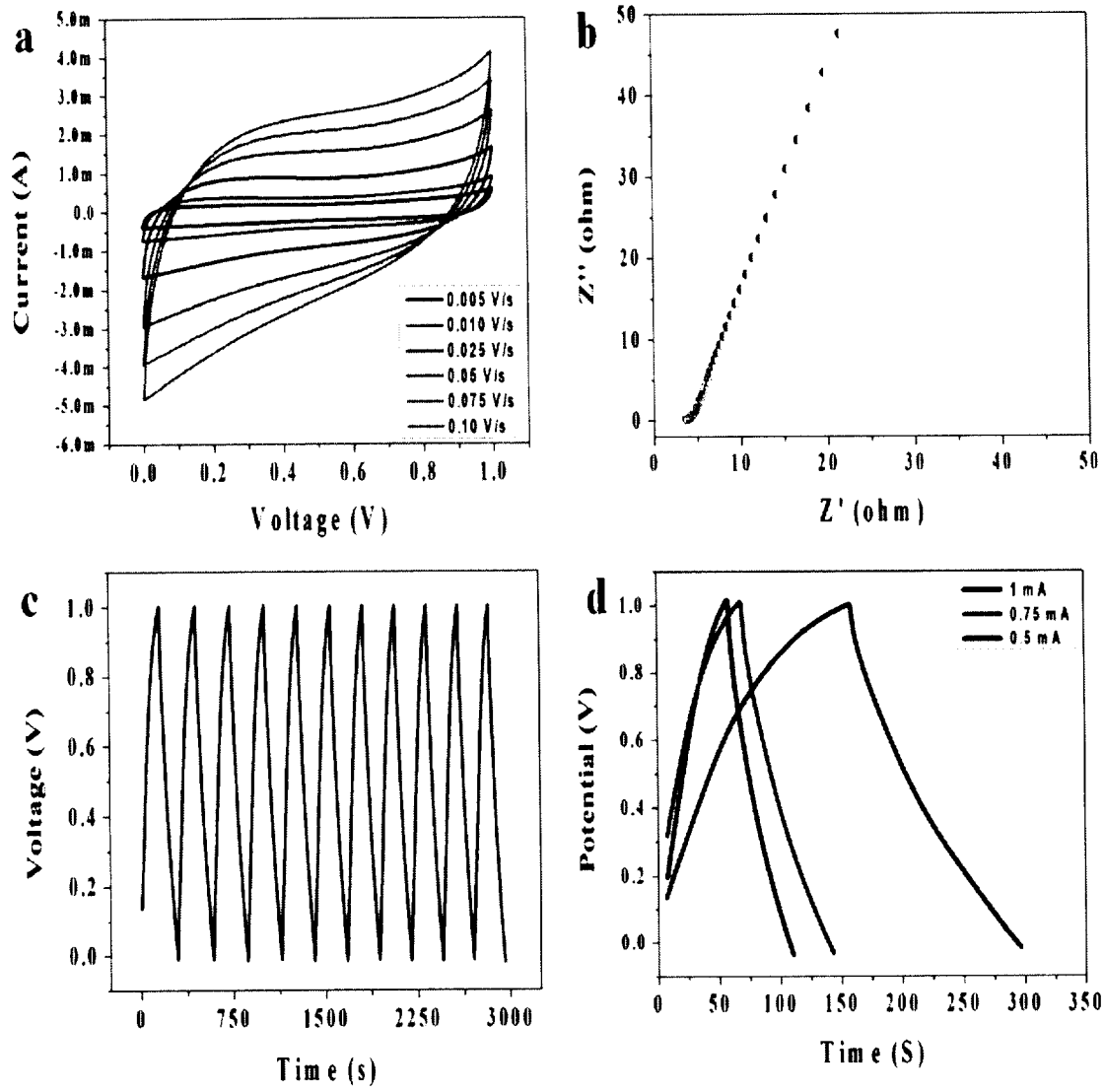

Figure. 4.15 (a) Cyclic voltammetry of graphene nanosheet electrodes in 1m KCl electrolyte. b) Electrochemical impedance spectra of graphene electrodes c) Charge discharge curve of graphene electrodes in 1M KCl with current density 0.5 mA cm^{-2} d) Charge discharge curve of graphene electrodes under different current densities.

density, a complete diffusion of the electrolyte ions has been occurred at the active electrode material. At a higher current density, the electrolyte ions possess time constraints which limits their diffusion at the active electrode, thereby results in lower

specific capacitance [68]. The specific capacitance is calculated from the galvanostatic charge-discharge analysis by using the relation:

$$C_{sp} = [(I\Delta t)/m\Delta V]\ F/g \quad \ldots\ldots\ldots\ldots\ldots\ldots\ldots\ldots\ldots\ldots\ (8)$$

where, I is the discharge current (mA), Δt is the discharge time (t), m is the mass of the electro-active material (mg), ΔV is the potential window. The maximum specific capacitance calculated is about 141 F/g under a current density 0.5 mA cm^{-2} and the capacitance retention is about 91.5 % after 1000 cycles. The achieved specific capacitance is in agreement with the previous reports on the specific capacitance of graphene nanosheets by other methods [69,71].

These studies suggest the use of graphene nanosheets towards supercapacitor applications.

4.6 Conclusion

In conclusion, the given applications of GO and graphene nanosheets are studied in this chapter as given below.

- Photocatalytic application of GO nanosheets
- Antibacterial applications of GO nanosheets and their use in functional textiles
- Corrosion inhibition application of GO thin films
- Antibacterial efficacy of graphene nanosheets (hydrothermal method) against pathogenic bacteria
- Supercapacitor application of graphene nanosheets (plasma reduced method).

REFERENCES

[1] J. Lv, T. Kako, Z. Zou, and J. Ye, Appl. Phys. Lett. **95**, 032107 (2009).

[2] Q. Wan and T. H. Wang, Appl. Phys. Lett. **87**, 083105 (2005).

[3] A. Fujishima and K. Honda, Nature (London) **238**, 37 (1972).

[4] W. Zhou, L. Yan, Y. Wang, and Y. Zhang, Appl. Phys. Lett. **89**, 013105 (2006).

[5] M. Berr, A. Vaneski, A. S. Susha, J. R. Fernandez, M. Doblinger, F. Jackel, A. L. Rogach, and J. Feldmann, Appl. Phys. Lett. **97**, 093108 (2010).

[6] R. Asahi, T. Morikawa, K. Aoki, and Y. Taga, Science **293**, 269 (2001).

[7] U. Sulaeman, S. Yin, and T. Sato, Appl. Phys. Lett. **97**, 103102 (2010).

[8] Z. Luo, P. M. Vora, E. J. Mele, A. T. C. Johnson, and J. M. Kikkawa, Appl. Phys. Lett. **94**, 111909 (2009).

[9] S. Saxena, T. A. Tyson, and E. Negusse, J. Phys. Chem. Lett. **1,** 3433 (2010).

[10] S. Shukla and S. Saxena, Appl. Phys. Lett. **98**, 073104 (2011).

[11] M. Premanathan, K. Karthikeyan, K. Jeyasubramanian, and G. Manivannan, Nanomedicine: Nanotechnol. Biol. Med. **7**, 184 (2011).

[12] G. V. Porcal, C. M. Previtali, and S. G. Bertolotti, Dyes Pigm. **80**, 206 (2009).

[13] J. S. Kim, E. Kuk, K. N. Yu, J. H. Kim, S. J. Park, H. J. Lee, S. H. Kim, Y. K. Park, Y. H. Park, C. Y. Hwang, Y. K. Kim, Y. S. Lee, D. H. Jeong, and M. H. Cho, Nanomedicine: Nanotechnol. Biol. Med. **3,** 95 (2007).

[14] A. Kumar, P. K. Vemula, P. M. Ajayan, and G. John, Nat. Mater. **7,** 236 (2008).

[15] Y. Li, P. Leung, L. Yao, Q. W. Song, and E. Newton, J. Hosp. Infect. **62,** 58 (2006).

[16] K. R. Raghupathi, R. T. Koodali, and A. C. Manna, Langmuir **27,** 4020 (2011).

[17] G. L. French, Adv. Drug. Deliv. Rev. **57,** 1514 (2005).

[18] C. Fang, N. Bhattarai, C. Sun, and M. Zhang, Small **5,** 1637 (2009).

[19] Zeta potential of colloids in water and waste water, ASTM Standard D 4187-82, American Society for Testing and Materials (1985).

[20] W. Hu, C. Peng, W. Luo, M. Lv, X. Li, D. Li, Q. Huang, and G. Fan, ACS Nano **4,** 4317 (2010).

[21] O. Akhavan and E. Ghaderi, ACS Nano **4,** 5731 (2010).

[22] N. Zhou, N. Menga, Y. Maa, X. Liao, J. Zhang, L. Li, and J. Shen, Carbon **47,** 1343 (2009).

[23] J. Lovric, S. J. Cho, F. M. Winnik, and D. Maysinger, Chem. Biol.**12,** 1227 (2005).

[24] M. Valko, H. Morris, and M. T. D. Cronin, Curr. Med. Chem.**12,** 1161 (2005).

[25] Y. Chang, S.-T. Yang, J.-H. Liu, E. Dong, Y. Wang, A. Cao, Y. Liu, and H. Wang, Toxic. Lett. **200,** 201 (2011).

[26] K. Vaideki, S. Jayakumar, G. Thilagavathi, and R. Rajendran, Appl. Surf. Sci. 253, 7323 (2007).

[27] O. C. Farokhzad and R. Langer, Adv. Drug. Deliv. Rev. **58,** 1456 (2006).

[28] R. Dastjerdi, and M. Montazer, Colloids. Surf. B. **79,** 5 (2010).

[29] T. Vigo, Text Res. J. **51,** 454 (1981).

[30] G. Fu, P. Vary, and C. T. Lin, J. Phys. Chem. B. **109,** 8889 (2005).

[31] P. Eaton, J. C. Fernandes, E. Pereira, M. E. Pintado, and F. X. Malcata, Ultramicroscopy **108,** 1128 (2008).

[32] O. Akhavan and E. Ghaderi, ACS Nano **4,** 5731 (2010).

[33] M. A. Malik, M. A. Hashim, F. Nabi, S. A. Thabaiti, and Z. Khan, Int. J. Electrochem. Sci. **6,** 1927 (2011).

[34] X. Xu, H. Liu, W. Li, and L. Zhu, Mat. Lett. **65,** 698 (2011).

[35] M. Pushpavanam, V. Raman, and B. A. Shenoi, Surf. Technol. **12,** 351 **(1981).**

[36] H. Yun, T. D. N. Phan, V. H. Pham, H. Kweon, J. S. Chung, B. Lee, and E. W. Shin, Mater. Res. Bull. **47,** 2988 (2012).

[37] D. Li, M. B. Muller, S. Gilje, R. B. Kaner, and G. G. Wallace, Nat. Nanotechnol. **3,** 101 (2008).

[38] S. Hong, W. Chen, H. Q. Luo, and N. B. Li, Corr. Sci. **57,** 270 (2012).

[39] B. Subramanian, R. Ananthakumar, and M. Jayachandran, Surf. Coat. Tech. **205,** 3485 (2011).

[40] F. Bentiss, M. Traisnel, and M. Lagrenee, Corr. Sci. **42,** 127 (2000).

[41] M. Veerapandian, M.-H. Lee, K. Krishnamoorthy, and K. S. Yun, Carbon, **50,** 4228, (2012).

[42] R. K. S. Raman, P. C. Banerjee, D. E. Lobo, H. Gullapalli, M. Sumandasa, A. Kumar, L. Choudhary, R. Tkacz, P. M. Ajayan, and M. Majumder, Carbon, **50,** 4040 (2012).

[43] L. G. Cancado, K. Takai, T. Enoki, M. Endo, Y. A. Kim, H. Mizusaki, A. Jorio, L. N. Coelho, R. M. Paniago, and M. A. Pimenta, Appl. Phys. Lett. **88,** 163106(1-3) (2006).

[44] C. Fang, N. Bhattarai, C. Sun, and M. Zhang, Small. **5,** 1637 (2009).

[45] S. Yang, X. Feng, S. Ivanovici, and K. Mullen, Angew. Chem. Int. Ed. **49,** 8408 (2010).

[46] J. Lovric, S. J. Cho, F. M. Winnik, and D. Maysinger, Chem. Biol. **12,** 1227 (2005).

[47] T. Xia, M. Kovochich, J. Brant, M. Hotze, J. Sempf, T. Oberley, C. Siloutas, J. I. Yeh, M. R. Weisner, and A. E. Nel, Nano Lett. **6,** 1794 (2006).

[48] O. Akhavan, E. Ghaderi, and A. Esfandiar, J. Phys. Chem. B **115,** 6279 (2011).

[49] Y. Zhang, S. F. Ali, E. Dervishi, Y. Xu, Z. Li, D. Casciano, and A. S. Biris, ACS Nano **4,** 3181 (**2010**).

[50] K. M. Garza, K. F. Soto, and L. E. Murr, Int. J. Nanomedicine **3,** 83 (2008).

[51] A. K. Jana, S. Agarwal, and S. N. Chatterjee, Radiat. Res. **124,** 7 (1990).

[52] Pryor WA. The involvement of free radicals in aging and carcinogenesis. In: Mathieu VJ, editor. Medicinal chemistry. Amsterdam: Elsevier; **1977,** 331-59.

[53] Y. Li, Y. Liu, Y. Fu, T. Wei, L. L. Guyader, G. Gao, R.-S. Liu, and Y.-Z. Chang, C. Chen, Biomaterials **33,** 402 (2012).

[54] S. Liu, T. H. Zeng, M. Hofmann, E. Burcombe, J. Wei, R. Jiang, J. Kong, and Y. Chen, ACS Nano **5,** 6971 **(2011).**

[55] T. C. Long, N. Saleh, R. D. Tilton, G. V. Lowry, B. Veronesi, Environ. Sci. Technol. **40,** 4346 (2006).

[56] J. Gao, F. Liu, Y. Liu, N. Ma, Z. Wang, and X. Zhang, Chem. Mater. **22,** 2213 (2010).

[57] Z. Zhou, X. F. Wu, and H. Fong, Appl. Phys. Lett. **100,** 023115(1-4) (2012).

[58] A. V. Murugan, T. Muraliganth, A. Manthiram, Chem. Mater. **21** (2009) 5004.

[59] R. Kalaiselvan, I. Genish, I. Perelshtein, J. M. C. Moreno, and A. Gedanken, J. Phys. Chem. C **112** (2008) 1825.

[60] B. Senthilkumar, P. Thenamirtham, and R. Kalai Selvan, Appl. Surf. Sci. **257,** 9063 (2011).

[61] A. V. Murugan, A. K. Viswanath, G. Campet, C. S. Gopinath, and K. Vijayamohanan, Appl. Phys. Lett. **87,** 243511(1-3) (2005).

[62] B. R. Stoner, B. R. Stoner, A. S. Raut, B. Brown, C. B. Parker, and J. T. Glass, Appl. Phys. Lett. **99** 183104(1-3) (2011).

[63] G. Guo, L. Huang, Q. Chang, L. Ji, Y. Liu, Y. Xie, W. Shi, and N. Jia, Appl. Phys. Lett. **99** (2011) 083111(1-3).

[64] S. T. Senthilkumar, S. Balaji, C. Sanjeeviraja, and R. Kalai Selvan, Mater. Res. Bull. **46,** 413 (2011).

[65] Z. Fan, , Z. Fan, Q. Zhao, T. Li, J. Yan, Y. Ren, J. Feng, T. Wei, Carbon **50,** 1699 (2012).

[66] C. G. Liu, M. Liu, F. Li, and H. M. Cheng, Appl. Phys. Lett. **92,** 143108(1-3) (2008).

[67] Q. Cheng, J. Tang, J. Ma, H. Zhang, N. Shinya, and L.-C. Qin, Carbon **49,** 2917 (2011).

[68] S. T. Senthilkumar, R. Kalaiselvan , N. Ponpandian, and J. S. Melo, RSC Adv. **2,** 8937 (2012).

[69] J. Yan, J. Liu, Z. Fan, T. Wei, and L, Zhang, Carbon **50,** 2179 (2012).

[70] A. Yu, I. Roes, A. Davies, and Z. Chen, Appl. Phys. Lett. **96** (2010) 253105(1-3).

[71] W. Shi , J. Zhu , D. H. Sim, Y. Y. Tay , Z. Lu, X. Zhang , Y. Sharma , M. Srinivasan , H. Zhang, H. H. Hng, and Q. Yan, J. Mater. Chem. **21,** 3422 (2011).

Chapter 5

Development of graphene oxide nanopaint for multifunctional applications.

5.1 Introduction

Paints are a class of "fluid materials" used for the decoration or protection of any surfaces where they are coated [1]. They have wide-spread applications in the day-to-day life of human society ranging from household care, biomedical field, to a variety of industrial sectors including construction, aerospace and maritime industries [2]. In broad aspects, paints are used to protect metals in these sectors since corrosion of metals is one of the worldwide concerns cost around 1.8 trillion US dollars (nearly 3 to 4% of the gross domestic product) of industrialized countries. The significant issue in the anti-corrosive coatings is to find a suitable alternative for the chromates (corrosion inhibitor additive) used in the coatings due to its toxic nature [3]. On the other hand, coatings with antibacterial property are also essential for controlling the growth and transfer of bacterial population thereby reducing the health care associated infections (HAI) [4]. Furthermore, paints with anti-corrosive and antibacterial properties can be used as "bottom paints" for the protection of metal hulls in the ship, since marine fouling is one of the global dilemma in the maritime industries [5]. Strikingly, the choice for the non-biocidal approach for the marine coating is needed for the environmental concern due to the adverse effects of biocide containing compounds [6]. The coating experts believe that the synergy of nanotechnology and nanomaterials combined with suitable polymer chemistry will

pave the way for the development of next generation coatings for diverse applications.

Nanocoatings can also be termed as "functional coatings" owing to their superior properties such as enhanced corrosion inhibition, self-cleaning, antifouling properties, etc., than the conventional coatings [7,8]. There are only limited reports available in the literatures regarding the applications of nanomaterials in the painting industry. Several metal oxide nanoparticles such as ZnO, Co_3O_4, TiO_2, have been used in paints as pigments due to their UV absorption property [9]. Silver and silver vanadate nanoparticles are used as antibacterial additives in paints [4,10]. Nanosized aluminum phosphates embedded in polyurethane for improving the corrosion resistance of polyurethane paints [7]. However, the increasing demand in the design and development of functional coatings triggers the researchers to formulate novel paints with nontoxic additives due to their huge impact on the health care, industrial and environmental sectors.

Recently, GO nanosheets become one of the hot materials owing to their unique properties such as gram scale production at very low cost, biocompatibility, fluorescence, tunable properties by controlling oxidation level, which makes them a potential candidate for wide disciplines ranging from electronics, optics, energy storage devices, to bio-sensors, as well as antibacterial applications [11-14]. Being a non-stoichiometric macromolecule, GO is extensively investigated by researchers from various disciplines and found that it possesses several distinct properties such as a template for nanocrystal growth, carbocatalysis (for oxidation reactions), functionalization with organic/inorganic materials via guest-host chemistry, cross-linking agent for polymerization, etc., for the design of novel materials with exceptional properties [16-17]. More recently, GO coating is used for the corrosion

inhibition of aluminum current collector in Li-ion batteries is reported [18]. The distinct properties of GO such as anticorrosion, antibacterial, fluorescence nature, biocompatibility and other properties (as stated above) motivated us to explore the potential utility of this material as a pigment in paints for the development of functional coatings.

Further, the additives used in the formulation of paint are very important in order to achieve high-quality surface finishing. In general, paints have different components viz, pigment, binder, drier, wetting agent stabilizer, thickener, etc., in which each component plays a crucial role in the properties of paint [19]. In our study, we used suitable harmless additives in the GO paint formulation to ensure their environmental friendly. For instance, we used alkyd resin (known for its biocompatibility) as the binder material in the paint component. Strikingly, the technology employed for the production of any product has a potential impact on the commercialization strategy. Hence, we employed a high-energy ball milling (HEBM) technique, a well-known technique used in many industries for the preparation of powder, composites, etc. We believe that our efforts in the design and development of GO paint with nontoxic additives *via* facile HEBM method will open the door for the real-world applications of this product in the coating industry.

5.2 Results and discussion

In this study, a facile method using HEBM technique for the preparation of paints based on GO nanosheets as a pigment embedded in the alkyd resin matrix with appropriate additives (as given in Table 5.1) has been developed. A simple brush coating method is used for the coating of the paint on various surfaces, and the drying process is monitored.

Table: 5.1 Additives and their role in GO paint.

Additives	Materials	Role of additives	Weight Percentage %
Pigment	GO nanosheets	Providing the color of the paint	16.0
Binder	Linseed alkyd resin	Film forming component of paint	64.0
Stabilizer	Nanosized ZnO	Reducing the color fading effect of the paint	0.6
Anti settling agent	Aluminum stearate	For preventing the settling of pigment and binder	0.5
Thickener	Thickener A	For improving the viscosity and prevents coagulation	0.1
Wetting agent	Soya lecithin	For wetting the pigment in the binder for uniform dispersion	0.6
Inner coat drier	Nanosized zirconia	Chemical cross-linking agent of unsaturated fatty acids	0.6
Upper coat drier	Cobalt napthenate	Active catalyst for the lipid autoxidation process	0.6
Thinner	Mineral turpentine oil	Dispersing agent of paint	17.0

5.2.1 Mechanism of drying and role of additives in GO nanopaint

The mechanism of drying in the GO paint relies on the lipid autoxidation process of alkyd resins, which is a well-known phenomenon by the free-radical mechanism in the presence of atmospheric oxygen [20,21]. The poly unsaturated fatty acids in the alkyd resin will undergo a chemical cross-linking via free radical mediated chain reaction thereby resulting in a dried uniform film or coating on the respective surface [22]. The presence of GO pigments in the paints might facilitate the lipid auto-oxidation reaction due to the carbocatalytic property of GO for oxidation and polymerization reactions [23-25]. Previous reports demonstrated that GO nanosheets can be used for the enrichment of the long chain fatty acids due to its chemical structure comprising hexagonal carbon atoms [26]. GO can be easily cross-linked with macromolecules during oxidative polymerization and it acts as a template for the growth of macromolecules [27,28]. During the ball milling process, GO nanosheets cross-linked with the lipid molecules present in the alkyd resin through electrostatic interaction and hydrogen bonding [28] which further results in the formation of black color paint with high order of homogeneity. Similarly, GO nanosheets catalyze the lipid autoxidation process by providing sufficient amount of oxygen during the drying process. It is worth mentioning that a partial reduction of GO can be occurred due to the free radicals generated during the autoxidation process as similar to the previous reports illustrating the reduction of GO through bacterial respiration, free radical reduction, and also during chemical functionalization [29,30]. Although, it is still remaining elusive to understand the cross-linking reaction

occurred between GO and the lipid chain present in alkyd resin, this method opens the way for the preparation of GO paint.

Achieving homogenous mixture of pigment in the binder is very important for a better surface finish. For a better dispersion, the surface energy of the binder should be minimized for the good wetting of the pigment which can be achieved by the addition of a wetting agent. We used soya lecithin as a wetting agent [31] in the GO paint for a better dispersion of GO in alkyd resin. Consequently, the absence of soya lecithin results in non-uniform surface finish due to aggregation of GO nanosheets.

We used two drier in our formulation viz., cobalt napthenate (exterior drier) and nanosized zirconia (interior drier). Cobalt napthenate is an active catalyst for the lipid autoxidation process [32], thereby it results in the faster drying time and uniform coating on the surfaces. Nanosized zirconia is a chemical cross-linking agent [33] of unsaturated fatty acids and it enhances the rate of cross-linking during drying process. The role of these driers significantly improves the drying time of GO paint as evidenced by Table 5.2. The active role of stabilizer (nanosized ZnO) in the paint formulation is to inhibit or prevent the separation of GO nanosheets in the alkyd resin for a long period of time and it also reduced the color fading effect of the final product [34]. A combination of commercially available thickener A and anti-settling agent (aluminum stearate synthesized in our laboratory) is used for improving the viscosity and for preventing the coagulation.

5.2.2 Properties of GO nanopaint.

The salient features of paint such as solid content, drying time, hiding power, spreading area and gloss measurements were performed for the GO paint in

comparison with the commercially available black color paint, and the results are provided in Table 2.

Table: 5.2 Comparison of GO paint with commercial paint

Test	Commercial paint	GO paint
Gloss @ 60 degree	75	75
Solid Content %	39.21	64.24
Acid Resistance	Peel off from substrate	Stable after exposure
Drying time (in hours) at room temperature		
Surface dry	4	1
Dry hard	8	3
Dry to overcoat	24	6

The solid content of the paint is the ratio of total weight of the solid ingredient in the paint to the total weight of the total ingredients in the paint. The solid content of the GO paint is about 64.24 % whereas for commercial paint is only 39.21 %. It signifies that the GO paint with higher solid content will be more economic than the commercial one. The drying time such as surface dry, dry hard and dry to recoat are monitored for the GO paint coatings at regular intervals [19]. The drying time for the GO paint is faster than the commercial black paint as evident from Table 5.2.

For the measurement of hiding power, spreading area and gloss measurement, the GO paint is coated on to the commercially available drawdown card [19] using a multifunctional thin film applicator. The thickness is controlled in the range of 150

μm using the thin-film applicator. The hiding power can be seen from Figure 5.1 (b) based on the drawdown card image painted using GO paint. It is clear from the Figure

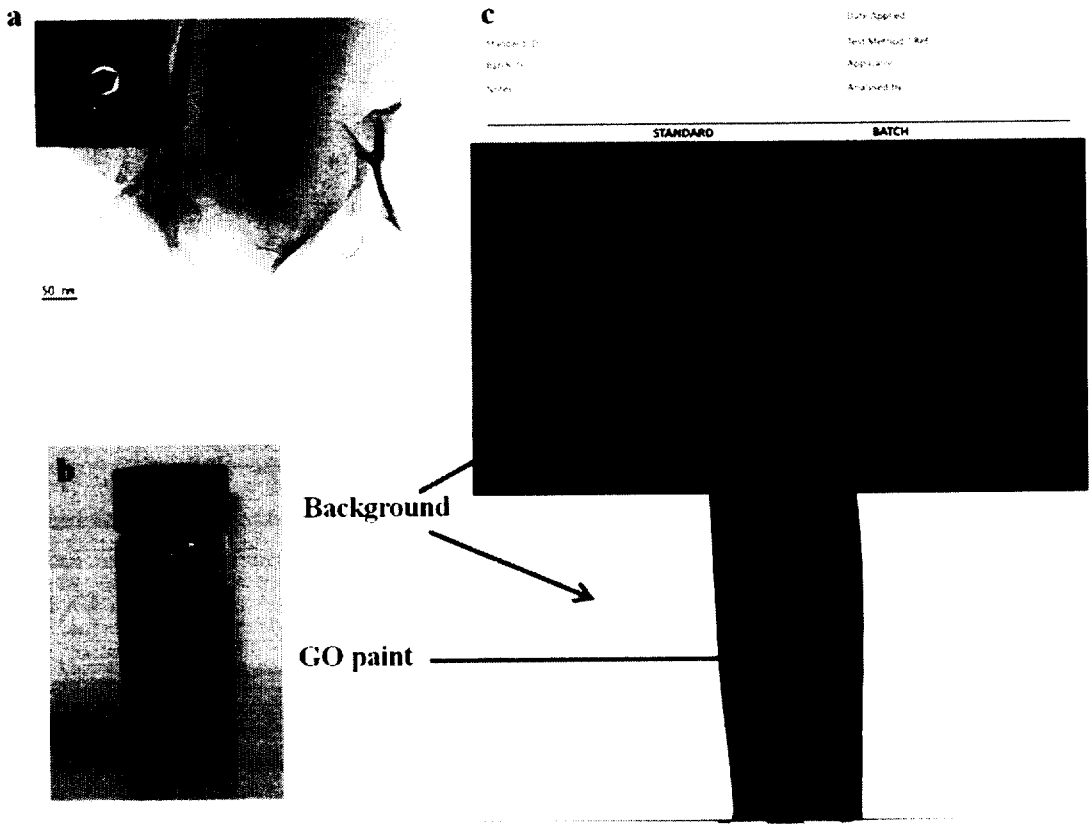

Figure 5.1 GO nanopaint (a) High resolution transmission electron microscope image of GO nanosheet and inset shows the corresponding SAED pattern. **(b)** Digital image of as prepared GO paint using ball milling method, (**c**) GO paint coated on drawdown card for the measurement of gloss, and hiding power. The multi thin film applicator used for the GO paint coating and the thickness was about 150 μm.

5.1 (b) that GO paint completely hides both the background colors black (top) and white (down) in the drawdown card. The spreading area is calculated as 72 cm^2 whereas for the commercial paint it is only 59 cm^2. The gloss measurement of GO paint shows that gloss@60° is about 75 GU. According to the ASTM standard, coating having gloss@60° with values higher than 60 GU is classified as a high gloss

surface [35]. This confirms the good surface finishing property of GO paint coatings. The GO paint holds better properties than the commercial black color paint which is mainly due to the unique properties of GO and the interaction between the GO and alkyd resin.

5.2.3 Spectroscopic investigation and surface analysis of GO paint.

For better understanding of the binding interactions occurred between the alkyd resin and GO nanosheets in the paint formulation, we employed Fourier transform infra red (FT-IR) spectra, laser Raman spectra, and X-ray photoelectron spectra (XPS). Figure 5.2 represents the FT-IR spectra of bare alkyd resin and the final GO paint. The FT-IR spectra of bare alkyd resin shows the presence of C-O group (1070 cm^{-1}), C-H in-plane vibrations (1121 cm^{-1}), C-O-C groups (1261 cm^{-1}), pyrrole ring (1459 cm^{-1}, 1579 cm^{-1}), C-C stretching (1600 cm^{-1}), carboxylic group (1730 cm^{-1}) and C-H vibration in methyl and methylene group (2800-3000 cm^{-1}) [36]. All these functional groups are preserved in the FT-IR spectrum of GO paint and the oxygenated functional groups present in GO nanosheets such as epoxyl, hydroxyl, carbonyl, and carboxyl groups are overlaid with the spectra of alkyd resin. However, the intensity of C-H group in the alkyd resin (2800-3000 cm^{-1}) significantly decreased in the GO paint and C-C vibrations move towards a higher wavenumber. The change in the carbonyl group is ascribed to the chemical cross-linking process occurred in the GO paint. This illustrates that structural changes have been occurred in GO paint through electrostatic interaction and hydrogen bonding between GO and alkyd resin [37].

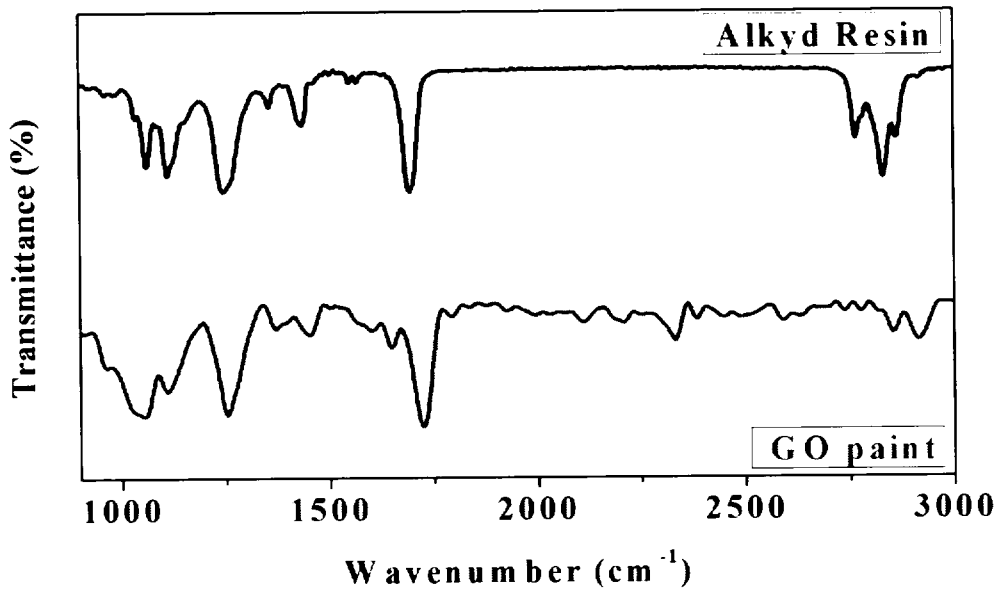

Figure 5.2 Fourier transform infra-red spectra of alkyd resin and GO paint.

In contrast to the FT-IR spectra, the Raman bands of pure alkyd resin observed at 1265 cm^{-1}, 1443 cm^{-1}, 1675 cm^{-1}, 2900 cm^{-1} and 3100 cm^{-1} [38] were diminished in the Raman spectra of GO paint (as shown in Figure 5.3) and only bands corresponding to sp^3 carbons (1610 cm^{-1}) and defects in carbon materials (1350 cm^{-1}) were observed. This is in agreement with the previous report on the Raman spectra of paint comprised of carbon black [39]. The Raman spectra of GO paint and the bare GO nanosheets were almost revealed the similar type of spectra with significant changes in the bands at the over tone regions. The G band position in GO nanosheets (1598 cm^{-1}) moved towards a higher wavenumber which suggested the increase in sp^3 domains in the paint due to the high content of alkyd resin. The disappearance of Raman bands of alkyd resin in paint can be attributed to the fluorescence nature of GO. This finds supports with the previous experimental results of Palus et al [40]. In order to confirm this issue, we also compared the Raman spectra of alkyd resin with the TiO_2 based paint (fabricated by the similar method using TiO_2 nanoparticles as

pigment instead of GO nanosheets – white colored paint) and confirmed that this is attributed due to the fluorescence property of the pigment material.

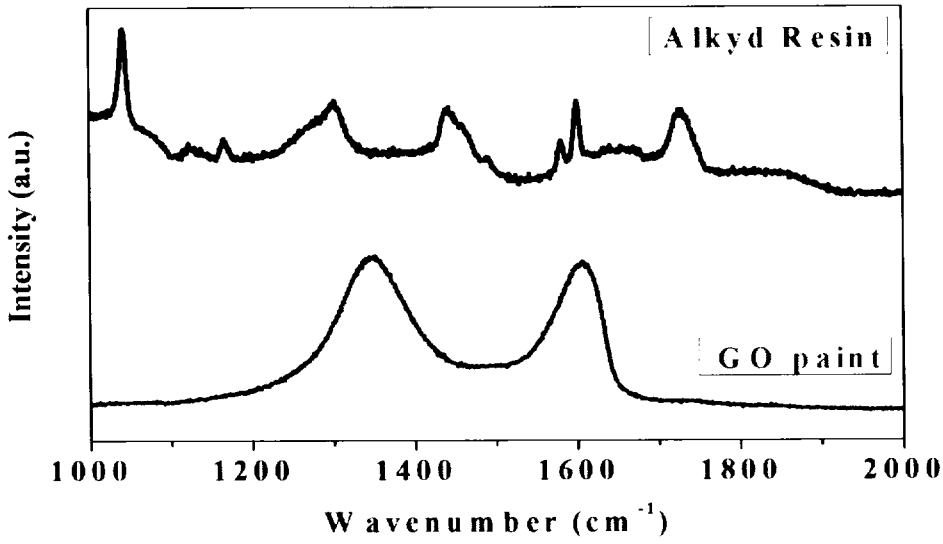

Figure 5.3 Raman spectra of alkyd resin and GO paint.

Further, we employed XPS analysis to investigate the surface composition of the GO paint and the XPS spectrum of bare alkyd resin and GO paint are shown in Figure 5.4. In comparison with the spectra of alkyd resin, the XPS of GO paint shows increase in oxygen content due to the presence of oxygenated functional groups in GO. The calculated C/O ratio from the XPS spectra of the bare alkyd resin and GO paint is 3.75 and 3.29, respectively. The C1s deconvoluted spectrum is shown in Figure 5.5 which shows the presence of C-C, C-OH and C-OO groups at 285.4, 286.37 and 288.88 eV respectively thus confirming the presence of fatty acids and ester groups in the alkyd resin. The peaks corresponding to the other additives such as ZnO, ZrO_2 etc., are not observed in the XPS survey scan, this is due to the lower weight fraction of these constituents in the paint.

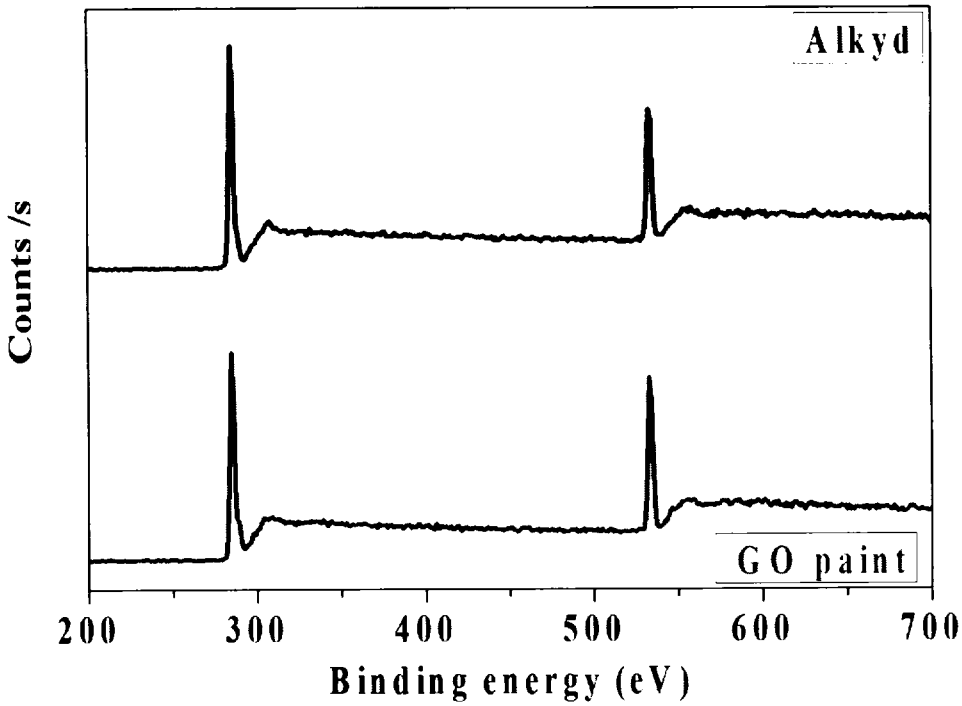

Figure 5.4 XPS survey spectra of alkyd resin and GO paint.

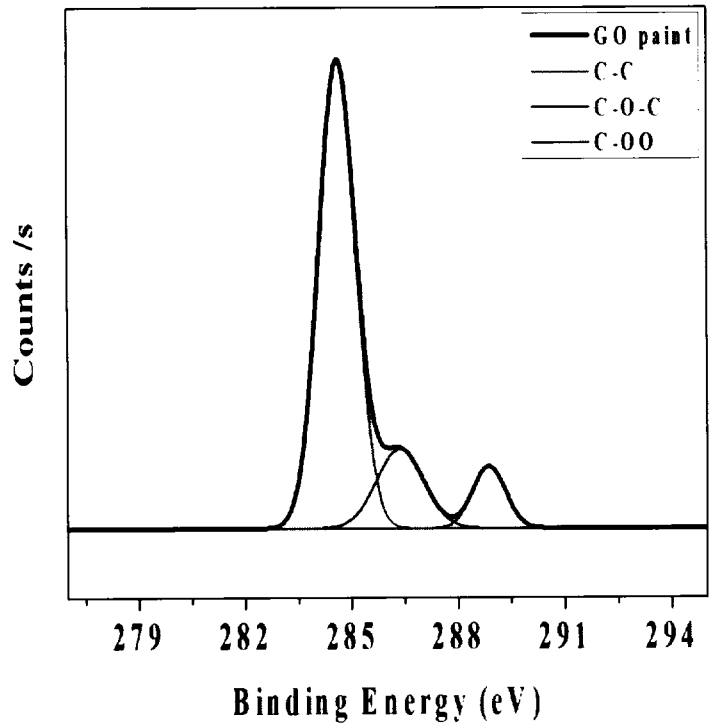

Figure 5.5 XPS C 1s deconcoluted spectra of alkyd resin and GO paint.

The surface morphology of the coated paint was investigated by field emission scanning electron microscope (FE-SEM) studies. Figure 5.6 shows the low and high magnification image of the paint coatings. Both the images revealed the uniform coating of the paint on the substrates and there is no void regions were observed in the FE-SEM image. The presence of GO nanosheets in the paint is not distinguishable which is depicts the role of ball milling process for preparing homogenous mixture of paint.

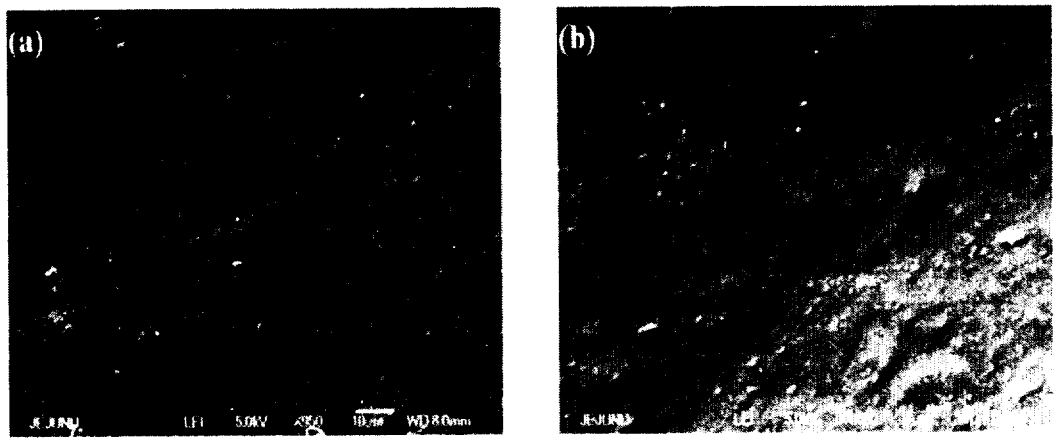

Figure 5.6 FE-SEM analysis of GO paint coating (a) low magnification image (10 μm), and (b) high magnification image (1 μm).

5.2.4 Corrosion in acidic media.

The GO paint coatings are characterized for their application for corrosion resistant coatings using the weight loss method by exposing the GO paint coated galvanized iron (GI) substrate in acidic media (0.1 N HCl) for 24 h and bare GI substrate is used as the control. It is clear from Figure 5.7 that the bare GI substrate after reaction with the acid media resulted in the formation of the rust on the surface due to the oxidation of metal exposed to acidic environment. The GO paint coated

substrate shows high corrosion resistant in acidic media which is ascribed to the corrosion inhibition property of GO. The corrosion inhibition efficiency of GO paint coating is calculated using the formula [41]

$$\text{Inhibition efficiency } \% = [(W_{uncoated}-W_{coated})/W_{uncoated}] \times 100 \quad \ldots\ldots\ldots\ldots\ldots\ldots \quad (1)$$

where $W_{uncoated}$ is the weight loss in bare substrate and W_{coated} is the weight loss in GO paint coated substrate. The GO paint coatings possess an inhibition efficiency of about 88.70 % than the bare substrates which substantiates the corrosion resistant property of GO paint.

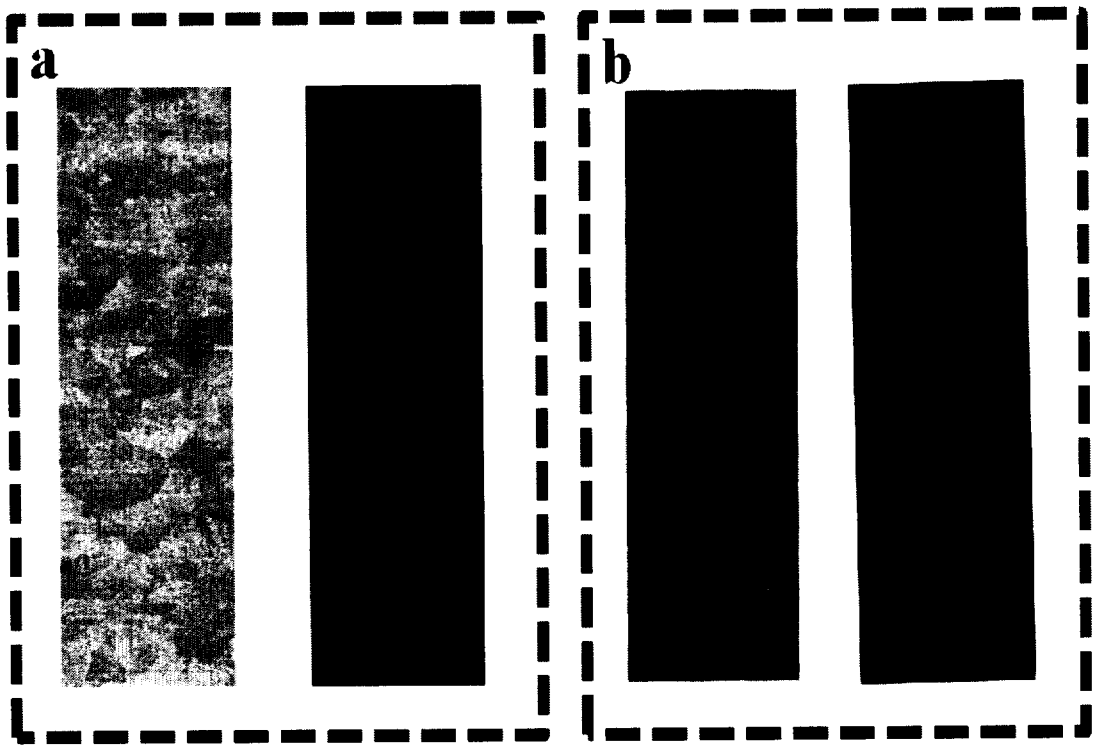

Figure 5.7 The GO paint is coated onto galvanized iron sheets. Digital image of bare and GO paint coated substrates (**a**) before exposure to acid (**b**) after immersion in HCl solution for a period of 24 h.

5.2.5 Electrochemical corrosion test in NaCl solution.

The electrochemical test or Tafel analysis is one of the standard methods used for the study of corrosion in metals [42]. The corrosion behavior of the metals can be explained by two reactions viz. (i) anodic oxidation of metal into metal ions and (ii) the cathodic reduction which utilize the electrons during the oxidization reaction. Both reactions will occur simultaneously and hence limiting one of this reaction will results in the prevention of corrosion. The potentiodynamic polarization curves of bare GI substrates and GO paint coated GI substrates measured in 3.5% NaCl solution are shown in Figure 5.8. The corrosion potential (E_{corr}) and the corrosion current density (I_{corr}) for bare GI substrate and GO paint coated GI substrate were calculated from the polarization curves by fitting the Tafel equation. It is obvious from Figure 5.8 that the anodic current densities of the GO coated substrates were more than one order of magnitude lower than that of the uncoated substrates. This illustrates that the GO paint coating significantly decreases the dissolution of metal ions from the substrates. The measured E_{corr} of the GI substrate and GO paint coated GI substrate were -1047 mV and -995 mV, respectively. The observed shift in E_{corr} of the GO coated substrates about 52 mV towards the positive potential side and the decrease in I_{corr} suggest that the GO paint coatings significantly improved the corrosion resistance of the bare substrate by acting as a protective layer between the substrate and the corrosive environment.

The protective efficiency $P_i(\%)$ of the GO paint coating is obtained from the polarization curves calculated by the equation [43]:

$$P_i(\%) = [1-(I_{corr}/I'_{corr})] \times 100 \quad \text{.....(2)}$$

where I_{corr} and I'_{corr} indicates the corrosion current density of GO coated GI substrate and the bare GI substrate respectively. The protective efficiency of the GO paint shows 76.61 % compared to the bare substrate ensures the potential utility of this paint towards corrosion inhibition coatings.

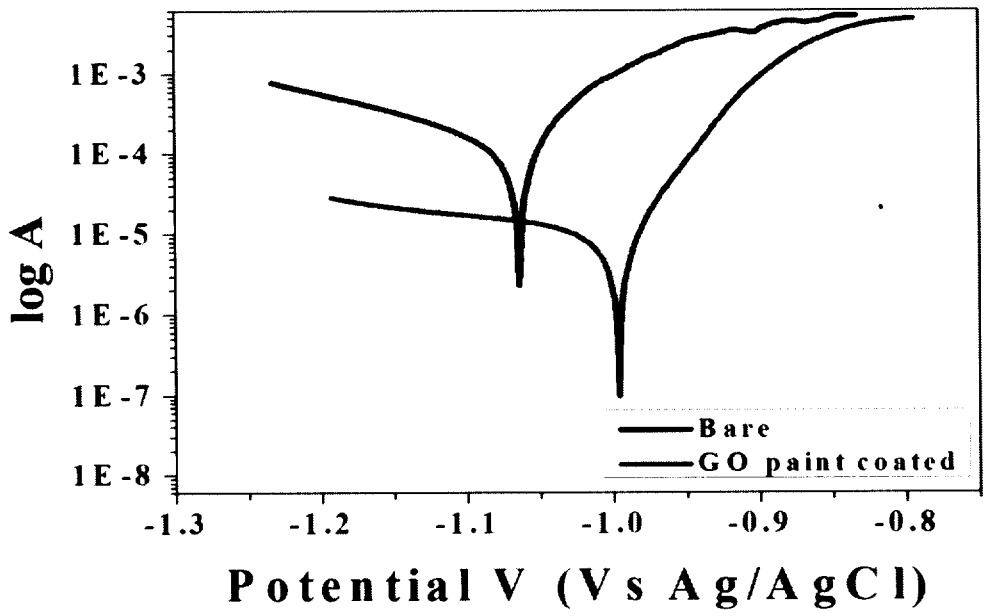

Figure 5.8 Linear polarization curves of bare and GO paint coated substrates in 3.5 % NaCl solution.

The corrosion resistant applications of GO paint suggested that the GO paint shows superior inhibition of metal corrosion both in acidic and salt medium. In these experiments, the Cl^- ions present in the test solution is one of the most powerful source for the oxidation of metal [44] and is evident from Figure 5.7 that formation of rust in uncoated substrates exposed to HCl solution and stability of GO paint in acidic media. The electrochemical corrosion test performed in NaCl solution, a prototype of sea water [4] and it is evident from Figure 5.8 that the GO paint acts as protection layer (with 76.41% protection efficiency) for the substrates when exposed to NaCl solution. The corrosion inhibition property is attributed to the corrosion inhibition

behavior of GO and the molecular level interaction between the GO and the alkyd resin in the paint. Since metal corrosion is one of the universal concern costs around $350 million in the world wide market in 2010 and growing to an estimated $900 million by 2015 [45], our efforts in the development of this GO paint with corrosion resistant properties may provide new insights to the industrial sectors.

5.2.6 Antibacterial properties

Several nanoparticles including metals (silver, gold) metal oxides (ZnO, MgO, TiO_2) and carbon materials (graphene, GO, CNT) exhibited antibacterial properties [46]. These intrinsic antibacterial properties of nanoparticles are remaining even after these materials are incorporated in any polymer matrix or in the form of thin films etc. It is well known that both carbon based materials such as CNT, graphene and GO possess antibacterial activity against bacteria. As a supporting evident, we also examined the antibacterial activity of the GO nanosheets and determined their minimum inhibitory concentration (using microdilution method) against *E. coli, S. aureus* and *P. aeruginosa* as 0.5 μg/mL, 0.5 μg/mL, and 1 μg/mL, respectively. This illustrates the superior antibacterial behavior of GO nanosheets. Further, we examined the GO paint coatings for their potential utility towards the control of microbial growth by evaluating their antibacterial activity against *E. coli, S. aureus* and *P. aeruginosa*. Herein, the uncoated substrates are used as a control. Figure 5.9 shows the photographic image of antibacterial properties of GO paint coated substrates against *E. coli.* It clearly depicts that no bacterial colonies were grown on the GO paint coated substrate in comparison with the bare substrate where we observed the growth of bacterial colonies. The similar type of results was obtained for the other two tested bacterial species such as *S. aureus* and *P. aeruginosa* which showed almost complete inhibition of bacterial growth. This study ensures that the GO paint coatings

holds excellent bactericidal efficiency which may create new insights into the GO based surface coatings for antibacterial applications.

Table 5.3 Minimum inhibitory concentration (MIC) of GO nanosheets against bacteria

Bacterial Strains	MIC
E. coli	0.5 μg mL
S. aureus	0.5 μg mL
P. aeruginosa	1 μg mL

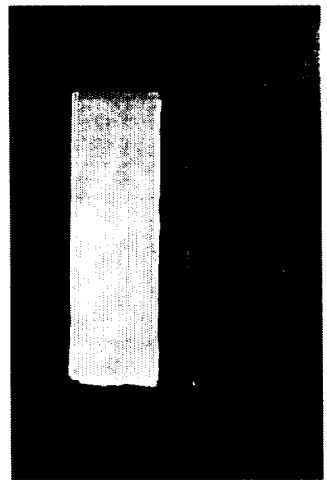

Figure 5.9 Antibacterial activity of GO paint coated substrate against *E .coli*.

Table 5.3 shows the MIC value of GO nanosheets against the tested bacteria. The photographic image represents the antibacterial activity of GO paint coated substrate against *E. coli*. The bare substrate shows the growth of bacteria whereas no bacterial growth was observed on GO paint coated substrate.

The antibacterial test performed evidences the inhibition of bacterial growth on the GO paint coated substrates in comparison with the bare substrates as shown in Figure 5.9. The mechanism of the antibacterial activity of the GO paint might be due to membrane and oxidative stress. This is supported by the previous reports on the inhibition of bacterial growth in GO based thin films and composites [47]. Thus the GO paint can be used for the prevention of health care associated infections.

5.2.7 Marine antifouling experiments

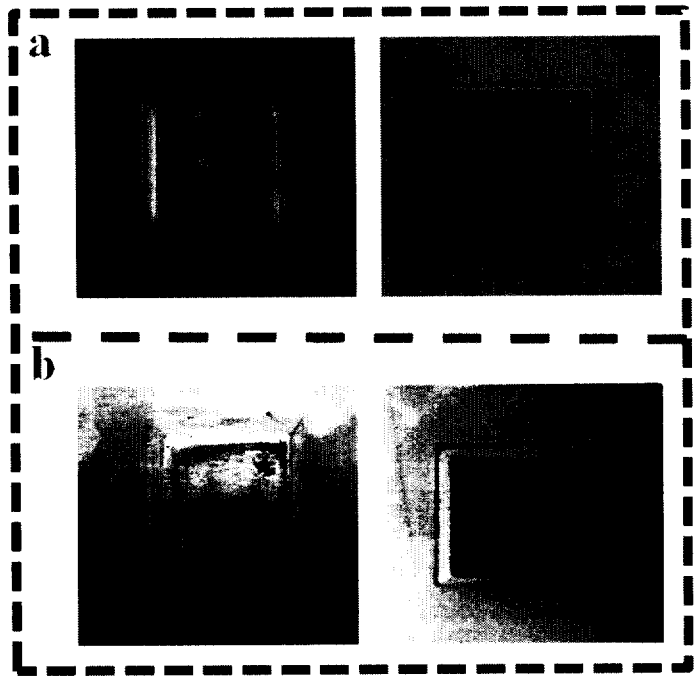

Figure 5.10 Antifouling activity of GO paint coated substrate in marine environment. The bare substrates and GO nano paint coated substrates are fixed in to substrates and kept in seawater (lagoon with tidal water directly connected to the Jeju Sea). (a) before and (b) after 1 week exposure in sea water. The bare substrates shows metal corrosion and fouling of organisms whereas GO nanopaint surfaces shows inhibition of bio-fouling.

The key issue in the marine industry (problem costs around $260 per annum in the US Navy fleet) relies on the bottom paints in which anticorrosive and antibacterial property are mandatory since the immersion in sea water leads to corrosion and formation of biofilm in the hulls of the ship [48,49]. Bacterial colonization is the first step in the biofilm formation which leads to the colonization of fouling organisms at the bottom of the ship [50]. In the present study, GO paint completely inhibit the

growth of the bacteria on its surface thus prevent the biofilm formation. In these aspects, we examined the anti-fouling property of the GO nanopaint for their potential applications towards marine painting. The bare and GO paint coated GI substrates were fixed and immersed into the sea water (lagoon with tidal water directly connected to the Jeju Sea) and the photographic images were recorded before and after 1 week period of immersion and is shown in Figure 5.10. It shows the formation of marine organism in bare substrates and GO paint coated substrates restricts the growth of marine organisms.

Moreover, there is no toxic materials such as chromates is present in the GO paint suggested their environmental benign nature. With the advantage of being anti corrosive in salt water combined with antibacterial and antifouling properties, we believe that the GO paint may find its potential utility towards industrial applications especially in the marine industry as a suitable alternative for "bottom paints".

5.3 Conclusion

In conclusion, we have demonstrated a versatile approach for the preparation of environmentally benign GO paint. The given method is not only limited to GO embedded paint but also can be applicable to the preparation of other nanomaterials based paints as well. The paint formulation, mechanism of drying, role of additives, other paint properties are discussed. The key findings of the work suggested that GO paint clasps superior corrosion resistant and excellent antibacterial properties ensure their promising applications in the coating industry. Given the scalability and processability of ball milling approach and the extraordinary properties of GO paint, we believe that it will create new insights into the development of next generation coatings in the near feature.

REFERENCES:

1. A. Kumar, P. K. Vemula, P. M. Ajayan, and G. John, Nature Mater. 7, 236 (2008).
2. J. Lee, S. Mahendra, and P. J. J. Alvarez, ACS Nano **4,** 3580 (2010).
3. J. Bohannon, Science **309**, 376 (2005).
4. E. Armelin, R. Oliver, F. Liesa, J. I. Iribarren, F. Estrany, and C. Aleman, Prog. Org. Coat. **59**, 46 (2007).
5. K. Kowalczyk, K. Luczka, B. Grzmil, and T. Spychaja, Prog. Org. Coat. **74,** 151 (2012).
6. N. S. Allen, M. Edge, A. Ortega, G. Sandoval, C. M. Liauw, J. Verran, J. Stratton, R. B. McIntyre, Polym. Degrad. Stabil. **85,** 927 (2004).
7. Z. Cao, and Y. Sun, ACS Appl. Mater. Interfaces. **1,** 494 (2009).
8. K. Krishnamoorthy, G. Manivannan, S. J. Kim, K. Jeyasubramanian, and M. Premanathan, J. Nanopart. Res. **14,** 1063 (2012).
9. E. Almeida, T. C. Diamantino, and O. Sousa, Prog. Org. Coat. **59,** 2 (2007).
10. S. Wijewardane, and D. Y. Goswami, Renew. Sust. Energ. Rev. **16,** 1863 (2012).
11. R. D. Holtz, B. A. Lima, A. G. Souza Filho, M Brocchi, and O. L. Alves, Nanomedicine: NBM **8,** 935 (2012).
12. A. Kolmakov, D. A. Dikin, L. J. Cote, J. Huang, M. K. Abyaneh, M. Amati, L. Gregoratti, S. Günther, and M. Kiskinova, Nature Nanotechnol. **6**, 651 (2011).
13. K. P. Loh, Q. Bao, G. Eda, and M. Chhowalla, Nature Chem. **2,** 1015 (2010).
14. M. Veerapandian, M. H. Lee, K. Krishnamoorthy, and K. Yun, Carbon **50,** 4228 (2012).

15. M. S. Mannoor, H. Tao, J. D. Clayton, A. Sengupta, D. L. Kaplan, R. R. Naik, N. Verma, F. G. Omenetto, and Michael C. McAlpine, Graphene-based wireless bacteria detection on tooth enamel. Nature Commun. 3:763 DOI: 10.1038/ncomms1767.

16. H. Wang, Q. Hao, X. Yang, L. Lu, and X. Wang, ACS Appl. Mater. Inter. **2,** 821 (2010).

17. D. A. Dikin, S. Stankovich, E. J. Zimney, R. D. Piner, G. H. B. Dommett, G. Evmenenko, S. T. Nguyen, and R. S. Ruoff, Nature **448,** 457 (2007).

18. K. Krishnamoorthy, M. Veerapandian, K. Yun, S. J. Kim, Carbon (2012), http://dx.doi.org/10.1016/j.carbon.2012.10.013.

19. G. Gsward (Ed.), Paint Testing Manual. (ASTM Philadelphia, 1972).

20. W. J. Muizebelt, J. C. Hubert, M. W. F. Nielen, R. P. Klaasen, and K. H. Zabel, Prog. Org. Coat. **40,** 121 (2000).

21. Bieleman, J. H. *Additives for Coatings* (Wiley-VCH, Weinheim, 2000).

22. Schaich, K. M. Bailey's Industrial Oil and Fat Products, Sixth Edition, Six Volume Set. Edited by Fereidoon Shahidi. Copyright # 2005 John Wiley & Sons, Inc.

23. D. R. Dreyer, H. –P. Jia, and C. W. Bielawski, Angew. Chem. Int. Ed. **49,** 6813 (2010).

24. S. H. Lee, S. H. Lee, D. R. Dreyer, J. An, A. Velamakanni, R. D. Piner, S. Park, Y. Zhu, S. O. Kim, C. W. Bielawski, R. S. Ruoff, Macromol. Rapid Commun. **31,** 281 (2009).

25. D. R. Dreyer, and C. W. Bielawski, Adv. Funct. Mater. **22,** 3247 (2012).

26. Y. Liu, J. Liu, C. Deng, and X. Zhang, Rapid Commun. Mass Spectrom. **25,** 3223 (2011).

27. S. Park, K.-S. Lee, G. Bozoklu, W. Cai, S. T. Nguyen, and R. S. Ruoff, ACS Nano. **4,** 572 (2008).

28. D. Chen, H. Feng, and J. Li, Chem. Rev. (2012) **DOI:** 10.1021/cr300115g.

29. O. Akhavan, and E. Ghaderi, Carbon, **50,** 1853 (2012).

30. K. Vinodgopal, B. Neppolian, I. V. Lightcap, F. Grieser, M. Ashokkumar, and P. V. Kamat, J. Phys. Chem. Lett. **1,** 1987 (2010).

31. P. M. Scocca, J. Am. Oil Chem. Soc. **53,** 428 (1976).

32. Z. O. Oyman, W. Ming, and R. Linde, Prog. Org. Coat. **48,** 80 (2003).

33. K. Yoshida, Y. Tsuo, and M. Atsuta, J Biomed Mater Res B: Appl Biomater. **77B,** 28 (2006).

34. M. Rashvand, Z. Ranjbar, and S. Rastegar, Prog. Org. Coat. **71,** 362 (2011).

35. Duttaa, S., Karaka, N. & Jana, T. Evaluation of *Mesua ferrea* L. seed oil modified polyurethane paints. *Prog. Org. Coat.* 65 (2009) 131–135.

36. G. S. Goncalves, A. F. Baldissera, L. F. Rodrigues Jr, E. M. A. Martini, and C. A. Ferreira, Synthetic Met. **161,** 313 (2011).

37. S. Park, D. A. Dikin, S. T. Nguyen, and R. S. Ruoff, J. Phys. Chem. C, **113,** 15801 (2009).

38. S. J. F. Erich, J. Laven, L. Pel, H. P. Huinink, and K. Kopinga, Prog. Org. Coat. **52,** 210 (2005).

39. J. D. Gelder, P. Vandenabeele, F. Govaert, and L. Moens, J. Raman Spectrosc. **36,** 1059 (2005).

40. J. Z. Palus, A. Michalska, and A. W. -Birczyn ska, J. Mol. Struct. **993,** 134 (2011).

41. J. Tang, Y. Shao, T. Zhang, G. Meng, and F. Wang, Corros. Sci. **53,** 1715 (2011).

42. D. Prasai, J. C. Tuberquia, R. R. Harl, G. K. Jennings, and K. I. Bolotin, ACS Nano **6,** 1102 (2012).

43. C. –H. Chang, T.-C. Huang, C.-W. Peng, T.-C. Yeh, H. I. Lu, W.-I. Hung, C. J. Weng, , T. I. Yang, J.-M. Yeh, Carbon **50,** 5044, (2012).

44. R. K. Singh Raman, P. C. Banerjee, D. E. Lobo, H. Gullapalli, M. Sumandasa, A. Kumar, L. Choudhary, R. Tkacz, P. M. Ajayan, and M. Majumder, Carbon **50,** 4040 (2012).

45. The world market for abrasion, wear and corrosion resistant nanocoatings. http://marketpublishers.com/r/WDD47C8E29FEN.html.

46. M. Premanathan, K. Karthikeyan, K. Jeyasubramanian, and G. Manivannan. Nanomedicine: Nanotechnol. Bio. Med. **7,** 184 (2011).

47. I. N. Kholmanov, M. D. Stoller, J. Edgeworth, W. H. Lee, H. Li, J. Lee, C. Barnhart, J. R. Potts, R. Piner, D. Akinwande, J. E. Barrick, and R. S. Ruoff, ACS Nano **6,** 5157 (2012).

48. E. Almeida, T. C. Diamantino, and O. Sousa, Prog. Org. Coat. **59,** 2 (2007).

49. E. Almeida, E. Marine Poll. Bull. **72,** 159 (2010).

50. F. Fay, D. Carteau, I. Linossier, and K. V. Rehel, Prog. Org. Coat. **72,** 579 (2011).

Chapter 6

Summary

This chapter summarizes the entire results and over all achievements listed in this thesis. Concluding, this dissertation presented the basic understanding of graphene oxide and graphene nanosheets with detailed spectroscopic characterizations. Our experimental results suggested that the properties of GO can be tuned by controlling the oxidation level. The chemical and structural analysis of GO with different degrees of oxidation was studied with the use of XRD, HR-TEM, and various spectroscopic techniques revealed that hydroxyl and carbonyl groups are formed at lower oxidation level and are converted into epoxyl groups with increase in oxidation level. The electrochemical properties revealed a transition from conducting to semiconducting and further into insulating nature with increase in oxidation level.

We have presented different types of reduction method for the reduction of GO into graphene nanosheets. The ultrasound assisted reduction of GO into graphene results in faster reduction reaction than any other method. A new non-toxic reducing agent, galactose is used for the chemical reduction of GO. We also used other reduction technique such as hydrothermal method for the efficient redcution of GO. Moreover, a low cost, non-toxic route to the reduction of GO using hydrogen plasma is demonstrated and the mechanism of redcution is also discussed. All the graphene synthesized by different reduction route for the characterized well.

We also demonstrated multifunctional application of GO and graphene nanosheets. The GO nanosheets can be used for photocatalysis, antibacterial, functional textile and also for corrosion inhibition coating. The graphene nanosheets synthesized by hydrothermal method are evaluated for their antibacterial activity

against pathogenic bacteria. The results shows that graphene nanosheets can be used as a potential antibacterial agent as a suitable alternate to the commercial drug. The graphene nanosheets synthesized by plasma assisted reduction are examined for their applications in supercapacitors. The results showed that it has a better specific capacitance, suggesting their applications in the energy storage devices.

With understanding the basic properties of GO, we used this material for the preparation of multifunctional nanopaint by incorporating GO in alkyd resin with suitable non-toxic additives using a ball milling approach. The prepared GO nanopaint shows promising application towards prevention of bacterial growth, corrosion inhibition of metals and anti-fouling applications. Based on the experimental results, we ensure that GO nanopaint has potential applications in the painting industry as a suitable alternative to the anti-fouling paints in the maritime industries.

APPENDIX

List of Publications in International Journals

1. **Karthikeyan Krishnamoorthy,** Ananthakumar Ramadoss, Gui-Sik Kim, Sang-Jae Kim. Graphene oxide nanosheets–corrosion inhibition coating. Accepted **Science of Advanced Materials.**
2. **Karthikeyan Krishnamoorthy,** Murugan Veerapandian, Kyusik Yun, S-J. Kim, The chemical and structural analysis of graphene oxide with different degrees of oxidation. **Accepted in Carbon. Article in Press.**
3. **Karthikeyan Krishnamoorthy,** Jeong Yong Moon, Ho Bong Hyun, Somi Kim Cho, Sang-Jae Kim. Mechanistic investigation on the toxicity of MgO nanoparticles toward cancer cells. ***Journal of Materials Chemistry.*** **(2012),** Vol-22, pp: 24610-24617.
4. **Karthikeyan Krishnamoorthy,** Gui-Sik Kim, Sang-Jae Kim. Graphene nanosheets: Ultrasound assisted synthesis and characterization. ***Ultrasonics Sonochemistry.*** **(2012),** Vol-20, pp: 644-649.
5. **Karthikeyan Krishnamoorthy,** Murugan Veerapandian, Gui-Sik Kim, Sang-Jae Kim. A one step hydrothermal approach for the improved synthesis of graphene nanosheets. ***Current Nanoscience*** **(2012),** Vol-8, No-6, pp: 834-938.
6. **Karthikeyan Krishnamoorthy,** Murugan Veerapandian, Ling-He Zhang, Kyusik Yun, Sang-Jae Kim. Antibacterial efficiency of graphene nanosheets against pathogenic bacteria via lipid peroxidation. ***Journ. Phys. Chem. C.*** **(2012),** Vol-115, pp: 17280-17287.
7. **Karthikeyan Krishnamoorthy,** Govindasamy Manivannan, Sang Jae Kim, Kadarkaraithangam Jeyasubramanian and Mariappan Premanathan.

Antibacterial activity of MgO nanoparticles based on lipid peroxidation by oxygen vacancy. ***Journal of Nanoparticle Research.*** **(2012),** Vol-14, pp: 1063-6.

8. **Karthikeyan Krishnamoorthy,** N. Umasudhan, Rajneesh Mohan, Jehee Lee, Sang-Jae Kim. Investigation of the antibacterial activity of graphene oxide nanosheets. ***Science of Advanced Materials.*** **(2012),** Vol-4, pp: 1111-1117.
9. **Karthikeyan Krishnamoorthy,** Murugan Veerapandian, Rajneesh Mohan, Sang-Jae Kim. Investigation of Raman and photoluminescence studies of reduced graphene oxide sheets. ***Applied Physics A,*** Vol-106, pp: 501-506.
10. **Karthikeyan Krishnamoorthy,** Rajneesh Mohan, and S-J. Kim, Graphene oxide as a photocatalytic material. ***Applied Physics Letters.*** **(2011)** Vol-98, pp:244101(1-3).
11. **Karthikeyan Krishnamoorthy,** B. Anish, Sang-Jae Kim, R. Murugesan, and Kadarkaraithangam Jeyasubramanian. Enhanced Photodynamic Efficacy and Efficient Delivery of Rose Bengal using Nanostructured Poly (Amidoamine) Dendrimers: Potential application in Photodynamic Therapy of Cancer. ***Cancer Nanotechnology.*** **(2011)** Vol-2, pp:95-103.
12. **Karthikeyan Krishnamoorthy,** N. Umasudhan, Rajneesh Mohan, Jehee Lee, Sang-Jae Kim. Graphene oxide nanostructures modified multifunctional cotton fabrics. ***Applied Nanoscience*** **(2011)** Vol-2, pp:119-126.
13. Rajneesh Mohan, **Karthikeyan Krishnamoorthy,** and Sang-Jae Kim. ZnO piezoelectric fine wire gated Graphene oxide Field effect transistor. **Accepted in *Journal of Nanoscience and Nanotechnology.***
14. Gunasekaran Venugopal, **Karthikeyan Krishnamoorthy,** Rajneesh Mohan and Sang-Jae Kim. An investigation of the electron transport mechanism in

graphene-oxide thin films. ***Material Chemistry and Physics*** **(2012)** Vol-132, pp:29-33.

15. Gunasekaran Venugopal, **Karthikeyan Krishnamoorthy,** Sang-Jae Kim. High performance graphene flakes. **Accepted in Journal of Nanoscience and Nanotechnology.**
16. Rajneesh Mohan, **Karthikeyan Krishnamoorthy,** Sang-Jae Kim. Diameter dependent photocatalytic activity of ZnO nanowires grown by vapor transport technique. ***Chemical Physics Letters,*** **(2012),** Vol-539-540, pp:83-88.
17. Rajneesh Mohan, **Karthikeyan Krishnamoorthy,** Sang-Jae Kim. Photocatalytic activity of Cu-doped ZnO nanowires. ***Solid State Communications,*** **(2012)** Vol-152, pp:375-380.
18. Ananthakumar Ramadoss, **Karthikeyan Krishnamoorthy,** Sang-Jae Kim. An investigation of structural, optical and electrical properties of HfO_2 thin films *via* sol-gel assisted spin coating method. ***Applied Physics Express*** **(2012),** Vol-5, pp: 085803(1-3).
19. Ananthakumar Ramadoss, **Karthikeyan Krishnamoorthy,** Sang-Jae Kim. Investigation of structural and optical properties of HfO_2 nanoparticles *via* precipitation method. ***Materials Research Bulletin***, **(2012)** Vol-47, **pp:** 2680-2684.
20. Ananthakumar Ramadoss, **Karthikeyan Krishnamoorthy,** Sang-Jae Kim. Facile synthesis of HfO_2 nanoparticles *via* precipitation method. ***Materials Letters,*** **(2012)** Vol-75, pp:215-217.
21. **Karthikeyan Krishnamoorthy,** Selvakumar Natarajan, Sang-Jae Kim, Jeyasubramanian Kadarkaraithangam. Enhancement in thermal and tensile

behavior of ZrO_2 / poly(vinylalcohol) nanocomposite film. ***Material Express*** **(2011)** Vol-1, pp:329-335.

Manuscripts under review:

22. **Karthikeyan Krishnamoorthy**, Antony Ananth, Young Sun Mok, Sang Jae Kim. Plasma assisted synthesis of graphene nanosheets and their supercapacitor applications. **Under review.**
23. **Karthikeyan Krishnamoorthy,** Subbiah Geetha, Mariappan Premanathan, Kadarkaraithangam Jeyasubramanian, Sang Jae Kim. Graphene oxide nanopaints. **Under review.**

List of Conferences

1. **Karthikeyan Krishnamoorthy,** V. Gunasekaran, K. Jeyasubramanian, and S.-J Kim. Synthesis of MgO-PVA nanocomposite film and their enhanced mechanical properties. IEEE conference. Jeju, South Korea.
2. **Karthikeyan Krishnamoorthy,** Jeyasubramanian Kadarkaraithangam, Sang Jae Kim. Enhanced Mechanical Properties, Morphological Characterizations and Antibacterial activity of MgO-poly(vinyl alcohol) Nanocomposite Films. Asia Pacific conference, South Korea.
3. **Karthikeyan Krishnamoorthy,** S. J. Kim. Graphene Oxide Field effect transistor. Korean physical society conference, Jeju South Korea.
4. **Karthikeyan Krishnamoorthy,** V. Gunasekaran, Sang-Jae Kim. Electrical characteristics of graphene oxide. KSPE conference.
5. **Karthikeyan Krishnamoorthy,** Navaneethaiyer Umasuthan, Rajneesh Mohan, Jehee Lee, S.-J. Kim. Nano graphene oxide embedded textile fabrics

for their enhanced thermal properties. The 7th International conference on Advanced Materials and Devices. Jeju, South Korea.

6. Rajneesh Mohan, **Karthikeyan Krishnamoorthy**, Sang-Jae Kim. Application of ZnO nanowires for the photodegradation of resazurin. 2011 First ACIS/JNU International Conference on Computers, Networks, Systems, and Industrial Engineering.
7. Gunasekaran Venugopal, **Karthikeyan Krishnamoorthy**, S.-J. Kim. Investigation of Transfer Characteristics of High Performance Graphene Flakes. ICAE -2011 conference, Jeju.
8. Rajneesh Mohan, **Karthikeyan Krishnamoorthy**, S.-J. Kim. ZnO piezoelectric fine wire gated Graphene oxide Field effect transistor. International conference on Advanced Electromaterials (ICAE). . Daejeon, South Korea.
9. Gunasekaran Venugopal, **Karthikeyan Krishnamoorthy**, Rajneesh Mohan, S.-J. Kim. Investigation of Transfer Characteristics of High Performance Graphene Flakes. International conference on Advanced Electromaterials (ICAE) Daejeon, South Korea.
10. Rajneesh Mohan, **Karthikeyan Krishnamoorthy**, S.-J. Kim. Controlling morphology of ZnO nanostructures in catalyst free vapor transport process and their influence on photocatalytic properties, Nano Korea 2011, South Korea.
11. Rajneesh Mohan, **Karthikeyan Krishnamoorthy**, S.-J. Kim. Growth and characterization of Cu doped ZnO NanoRods. 15 th International Symposium on the Physics of Semiconductors and Applications. Jeju, South Korea.

12. Rajneesh Mohan, **Karthikeyan Krishnamoorthy,** S.-J. Kim. Application of ZnO nanowires for the photodegradation of Resazurin. 1st ACIS/JNU Int. Conference on Computers, Networks, Systems, and Industrial Engineering.
13. Rajneesh Mohan, **Karthikeyan Krishnamoorthy,** S.-J. Kim. Piezopotential gated GO Field effect transistor. 13th Korean MEMS conference. Jeju, South Korea.
14. Ananthakumar Ramadoss, **Karthikeyan Krishnamoorthy,** and Sang Jae Kim. Resistive Switching Characteristics of HfO_2 Thin Films Grown by Sol-gel Spin Coating Method. Korean Physical Society, 2012 Spring Meeting, April 24-26 2012, Daejeon Convention Centre, Daejeon, Korea.
15. Ananthakumar Ramadoss, **Karthikeyan Krishnamoorthy,** and Sang Jae Kim. Corrosion behavior of TiN/TiO_2 multilayer coatings in phosphate buffered saline solutions for biomedical applications. Nano Korea 2012, The 10^{th} International Nanotech Symposium & Nano-Convergence Expo in Korea, August 16-18 2012, COEX, Korea.